

Master's Thesis

**Effect of the Cooling Rate and the Surface Film
Composition on the Colloidal Stability of Whey Protein
Based Emulsions of Triacylglycerols**

M.Sc. Charlotte Schueler

Assistant Supervisor: Jasmin Reiner

Supervisor: Prof. Björn Bergenståhl

Examiner: Prof. Federico Goméz

Karlsruhe, November 25, 2022

Lund University

LTH Faculty of Engineering

Department of Food Technology, Engineering and Nutrition

Master of Food Technology and Nutrition

KLGM01 Degree Project in Food Technology



Karlsruhe Institute of Technology

Institute of Process Engineering in Life Sciences

Chair: Food Process Engineering



Preface

This project report represents the final assignment to attain the master's degree in Food Technology and Nutrition at the Faculty of Engineering at Lund University. The project work was carried out at the premises of the Institute of Process Engineering in Life Sciences at the Karlsruhe Institute of Technology (KIT). I am deeply grateful to Jasmin Reiner and Prof. Karbstein for this collaboration, their feedback and input and invaluable discussions. I wish to thank the technical team at KIT, especially Lydia Schuetz, for her experienced advice and her solicitude. A special thanks goes to Annette Schucker from the Institute of Applied Materials and Electrochemical Technologies for carrying out the XRD measurements included in this report. I would like to express my sincere appreciation to my supervisor, Björn Bergenståhl and my examiner Federico Gómez. Federico has not only guided and supported me throughout this project but throughout my entire time as an international student at Lund University. This project is based on and inspired by important findings that Björn's research has provided. It is only thanks to him that I have discovered my passion for emulsion based foods and interfacial phenomena.

Declaration

I hereby declare that this master's thesis is written independently naming all the used sources completely and precisely and marking all the passages taken over from other works entirely or with changes.

I agree with publicising the work completely or in extracts as a printed version in the library of the Chair of Food Process Engineering and at the Food Engineering department at Lund University, as well as in the form of an electronically published document on the data server accessible for non-commercial purposes. This contains the possibility to copy the work completely or in extracts.

November 25th 2022

Date


Signature

Table of Contents

List of Figures	VII
List of Tables	X
List of Equations	XII
List of Abbreviations and Symbols	XIII
Popular Science Abstract	XV
Abstract	XVI
1 Introduction and Motivation	1
2 Theoretical Background.....	3
2.1 Triacylglycerol Emulsions with a Semi-Crystalline Disperse Phase.....	3
2.1.1 Definition of Triacylglycerol Emulsions with a Semi-Crystalline Disperse Phase	3
2.1.2 Melt Emulsification of TAG Emulsions with a Semi-Crystalline Disperse Phase	3
2.1.3 Crystallisation Behaviour of Triacylglycerols.....	4
2.1.4 Crystallisation in Oil-in-Water (O/W) Emulsions	7
2.1.5 Colloidal Instability Mechanisms in Semi-Crystalline Triacylglycerol Emulsions.....	9
2.2 Stabilising Oil-Water-Interfaces with Food-Grade Emulsifiers	13
2.2.1 Properties and Categories of Food-Grade Emulsifiers	13
2.2.2 Combination of Food-Grade Emulsifiers	17
2.2.3 Impact of Food-Grade Emulsifiers on Triacylglycerol Crystallisation	18
2.3 Colloidal Structure of Milk.....	20
2.3.1 Dairy Proteins.....	20
2.3.2 Dairy Fat	21
2.3.3 Dairy Sugar	22
3 Objectives and Hypotheses.....	24
3.1 Objectives and Motivation of the Study Design	24
3.2 Hypotheses	25
4 Materials and Methods	27
4.1 Materials and Tools.....	27
4.2 Emulsion Preparation	28
4.2.1 Coarse Emulsion Preparation	28
4.2.2 Fine Emulsion Preparation	29
4.2.3 Storage Conditions.....	29

4.3	Analytical Methods	30
4.3.1	Laser Diffraction Analysis	30
4.3.2	Polarised Light Microscopy	31
4.3.3	Visual Analysis	31
4.3.4	Differential Scanning Calorimetry	31
4.3.5	X-Ray Diffraction	33
4.3.6	Statistical Analysis	35
5	Results and Discussion	36
5.1	Results on the Macrostructure	36
5.2	Results of the Equivalent Particle Size Distribution and Microstructure	38
5.2.1	Results on the Microstructure	38
5.2.2	Results of the Equivalent Particle Size Distribution	43
5.3	Results on the Melting Behaviour and Crystal Polymorphism	46
5.3.1	Results on the Crystal Polymorphism.....	46
5.3.2	Results on the Melting Behaviour	47
5.4	Discussion	53
5.4.1	Evidence for Creaming	53
5.4.2	Evidence for Mass Transport Processes.....	54
5.4.3	Evidence for Polymorphic Transitions.....	60
6	Conclusion and Outlook	62
6.1	Summary.....	62
6.2	Conclusions	63
6.3	Outlook.....	64
7	References	65
8	Appendix.....	XVII

List of Figures

Figure 2-1 Schematic representation of a melt emulsification process, with Q = heat transfer rate, E_v = volumetric energy density. Green droplets on the right depict crystallinity as observed under polarised light (Abramov et al., 2017, p.1).....	4
Figure 2-2 Lattice parameters, i.e. angles and vectors, allowing to describe and distinguish a crystal unit cell and to categorise crystals into seven different crystal systems (adopted and modified from Shirokanev et al., 2019).	5
Figure 2-3 Left to right: schematic representation of an exemplary TAG molecule (adopted from Motoyama et al., 2010, p.1245) and tuning fork and chair conformation of two solid state TAG molecules (modified from Coultate, 2002, p.16).	5
Figure 2-4 Schematic representation of the temperature dependence of crystal nucleation and growth. While the rate of nucleation is higher at higher levels of supercooling, the rate of propagation increases as the temperature increases because of a higher rate of diffusion (adopted and modified from Roos and Drusch, 2016, p.24).	9
Figure 2-5 Schematic representation of the main colloidal instability mechanisms as found in emulsions (from left to right): creaming, aggregation, coalescence, Ostwald ripening (adopted and modified from Ritzoulis, 2013).	10
Figure 2-6 Schematic representation of semi-crystalline emulsion droplets with protruding crystals that undergo partial (middle) and total (right) coalescence(Rousseau, 2000, p.11).....	12
Figure 2-7 Left to right: Schematic representation of the conformation of a generic random-coil protein (1) as opposed to a globular protein (2) upon adsorption to an emulsion interface with increasing protein concentration from top to bottom (Darling and Birkett, 1986, p.11). Schematic representation of the interfacial conformation of caseins (left) and β -lactoglobulin (right) upon adsorption to an oil droplet surface (dimensions not to scale) (Rayner, 2015, p.100).	14
Figure 2-8 (From left to right) Fischer projection of a glycerophospholipid (Wright and Marangoni, 2006, p.20) and structure of the most common hydrophilic head groups found in milk phospholipids (Contarini and Povo, 2013, p.2810).	15
Figure 2-9 Self-assembly structures of soybean phospholipids formed at surplus of water (adopted and modified from Bergenståhl and Alander, 1997, p.591).....	16
Figure 2-10 Adsorption of phospholipid molecules to an oil-water interface at low pH (Coultate, 2002, p.115).16	
Figure 2-11 Multi-layered interfacial film formed by adsorption of phospholipids to an O/W emulsion at high concentration (Hernqvist, 1986, p.159).	17
Figure 2-12 Illustration of the impact of the size of milk fat globules on their physicochemical properties (Truong et al., 2016, p.36).	22
Figure 4-1 Schematic representation of a crystal unit cell with its parallel planes of atoms. The vector coordinates below are the Miller indices defining the orientation of the planes (adopted from Lebouin et al., 2009).....	33

Figure 4-2 Schematic representation of an X-ray diffractometer with a Bragg-Brentano geometry, where the incident and diffracted beam slits move on a circle around the sample. The incident angle ω is half of the diffraction angle 2θ and the diffraction vector s bisects the angle between the incident and diffracted beam (adopted from Speakman, n.d.).	33
Figure 4-3 Schematic representation of a properly oriented crystal that creates a diffraction peak in an XRD measurement. The orientation of the parallel planes in the crystal structure diffracts the incident X-rays in a way to cause constructive interference. The diffraction vector s bisects the incident and the diffracted angle. d_{hkl} denotes the distance or d-spacing between the parallel planes with the Miller indices (hkl) (adopted and modified from Speakman, n.d.).	34
Figure 4-4 Exemplary diffraction pattern of a TAG with β' and β polymorphic crystals. The labels 's' and 'm' indicate a strong and medium peak intensity (adopted from Calligarisa et al., 2018).	34
Figure 5-1 Images of B samples cooled at slow (left), moderate (middle) and fast (right) rate, taken at t_0 and t_8 .	36
Figure 5-2 Images of C and CC samples cooled at slow (left), moderate (middle) and fast (right) rate, taken at t_0 and t_8 .	37
Figure 5-3 Images of E and EE samples cooled at slow (left), moderate (middle) and fast (right) rate, taken at t_0 and t_8 .	37
Figure 5-4 Microscopic images of undiluted B samples cooled at slow (left), moderate (middle) and fast cooling rate (right) taken at t_0 (top), t_4 (middle) and t_8 (bottom). 20x magnification. Arrows point to emulsion particle flocs.	38
Figure 5-5 Microscopic images of undiluted C samples cooled at slow (left), moderate (middle) and fast cooling rate (right) taken at t_0 (top), t_4 (middle) and t_8 (bottom). 20x magnification. Arrows point to emulsion particle flocs.	39
Figure 5-6 Microscopic images of undiluted CC samples cooled at slow (left), moderate (middle) and fast cooling rate (right) taken at t_0 (top), t_4 (middle) and t_8 (bottom). 20x magnification. Arrows point to emulsion particle flocs.	40
Figure 5-7 Microscopic images of undiluted E samples cooled at slow (left), moderate (middle) and fast cooling rate (right) taken at t_0 (top), t_4 (middle) and t_8 (bottom). 20x magnification. Arrows point to emulsion particle flocs.	41
Figure 5-8 Microscopic images of undiluted EE samples cooled at slow (left), moderate (middle) and fast cooling rate (right) taken at t_0 (top), t_4 (middle) and t_8 (bottom). 20x magnification. Arrows point to emulsion particle flocs.	42
Figure 5-9 Partially (left) and totally merged (centre-left) emulsion particles and Maltese crosses (centre-right and right) found in different samples and after different storage periods. 20x magnification.	42
Figure 5-10 10 %, 50 % and 90 % percentile of the cumulative normalised undersize distribution of the B samples based on the particle volume. All values are averaged, the error bars indicate the SEM (N = 2, n = 3).	43

Figure 5-11 10 %, 50 % and 90 % percentile of the cumulative normalised undersize distribution of the C samples (left) and CC samples (right) based on the particle volume. All values are averaged, the error bars indicate the SEM (N = 2, n = 3).	43
Figure 5-12 10 %, 50 % and 90 % percentile of the cumulative normalised undersize distribution of the E samples (left) and EE samples (right) based on the particle volume. All values are averaged, the error bars indicate the SEM (N = 2, n = 3).	44
Figure 5-13 X-ray diffraction pattern of the B samples crystallised at low (left) and high cooling rate (right). Measurements performed at t_0 (top) and t_8 (bottom) (N = 1, n = 1). Arrows point to detectable peaks.	46
Figure 5-14 X-ray diffraction pattern of the C samples crystallised at low (left) and high cooling rate (right). Measurements performed at t_0 (top) and t_8 (bottom) (N = 1, n = 1). Arrows point to detectable peaks.	47
Figure 5-15 X-ray diffraction pattern of the E samples crystallised at low (left) and high cooling rate (right). Measurements performed at t_0 (top) and t_8 (bottom) (N = 1, n = 1). Arrows point to detectable peaks.	47
Figure 5-16 DSC curves of the B samples measured at t_0 (top) and t_8 (bottom). The curves are averaged over both sample replicates (N = 2, n = 1).	48
Figure 5-17 DSC curves of the C samples measured at t_0 (top) and t_8 (bottom). The curves are averaged over both sample replicates (N = 2, n = 1).	48
Figure 5-18 DSC curves of the CC samples measured at t_0 (top) and t_8 (bottom). The curves are averaged over both sample replicates (N = 2, n = 1).	48
Figure 5-19 DSC curves of the E samples measured at t_0 (top) and t_8 (bottom). The curves are averaged over both sample replicates (N = 2, n = 1).	49
Figure 5-20 DSC curves of the EE samples measured at t_0 (top) and t_8 (bottom). The curves are averaged over both sample replicates (N = 2, n = 1).	49
Figure 5-21 Sum of the melting enthalpy of all endothermic events recorded in the DSC curves of the B , C and CC samples (see Fig. 4-16 to 4-18) cooled at low (left), moderate (middle) and high (right) cooling rate respectively. Values are given as mean \pm SEM (N = 2, n = 1).	52
Figure 5-22 Sum of the melting enthalpy of all endothermic events recorded in the DSC curves of the B , E and EE samples (see Fig. 4-16, 4-19 and 4-20) cooled at low (left), moderate (middle) and high (right) cooling rate respectively. Values are given as mean \pm SEM (N = 2, n = 1).	52

List of Tables

Table 2-1 Melting point of the three main polymorphic forms of different monoacid triacylglycerols (Coulgate, 2002, p.108).	6
Table 2-2 Molecular structure and concentration of the principal fatty acids in milk fat (modified from Bylund, 1995, p.19).	21
Table 4-1 Ingredients for emulsion preparation.	27
Table 4-2 Chemicals needed for DSC measurements and pH adjustment.....	27
Table 4-3 Analytical devices and homogenisers.	27
Table 4-4 Software.	27
Table 4-5 Composition of commercially available lecithins according to manufacturer's specification (Lipoid GmbH, Ludwigshafen, Germany). n. sp. = not specified.	28
Table 4-6 Composition and process parameters of prepared emulsions.	29
Table 4-7 Characteristic diffraction peak positions of the three main polymorphic forms found in milk fat as measured by small and wide angle X-ray diffraction (adopted from Mazzanti et al., 2004, p.1304).	35
Table 5-1 90 % percentile of the cumulative normalised undersize distribution of the colloidal particles in all samples crystallised at low cooling rate (RT). B samples serve as reference. Values are given as mean \pm SEM, values marked with matching letters are significantly different according to one-way ANOVA with $p = 0.05$ ($N = 2$, $n = 3$).	44
Table 5-2 90 % percentile of the cumulative normalised undersize distribution of the colloidal particles in all samples crystallised at moderate cooling rate (RF). B samples serve as reference. Values are given as mean \pm SEM, values marked with matching letters are significantly different according to one-way ANOVA with $p = 0.05$ ($N = 2$, $n = 3$).	44
Table 5-3 90 % percentile of the cumulative normalised undersize distribution of the colloidal particles in all samples crystallised at high cooling rate (IB). B samples serve as reference. Values are given as mean \pm SEM, values marked with matching letters are significantly different according to one-way ANOVA with $p = 0.05$ ($N = 2$, $n = 3$).	45
Table 5-4 90 % percentile of the cumulative normalised undersize distribution of all B samples. Values are given as mean \pm SEM, values marked with matching letters are significantly different according to one-way ANOVA with $p = 0.05$ ($N = 2$, $n = 3$).	45
Table 5-5 90 % percentile of the cumulative normalised undersize distribution of all C and CC samples. Values are given as mean \pm SEM, values marked with matching letters are significantly different according to one-way ANOVA with $p = 0.05$ ($N = 2$, $n = 3$).	45
Table 5-6 90 % percentile of the cumulative normalised undersize distribution of all C and CC samples. Values are given as mean \pm SEM, values marked with matching letters are significantly different according to one-way ANOVA with $p = 0.05$ ($N = 2$, $n = 3$).	45

Table 5-7 Peak melting and crystallisation temperature of the endo- and exothermic peaks in the DSC curves of the B samples. Values are given as mean \pm SEM (N = 2, n = 1). T_m = melting temperature, T_c = crystallisation temperature, T_m add. = melting temperature of the additional endotherm, *no endotherm in the second sample replicate.	50
Table 5-8 Peak melting and crystallisation temperature of the endo- and exothermic peaks in the DSC curves of the C samples. Values are given as mean \pm SEM (N = 2, n = 1). T_m = melting temperature, T_c = crystallisation temperature, T_m add. = melting temperature of the additional endotherm, no endotherm in the second sample replicate.	50
Table 5-9 Peak melting and crystallisation temperature of the endo- and exothermic peaks in the DSC curves of the CC samples. Values are given as mean \pm SEM (N = 2, n = 1). T_m = melting temperature, T_c = crystallisation temperature, T_m add. = melting temperature of the additional endotherm, no endotherm in the second sample replicate.	50
Table 5-10 Peak melting and crystallisation temperature of the endo- and exothermic peaks in the DSC curves of the E samples. Values are given as mean \pm SEM (N = 2, n = 1). T_m = melting temperature, T_c = crystallisation temperature, T_m add. = melting temperature of the additional endotherm.	51
Table 5-11 Peak melting and crystallisation temperature of the endo- and exothermic peaks in the DSC curves of the EE samples. Values are given as mean \pm SEM (N = 2, n = 1). T_m = melting temperature, T_c = crystallisation temperature, T_m add. = melting temperature of the additional endotherm, *no exo-/endotherm in the sample replicate.	51

List of Equations

Equation 4-1..... 30
Equation 4-2..... 31
Equation 4-3..... 31
Equation 4-4..... 34

List of Abbreviations and Symbols

β -lg	Beta lactoglobulin
CMC	Critical micelle concentration
DSC	Differential scanning calorimetry
(DS)PC	(Distearoyl-) Phosphatidylcholine
(DS)PE	(Distearoyl-) Phosphatidylethanolamine
FA	Fatty acid
HLB	Hydrophobic-lipophilic balance
HMF	High melting (fat) fraction
IB	Ice bath
IP	Isoelectric point
LMF	Low melting (fat) fraction
LMWE	Low-molecular weight emulsifier
LVR	Linear viscoelastic range
M	Molarity/molar concentration
MCT	Medium-chain triacylglycerol
MFG	Milk fat globule
MMF	Middle melting (fat) fraction
O/W emulsion	Oil-in-water emulsion
PL	Phospholipid
PC	Phosphatidylcholine
PE	Phosphatidylethanolamine
RF	Refrigerator
rpm	Rounds per minute
RT	Room temperature
SEM	Standard error of the mean
SFC	Solid fat content
SLN	Solid lipid nanoparticle
TAG	Triacylglycerol
W/O emulsion	Water-in-oil emulsion
WPI	Whey protein isolate
wt%	Weight fraction
XRD	X-ray diffraction

Symbol	Unit	Dimension
CI	%	Creaming index
c_p	$\text{kJ kg}^{-1} \text{K}^{-1}$	Specific heat capacity
$d_{3,2}$	μm	Sauter diameter
E_v	J m^{-3}	Volumetric energy density
H_C	mm	Height of the cream layer
H_T	mm	Height of the total emulsion
ΔH_m	J	Melting enthalpy
$\Delta H'_m$	J g^{-1}	(Total) Melting enthalpy per unit mass of fat
λ	m	Wavelength
ω	Rad s^{-1}	Angular frequency
\dot{Q}	W	Heat transfer rate
Q0	%	Cumulative normalised undersize equivalent particle size distribution based on the particle count
Q3	%	Cumulative normalised undersize equivalent particle size distribution based on the particle volume
r^*	m	Critical nucleus radius
T^*	$^{\circ}\text{C}$	Critical temperature
T_m	$^{\circ}\text{C}$	Melting temperature
$x_{10,3}$	μm	Equivalent particle diameter making up the lower 10 % of a volume based undersize distribution
$x_{50,3}$	μm	Equivalent particle median diameter of a volume based undersize distribution
$x_{90,3}$	μm	Equivalent particle diameter making up the lower 90 % of a volume based undersize distribution

Popular Science Abstract

What crystals have to do with the quality of stored food products

Some food components can form crystals when the foodstuff is stored over an extended period of time. These crystals can impair the product's texture and appearance. It is therefore important to control crystallisation in foods to preserve their quality.

When you think of a crystal, you might have a shiny objects in mind, maybe made from water, like snowflakes or ice cubes or made from carbon, like a diamond on an engagement ring. In chemical terms, the crystalline state is one of two solid states that a compound can exist in. Food components such as fats, proteins and sugars can form crystals. In some applications, as for instance ice cream and margarine, crystals are necessary to provide a certain texture.

However, crystals can also form unintentionally in foods such as UHT milk and heavy cream. In these products, the milk fat is initially present as liquid droplets floating around in an aqueous medium. When these products are stored or shipped, the liquid fat droplets can crystallise over time. The fat crystals can grow really big and form sharp edges. The large fat crystals tend to get entangled when they collide. Then they stick together and merge. Eventually, the fat crystals may form one big layer, which floats up. This might make you think that the product has turned bad and make you discard it.

This project was aimed at finding mechanisms to control the fat crystallisation during storage of high fat liquid dairy products. Milk fat is a highly complex natural fat with a varying composition depending on seasonal factors and cow genetics. Therefore, hydrogenated palm oil was used as a model fat. It has a known composition and similar key features to milk fat. After screening the literature, two approaches to control the fat crystallisation were chosen: (a) rapidly cooling the product from the temperatures at which it is processed, i.e. temperatures above the melting point of the fat, to the temperature at which the product is stored and (b) adding certain fats, called phospholipids, because these allow to induce a controlled crystallisation process. Both approaches were expected to lead to the formation of small, equally sized, roundish fat crystals, which would not easily get entangled.

Approach (a) showed no significant effect on any product parameter. Approach (b) on the other hand led to a more uniform crystal size. The benefit of this effect is however outweighed by the costs, that the addition of phospholipids incurs. This is especially true since the quality and the stability of the products were acceptable even without following either approach (a) or (b).

The results of this project suggest that a product formulation without added phospholipids and a cooling process that is not intentionally accelerated are most efficient to reach a stable high fat liquid dairy product.

Abstract

The goal of this project was to investigate the effect and interplay of formulation and processing parameters on the colloidal stability of emulsified triacylglycerols from a product quality perspective. Different methods to quantify and monitor this effect over time were evaluated. The results of this study were intended to lead to the development of industry relevant recommendations to optimise the processing conditions and formulation of a range of different products.

Many commercially important products, including cosmetics, pharmaceuticals and foods such as UHT milk and heavy cream are based on triacylglycerols emulsified in a protein-rich continuous phase. Temperature fluctuations during long-term storage and distribution of these products can cause uncontrolled crystallisation of the disperse fat phase. This impairs the functional and sensory characteristics and the stability of the emulsion system. Product defects and product waste could be reduced by gaining a systematic understanding of the factors that govern the crystallisation behaviour of emulsified triacylglycerols and by finding mechanisms to induce a guided crystallisation process.

In this study, a liquid emulsion system was produced from hydrogenated palm oil, consisting nearly entirely of triacylglycerols, and an aqueous continuous phase, containing β -lactoglobulin as emulsifier. Diffraction analysis, microscopic and calorimetric measurements were used to determine the colloidal stability of the model system over eight weeks of isothermal storage at 22 °C. Based on previous research, it was expected that the surface film composition of the dispersed palm oil droplets and the rate at which the emulsions are cooled from processing to storage temperature, would impact the stability of the system. Thus, the influence of a high, moderate and low cooling rate and the addition of two phospholipids, acting as complementary emulsifiers to β -lactoglobulin, were tested.

No significant effect of the cooling rate on the stability of the emulsion system was noted over a storage period of eight weeks. The addition of phospholipids seemed to have altered the composition and thereby the properties of the emulsion interfaces. The emulsions showed a more uniform fat crystal size but also more extensive flocculation. It is therefore questionable whether the benefit of using phospholipids does not outweigh the costs. One of the two phospholipids even appeared to inhibit the crystallisation of the hydrogenated palm oil, which is unfavourable, when aiming for a fully crystalline fat phase.

The results of this project suggest that a formulation without phospholipids and a slow cooling process are most cost and resource efficient to produce a stable emulsion system. Independent of the formulation or processing, there were signs for the migration of fat molecules between the emulsion particles. This can adversely affect the particles' physicochemical properties and raises the need for further research into mechanisms to prevent mass transport processes in triacylglycerol emulsions.

1 Introduction and Motivation

Many commercially important products are based on (semi-)crystalline natural fats that are emulsified in a protein-rich aqueous continuous phase. Application areas include cosmetics, pharmaceuticals and food products (Truong et al., 2016).

Natural fats consist of a wide variety of different triacylglycerols. This accounts for their complex melting and crystallisation behaviour. (Truong et al., 2014) Temperature fluctuations during long-term storage and distribution of products based on emulsified natural fats can cause uncontrolled (re-)crystallisation of the disperse fat phase and thereby impair the stability of the emulsion system.

In the case of emulsion based foods, the destabilisation of the colloidal structure can have a negative impact on the sensory characteristics of the product. A product with sensory defects risks being rejected by the consumer even if it is still fit for consumption ('food waste'). Emulsion destabilisation can also reduce the product's shelf life and thereby lead to food loss. As there are many dairy products that are based on emulsified (semi-)crystalline natural fats, the dairy industry serves as a good example to illustrate the potential of reducing food waste and loss by prolonging a product's shelf life. According to the Food & Agriculture Organization of the United Nations (2011) around 20 % of the milk globally produced is wasted. In industrialised regions, 40-65 % of this waste occurs at the consumption level, while in Africa, Latin America and South(-east) Asia, most waste production is connected to the distribution of milk. Germany is the largest producer of milk in Europe with roughly 33 million tons produced annually of which half is exported (Federal Ministry of Food and Agriculture, 2020). Export products are subjected to high storage temperatures over extended periods of time and have to face extreme temperature fluctuations during transport and distribution (Tanner and Amos, 2003). These conditions pose an extra challenge to preserve the colloidal structure of the products.

Consumers nowadays call for products with a clean label, i.e. a short list of ingredients all of which are ideally sourced naturally (Saraiva et al., 2020). In order to meet consumer demands, preventing emulsion instability in emulsion based food products should be sought to be achieved by using the minimum amount of stabilising agents and by replacing highly processed or artificial compounds by food inherent functional ingredients. Turning to alternative approaches such as altering the processing conditions might even allow to avoid using additives entirely.

A clean product label is also desired in the cosmetics and pharmaceutical industry, although not primarily motivated by consumer preferences but rather by safety requirements. It is common to use stabilising agents to prolong the shelf-life of pharmaceutical products. Some of these compounds can exert adverse health effects and local toxicity. It is therefore vital to keep the concentration of functional excipients as low as possible and to explore alternatives to potentially irritant and/or allergenic compounds. (Mehnert and Mäder, 2001)

The central idea of this project is to test two possible approaches to increase the shelf life of a liquid emulsion system with a complex natural fat phase and a protein-rich aqueous continuous phase. These two approaches include the manipulation of a processing and a formulation parameter. The findings of this report are supposed to benefit businesses, such as pharmaceutical and food companies, that market products with a composition similar to that of the emulsion system studied herein. If the investigated approaches are found to be effective in improving product quality and prolonging storage stability, this would bring about obvious economic benefits by raising the appeal, safety and competitiveness of the products. An optimised formulation and manufacturing process would also allow to save resources and to prevent product waste. These potential applications of the knowledge gained from this project justify and motivate the conduct of this study.

2 Theoretical Background

2.1 Triacylglycerol Emulsions with a Semi-Crystalline Disperse Phase

2.1.1 Definition of Triacylglycerol Emulsions with a Semi-Crystalline Disperse Phase

Colloidal dispersions are physically heterogeneous, polyphasic systems with a continuous and a disperse phase, the latter consisting of particles or droplets with a size of 1 nm up to 10 μm . Colloidal dispersions are thermodynamically unstable systems because of the acting interfacial tension between the disperse and the continuous phase. Thus, the free energy of the disperse state is higher compared to that of the separated phases. Any colloidal dispersion destabilises over time as the collapse of the system minimises the contact area between the two immiscible phases. (McClements, 2012)

Emulsions are colloidal dispersions consisting of two immiscible liquids of which one is dispersed as droplets in the other (Rousseau, 2000). For food applications, the term 'emulsion' usually has "[...] a broader definition [...], encompassing systems in which either the disperse[...] phase or the continuous phase is semi-solid or even solid" (Darling and Birkett, 1986, p.1). This applies to the system studied in this report, which is an oil-in-water (O/W) emulsion where solidified, crystalline triacylglycerol (TAG) molecules are confined within droplets and dispersed in an aqueous continuous phase. Dairy products like UHT milk and heavy cream and spray-dried, powdered products such as infant formulae and dietetic foods are based on this type of O/W emulsion.

TAG emulsions with a semi-crystalline disperse phase are not only used in food applications but also in the pharmaceutical, chemical and cosmetics industry. In order to protect hydrophobic (bioactive) agents and to ensure their targeted and controlled release, these components can be dissolved in a carrier lipid, commonly consisting of TAGs, and be delivered as nano-size, crystalline particles dispersed in an aqueous phase. These systems are called solid-lipid nanoparticles (SLNs), nano-structured lipid carriers or nano-crystal suspensions depending on the use of a solid lipid matrix and the degree of crystallinity of the disperse phase. (Mehnert and Mäder, 2001, Wissing et al., 2003, Bunjes and Koch, 2005, Salminen et al., 2014)

2.1.2 Melt Emulsification of TAG Emulsions with a Semi-Crystalline Disperse Phase

There are several different methods to produce emulsions all of which are referred to as emulsification or homogenisation processes. Their purpose is to reduce and homogenise the size of the disperse phase colloidal droplets. A small and uniform droplet size favours emulsion stability, which is desired in the product applications discussed in this report. As the free energy of the emulsified state is higher than that of the separated phases, there has to be an energy input into a biphasic system to homogenise it. High-energy methods rely on mechanical stresses to disrupt the disperse phase into fine droplets. This mechanical energy is supplied by devices such as rotor-stator systems, colloid mills or high-pressure valve homogenisers. There are less energy-intensive methods that induce phase

inversion or spontaneous formation of emulsion droplets by altering the environmental conditions, such as the pH or the concentration of stabilising agents. (McClements, 2012)

Milk fat and hydrogenated plant fats consist of triacylglycerols, which are mainly or exclusively esterified with saturated fatty acids and therefore solid at room temperature. Crystalline TAG emulsions are traditionally manufactured in a two-step process sometimes described as ‘melt emulsification’, which is depicted in Figure 2-1. In a first step, the fat phase is heated above its melting point and then mixed into the tempered continuous phase. The raw emulsion is then homogenised by one of the emulsification methods described above and subsequently cooled to induce crystallisation and re-solidification of the disperse fat phase. (Abramov et al., 2018)

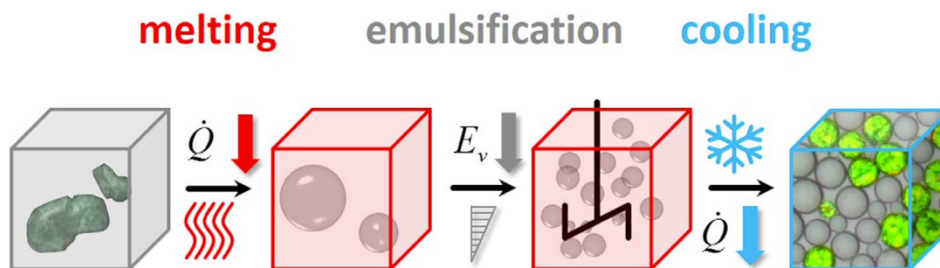


Figure 2-1 Schematic representation of a melt emulsification process, with \dot{Q} = heat transfer rate, E_v = volumetric energy density. Green droplets on the right depict crystallinity as observed under polarised light (Abramov et al., 2017, p.1).

At industrial scale, melt emulsification is mostly performed with rotor-stator systems and the cooling is carried out in stirring tanks or heat exchangers. Stirring tanks have a varying cooling profile and reach only slow to moderate cooling rates of $0.1\text{-}50\text{ K min}^{-1}$ (Reiner et al., 2022). Heat exchanger are more efficient and provide constant cooling conditions but fouling is a commonly encountered problem (Singh and Heldman, 2014).

2.1.3 Crystallisation Behaviour of Triacylglycerols

The crystalline state is marked by a highly ordered atomic arrangement that is periodic in three dimensions. Any crystal structure can be described in terms of the basic repeating unit it is composed of. These building blocks, identical in size, shape and orientation, are called unit cells. The three vectors a , b and c and the three angles α , β and γ allow to characterise all seven possible types of unit cells that can be distinguished. Based on these different unit cell types, any crystal can be classified into one of the so-called crystal systems. (Shirokanev et al., 2019) An overview over their axis systems and symmetries is given in Figure 2-2.

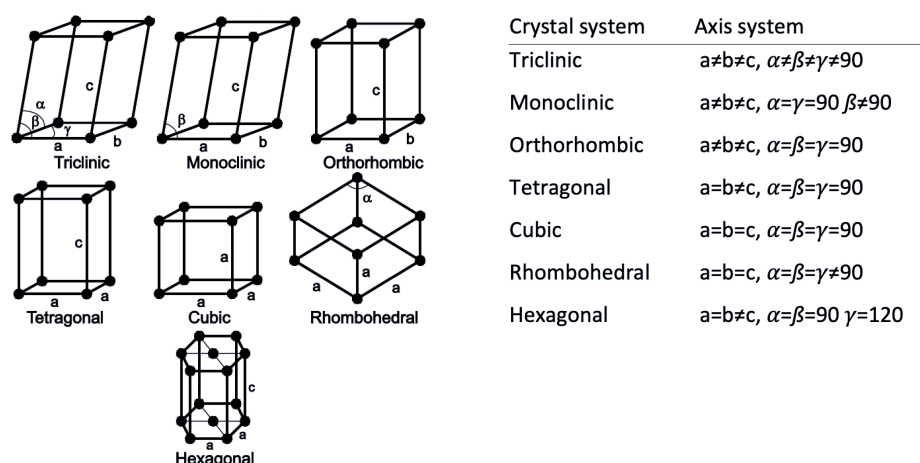


Figure 2-2 Lattice parameters, i.e. angles and vectors, allowing to describe and distinguish a crystal unit cell and to categorise crystals into seven different crystal systems (adopted and modified from Shirokanev et al., 2019).

Triacylglycerols (TAGs) are fats consisting of a glycerol backbone and three fatty acids (FAs) esterified at positions *sn*-1, *sn*-2 and *sn*-3 (see Figure 2-3). FAs are characterised by the length and degree of unsaturation of their aliphatic hydrocarbon chain. Based on this, fatty acids are divided into saturated, mono-, di- and poly-unsaturated FAs and into short-, medium- and long-chain FAs. Monoacid TAGs, containing three identical FAs, can be distinguished from TAGs with mixed fatty acids, the latter existing as positional isomers. The nature and order of the FAs strongly affects the melting and crystallisation behaviour of the TAG molecule. Saturated long-chain FAs increase the melting point of the TAG molecule, while TAGs esterified with short-chain unsaturated FAs are liquid at room temperature. (Pashley and Karaman, 2004, Awad et al., 2008) Depending on the similarity of its fatty acid chains, a TAG at solid state adopts either a chair or tuning fork conformation. In the chair conformation, the FAs in positions *sn*-1 and *sn*-2 are closely aligned and point in the same direction whereas, in the tuning fork conformation, the FAs in positions *sn*-1 and *sn*-3 are running alongside each other. This is illustrated by Figure 2-3.

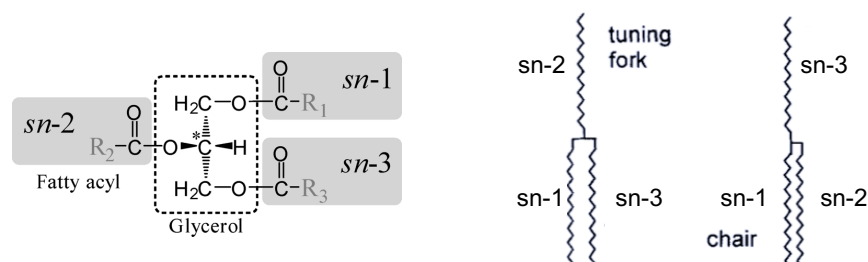


Figure 2-3 Left to right: schematic representation of an exemplary TAG molecule (adopted from Motoyama et al., 2010, p.1245) and tuning fork and chair conformation of two solid state TAG molecules (modified from Coultate, 2002, p.16).

In their solid state, TAGs are crystalline. In a TAG crystal, the TAG molecules may assemble into four different unit cells: hexagonal, monoclinic, orthorhombic or triclinic (Golodnizky et al., 2022). This is dictated by the nature, molecular structure and position of the FAs, that the TAGs are esterified with. (McClements, 2012) The type of unit cell the TAG crystal is built from, classifies it as one specific, so-called polymorph. For TAG crystals, there are mainly three polymorphic form: α , β' and β . Each of them have individual thermodynamic and physicochemical properties, such as the melting point.

This is illustrated for the crystal polymorphs of some monoacid TAGs in Table 2-1.

Table 2-1 Melting point of the three main polymorphic forms of different monoacid triacylglycerols (Coultate, 2002, p.108).

	α	β'	β
Trilaurin	14 °C	43 °C	44 °C
Trimyristin	32 °C	44 °C	56 °C
Tripalmitin	44 °C	56 °C	66 °C
Tristearin	54 °C	64 °C	73 °C

The TAG molecules in the α polymorphic form are in a tuning fork conformation and organised in a hexagonal unit cell (Golodnizky et al., 2022). The alpha polymorph has the lowest melting point and stability. It is characterised by a low packing density. Because of the loose packing structure, α crystals can easily incorporate impurities or TAGs with different FA profiles. This accounts for their high compositional versatility and low purity. (Bayard et al., 2022) The morphology of alpha TAG crystals is spherical. Emulsified TAG molecules that crystallise in the alpha polymorphic form remain confined within the emulsion droplets and these thereby retain their initial size and morphology.

The β' polymorphic form is composed of TAGs in either a chair or a tuning fork conformation, assembled in an orthorhombic or monoclinic unit cell. The β polymorph is characterised by TAGs in a tuning fork conformation, that arrange in a triclinic unit cell. (Golodnizky et al., 2022)

Only TAG molecules, which are similar in terms of the nature and order of their FAs, crystallise in the β form. Due to their similarity, they can pack very densely, which does not allow for impurities to get incorporated. The β polymorphic form therefore has the highest melting point and stability of the three major TAG polymorphs. (Coultate, 2002, McClements, 2012) Dietary fats consist most commonly of a large number of different TAG molecules. Thus, they tend to form crystals with low density and purity (Awad et al., 2008). However, one polymorphic form usually dominates in a specific type of fat, which, in the case of milk fat, is the β' polymorph. (Coultate, 2002)

When TAGs crystallise in the β polymorphic form, they grow into platelet like, highly rigid structures (Coupland, 2002, Bunjes et al., 2007). These are prone to aggregation and network formation/gelation (McClements, 2012). Dispersed TAG crystals with extensive and irregular dimensions are unwanted in the product applications discussed in this report as they accelerate emulsion destabilisation (see 2.1.5). Rapid cooling promotes the formation of crystals with a low packing density as the TAG molecules are not given time to rearrange into an ideal order before being immobilised by solidification. Thus, they often crystallise in the lowest melting, most unstable α form. Accordingly, slowly crystallised TAG molecules tend to pack more densely. (McClements, 2012) Apart from the processing conditions, the size of the liquid emulsion droplets also affects the polymorphic form, that the TAG molecules adopt upon crystallisation. Samtlebe et al. (2012) report that small emulsion droplets crystallise in the alpha polymorph, while larger emulsion droplets contain mostly β crystals, which is related to their higher tendency to undergo polymorphic transitions. The same authors also describe the effect of native milk

phospholipids on the polymorphic behaviour of crystalline milk fat. At high cooling rates, they observed the formation of mixed alpha crystals composed of polar lipids and a high melting milk fat fraction. Conversely, at slow cooling rates, the polar lipids and milk fat molecules crystallise separately into β' crystals.

The β and β' polymorphs of crystalline TAGs have a higher activation energy but a lower free energy than the alpha polymorph. This makes the β' and β forms favourable from a thermodynamic point of view. However, TAGs only rarely exist in the most stable crystal form because the activation energy for the polymorphic transition is not reached. (McClements, 2012) Storage of crystalline TAG emulsions at temperatures slightly above the melting point of the respective crystal polymorph can lead to recrystallisation to more stable polymorphic forms. These polymorphic transitions are always monotropic proceeding from the α over the β' to the β form (Coultate, 2002). High heating and cooling rates delay polymorphic transitions (Awad et al., 2008). TAGs containing short-chain FAs usually transition faster compared to those containing longer FA chains (Awad et al., 2008). In emulsions, polymorphic transitions can induce instability mechanisms.

2.1.4 Crystallisation in Oil-in-Water (O/W) Emulsions

Crystallisation is a liquid-solid first-order phase transition marked by three distinct events: nucleation, propagation and maturation. Even though the solid, crystalline state has a lower free energy and is thermodynamically more stable than the liquid state, crystallisation only occurs once the energy barrier for the formation of crystal nuclei is overcome. Based on classical nucleation theory, “[...] nuclei are believed to consist of small transiently ordered molecular clusters that form when a number of molecules collide and become associated with each other” (McClements, 2012, p.7). The creation of crystal-liquid interfaces upon nucleation leads to interfacial tension that increases the free energy of the system. This thermodynamically unfavourable effect is proportional to the surface of the formed nuclei. There is a critical nucleus radius r^* above which growth of the nucleus is favoured. When reaching r^* the surface effect is outweighed by the decrease in free energy associated with the solid-liquid phase transition. This then dominating negative free energy change is proportional to the volume of the nuclei. When considering nucleation in a liquid bulk fat, the system needs to be cooled below its melting point to a critical temperature T^* to reach the critical nucleus radius. This phenomenon is called supercooling. At some point of supercooling a diffusional barrier builds up and nucleation is inhibited. Thus, there is an optimal temperature where the nucleation rate is highest. Golodnizky et al. (2022) have investigated the nucleation behaviour of triacylglycerols. They claim that the temperature dependence of the nucleation process is due to the conversion rate of the different molecular conformations of the TAG molecules. From the liquid state they have to transition into the tuning fork conformation (see 2.1.1) as this is the one required for a nucleus to form. Conformational changes require a high level of mobility which is achieved at an optimum temperature where the

conversion rate and thus the nucleation rate is highest.

Agitation can help nucleation as it increases the rate of collision between bulk fat molecules. Impurities can promote the formation of fat crystal nuclei by acting as nucleation sites and thereby reducing the nucleation barrier. This however depends on the wettability of the impurity by the fat. Examples of crystallisation-promoting, catalytic impurities are emulsifiers with a molecular structure similar to that of the fat phase (see 2.2.3). (McClements, 2012, Roos and Drusch, 2016) Nucleation induced by impurities is called heterogeneous. Primary heterogeneous nucleation is initiated by catalytic impurities different in nature from the nucleating compound. Secondary nucleation occurs in the presence of so-called crystals seeds, which are existing crystals of the nucleating compound. (Roos and Drusch, 2016) In O/W emulsions, only a minor fraction of the fat droplets crystallises by a heterogeneous nucleation mechanism. That is because the same number of catalytic impurities present in a bulk fat need to distribute over many individually dispersed fat droplets. This lowers the probability for a fat droplet to contain an impurity and increases the level of supercooling required to initiate crystal nucleation. (Walstra and van Beresteyn, 1975) The rate and extent of nuclei formation depends on the fat droplet size. Smaller droplets have a lower melting point because of a higher Laplace pressure. Consequently, more supercooling is needed for nucleation to occur in small droplets. (McClements, 2012) Additionally, bigger droplets have a higher probability of containing a catalytic impurity and to undergo heterogeneous nucleation, which generally occurs at higher temperatures (McClements et al., 1993c, Abramov et al., 2018, Bayard et al., 2022). The droplet size distribution in emulsions is polydisperse and each size class has its own nucleation rate. As a result, every emulsion droplet shows an individual nucleation behaviour. Because the droplets are also isolated from each other, nucleation in one droplet is independent of nucleation in other droplets and does not propagate. Eventually, this results in different fat droplet fractions, some existing as supercooled liquids or amorphous particles and others showing different single or poly-crystalline structures. These droplet fractions vary in their tendency to destabilise and to undergo phase transitions, which favours colloidal instability mechanisms. To achieve an overall high emulsion stability, it is ideal to yield fully crystalline fat droplets that retain their original shape and size. (Coupland, 2002, Awad et al., 2008, Abramov et al., 2017 and, 2018, Reiner et al., 2022)

The nucleation behaviour of the individual emulsion droplets affects the size, morphology and physical state of the fat crystals as they grow. Crystal growth is limited by the finite extensions of the emulsion droplets and proceeds extremely quickly. This also means that a small initial droplet size leads to a smaller final crystal size. (Truong et al., 2014, Abramov et al., 2018, Bayard et al., 2022) In O/W emulsions, crystal growth occurs by diffusion and/or convective transport of fat molecules to the surface of the fat crystal nuclei. The liquid fat molecules need to be oriented correctly to get incorporated into the crystal lattice. (Bund and Hartel, 2010) This process is strongly temperature

dependent. At high temperatures, the uptake of fat molecules into the crystal lattice of the nuclei is the rate-limiting step. At low temperatures, the increasing viscosity of the aqueous continuous phase slows down the diffusional transport of the fat molecules to the nuclei surface and thereby limits crystal growth. (McClements, 2012) Low temperatures due to rapid cooling also restrict the molecular mobility of the fat molecules, which then do not have sufficient time to reach the energetically most favourable site for incorporation. The resulting crystals therefore have a more disorganised structure. (Coupland, 2002) In the case of emulsified TAGs, this favours the formation of α -crystals. In Figure 2-4 the influence of the temperature on the rate of nuclei formation, crystal growth and overall crystallisation rate is depicted. At high levels of supercooling, the rate of nucleation dominates over the rate of propagation and the resulting crystals are small, while at lower levels of supercooling, bigger crystals are formed due to a higher rate of crystal growth. (Roos and Drusch, 2016) A rapid and uniform cooling process therefore generates small crystals with a narrow size distribution (Hartel, 2001).

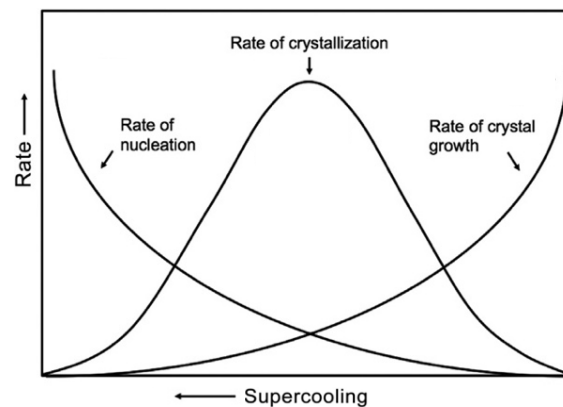


Figure 2-4 Schematic representation of the temperature dependence of crystal nucleation and growth. While the rate of nucleation is higher at higher levels of supercooling, the rate of propagation increases as the temperature increases because of a higher rate of diffusion (adopted and modified from Roos and Drusch, 2016, p.24).

Different faces of the fat crystal may grow at a different rate generating crystal morphologies deviating from that of a perfect sphere. The size and morphology of the fat crystals have an effect on the colloidal stability and the physicochemical properties of the O/W emulsion such as its rheology and appearance. During storage, O/W emulsions may undergo recrystallisation. The fat crystals rearrange to reach a lower energy state, which requires a certain molecular mobility. Recrystallisation is therefore enhanced by fluctuating temperatures and temperatures close to the melting point of the fat phase. It entails changes in the size, number, shape, orientation and degree of purity of the fat crystals. As a result, the overall size of the crystals increases, and the size distribution gets more polydisperse. Often a change from a spherical to a more ellipsoid fat crystal morphology can be observed. These changes trigger instability mechanisms (see 2.1.5) (Bund and Hartel, 2010).

2.1.5 Colloidal Instability Mechanisms in Semi-Crystalline Triacylglycerol Emulsions

There are generally five main mechanisms contributing to colloidal instability of emulsions. These are creaming, aggregation, partial and total coalescence, Ostwald ripening and phase inversion (see Figure

2-5). In food systems, these mechanisms are often coupled as they may occur simultaneously. As an example, a growing particle size, caused by aggregation and coalescence, subsequently promotes creaming. (Vanapalli and Palanuwech, 2022)

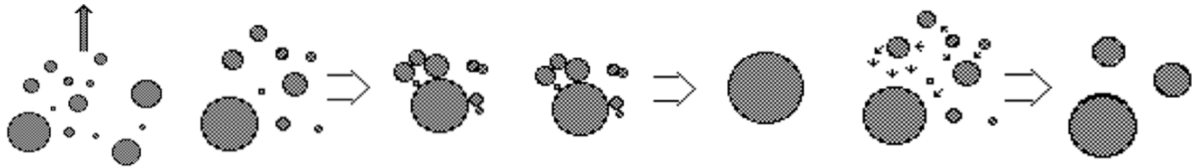


Figure 2-5 Schematic representation of the main colloidal instability mechanisms as found in emulsions (from left to right): creaming, aggregation, coalescence, Ostwald ripening (adopted and modified from Ritzoulis, 2013).

Creaming is a gravity-driven process that arises from density differences between the disperse and the continuous phase. In semi-crystalline triacylglycerol emulsions the lower-density emulsion droplets can thereby separate into a top creamed layer from a bottom serum phase (Rousseau, 2000).

Aggregation is an umbrella term for “[...] a variety of particle-particle interaction processes.” (Darling and Birkett, 1986, p.17). One of these processes is flocculation, which “[...] describe[s] any aggregation process in which droplets retain their identity.” (Darling and Birkett, 1986, p.14). Flocculating emulsion droplets form clusters, which increases the effective droplet size (Vanapalli and Palanuwech, 2022). Flocculation occurs due to repulsive forces being insufficient to oppose the attractive forces acting between emulsion droplets. As the range differs over which these forces are effective, flocculation is highly dependent on the inter-particle distance.

The solubility of TAGs in water is poor but finite. In semi-crystalline triacylglycerol emulsions, diffusion of liquid TAG molecules across the aqueous continuous phase therefore actually occurs. There are three different mass transport processes in O/W emulsions that can be distinguished. Ostwald ripening is driven by the difference in Laplace pressure in small and large emulsion droplets, which is related to the curvature of the droplet surface. Ostwald ripening leads to larger droplets growing at the expense of small droplets (Darling and Birkett, 1986). Compositional ripening occurs between emulsion droplets differing in their composition. This may for instance concern supercooled liquid, semi-solid and fully crystalline fractions of emulsion droplets or emulsion droplets containing high, middle and low melting fractions of TAG molecules from a complex natural fat. Solubilisation is a mass transport process that involves liquid oil molecules moving out of the emulsion droplets and into the aqueous phase. (Weiss and McClements, 2000) All of these processes are thermodynamically driven by the entropy of mixing. Upon homogenisation and crystallisation, emulsion droplets differing in terms of their size (i.e. different Laplace pressure), state (i.e. supercooled liquid, semi-solid or fully crystalline) and composition (i.e. HMF, MMF or LMF of mixed TAGs) are created. This leads to a different chemical potential in the different compartments of the total emulsion system and is entropically unfavourable. The system strives towards an equilibrium distribution of the different TAG molecules amongst all emulsion droplets and between the continuous and disperse phase. (McClements et al., 1993b) The rate of this distribution process depends on the solubility of the TAG molecules in the continuous

phase. Small triacylglycerols with short-chain FAs diffuse faster due to their higher polarity. The solubility of TAGs is also increased in the presence of co-solutes that lower the polarity of the aqueous continuous phase. This has been proven for the addition of ethanol to a solid lipid nanoparticle emulsion, that led to a higher mass transport rate of MCT molecules from liquid emulsion droplets to SLNs consisting of hydrogenated palm oil. (Samtlebe et al., 2012) There are other co-solutes, namely proteins and micelle-forming emulsifiers, that can incorporate or bind TAG molecules and thereby affect the mass transport rate. Weiss and McClements (2000) studied tetradecane emulsions stabilised by different non-ionic emulsifiers, added above their critical micelle concentration. They hypothesise that the excess, non-adsorbed emulsifier forms micelles in the aqueous continuous phase, which incorporate tetradecane molecules in their hydrophobic core. McClements et al. (1993b) showed that the inter-droplet exchange rate of hexadecane molecules in an O/W emulsion increased with increasing concentration of added whey protein isolate. The authors related the observed phenomenon to the β -barrel type structure of β -lactoglobulin, the main whey protein fraction (see 2.2.1). This hydrophobic region of the β -lactoglobulin structure allows binding and transportation of apolar ligands such as alkanes, triacylglycerols and fatty acids. In the same study, the mass transport rate was also found to be proportional to the specific surface area of the emulsion droplets.

Coalescence occurs upon droplet collision and is due to oscillations, i.e. emulsifier desorption or displacement (Marangoni effect), in the interfacial film. A high volume fraction of the disperse phase increases the rate of coalescence as collisions between particles are more frequent. The probability of colliding droplets to coalesce depends on the adsorption kinetics and the stabilising mechanism of the emulsifiers covering the droplet surface. Coalescence is limited in emulsions with a disperse phase fraction of less than 1 wt% and a high emulsifier concentration. The latter ensures an efficient coverage of the droplet surfaces and a thick, highly viscoelastic interfacial layer. (Pichot et al., 2013, Taboada et al., 2020) A high interfacial viscosity limits fluctuations in the density of adsorbed emulsifier molecules and thereby counteracts coalescence upon collision (Bos and van Vliet, 2001). The extent of coalescence also depends on the nature of the disperse phase; coalescence may be complete when considering fully liquid emulsion droplets or partial if the emulsion droplets are (semi-)crystalline (Rousseau, 2000).

Partial coalescence occurs in emulsions with a semi-crystalline disperse phase where the crystals are located at the surface of the emulsion droplets and protrude into the continuous phase. Upon collision of two emulsion droplets, the protruding crystals penetrate the interfacial film of the other droplet and form a bridge, which gets wetted by liquid disperse phase material. The droplets form irregularly shaped clusters but do not fuse entirely because the internal crystal network, built up in the individual droplets, is strong enough to maintain the droplet integrity. (Coupland, 2002, McClements, 2012, Vanapalli and Palanuwech, 2022) Upon melting, this internal crystal network can collapse. The partially

coalesced droplets then merge into one bigger droplet. This is then considered as true coalescence. (Rousseau, 2000) The mechanism is shown in Figure 2-6.

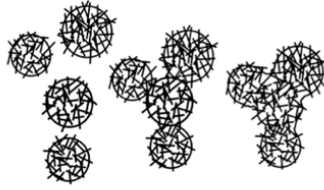


Figure 2-6 Schematic representation of semi-crystalline emulsion droplets with protruding crystals that undergo partial (middle) and total (right) coalescence (Rousseau, 2000, p.11).

In O/W emulsions, the rate and extent at which partial coalescence occurs, depends on a number of factors among which are the composition and volume fraction of the disperse phase, the crystal size, polymorphism and morphology, the nature of the emulsifier establishing the interfacial film and the shear rate. Partial coalescence is promoted by a high shear rate and low viscosity of the continuous phase as these increase the rate and probability of collision. A high volume fraction of disperse phase decreases the inter-particle distance. Big, rigid crystals with a platelet-like morphology enhance partial coalescence. Stable polymorphs form more rigid crystals (see 2.1.1). This makes them less sensitive to the bending conferred by the curvature of the emulsion droplet surface. The crystals are thereby more likely to penetrate the interfacial layer and to induce partial coalescence. (Coupland, 2002) The cooling rate has an impact on the size and number of crystals formed and on the fat polymorphism, which in turn determines the morphology of the crystals (see 2.1.1). A small droplet size confines crystals to grow in a smaller volume thereby reducing the crystal size. Smaller crystals can be efficiently stabilised by the addition of low molecular weight emulsifiers (LMWE) (see 2.2.1). The nature and concentration of the emulsifier also influences the thickness, rigidity/viscosity and repulsive forces of the interfacial film (see 2.2.1 and 2.2.2). A thin, non-elastic interfacial film is more easily pierced by fat crystals, which induces partial coalescence. (Bergenståhl and Alander, 1997, Coupland, 2002, McClements, 2012, Truong et al., 2014, Vanapalli and Palanuwech, 2022)

Transitions of TAG crystals from one polymorphic form into another (see 2.1.3) promote aggregation. That is because the restructuring and reformation of the crystals leads to the exposition of uncovered hydrophobic patches, which attract one another. Polymorphic transitions may also entail crystal shape transformations, resulting in a more platelet-like morphology of the TAG crystals. The latter is known to promote partial coalescence. (Awad et al., 2008, McClements, 2012, Salminen et al., 2014) While big fat crystals and TAG molecules with short-chain FAs undergo fast polymorphic transitions, the process can be slowed down by the addition of lipid based LMWE and the control of the storage and processing temperature (see 2.1.3).

2.2 Stabilising Oil-Water-Interfaces with Food-Grade Emulsifiers

2.2.1 Properties and Categories of Food-Grade Emulsifiers

A fundamental prerequisite for a molecule to act as an emulsifier is for it to display surface activity. Molecules consisting of clearly separated hydrophilic and hydrophobic domains are surface active. This feature is termed amphiphilicity. (Coultate, 2002) In O/W emulsions, the hydrophobic parts of the emulsifier molecules orient towards the fat phase whereas the hydrophilic parts orient towards the continuous aqueous phase. Adsorption of emulsifier molecules to the oil-water interface lowers the interfacial tension. The drop in surface tension, described by the surface pressure, depends on the adsorption kinetics, adsorption isotherm and molecular structure (morphology and charge) of the emulsifier. Generally, emulsifiers promote emulsion stability by increasing the interfacial viscosity and by enhancing repulsive forces such as electrostatic and steric repulsion, which oppose attractive forces that act between the emulsion droplets. The stabilising mechanism differentiates emulsifiers from stabilisers or thickening agents, the latter acting by increasing the viscosity of the continuous phase (e.g., by network formation/gel) to immobilise emulsion droplets. (Goodwin, 2004)

Food-grade systems used to stabilise emulsions include low molecular weight emulsifiers (LMWE), macromolecules, Pickering particles and microgels. Common macromolecular emulsifiers in food applications are proteins and polymers such as modified starches and celluloses. The most common proteins used as emulsifiers are whey protein isolates (WPI) and caseinates sourced from milk. (Rayner, 2015) The structure and properties of a protein are determined by its specific amino acid sequence. Depending on their functional group, amino acids are either hydrophilic or hydrophobic in nature. Blocks of hydrophilic amino acids and patches with predominantly hydrophobic amino acids make the protein molecule amphiphilic. This accounts for the surface activity generally displayed by proteins. Many proteinogenic amino acids have ionisable functional groups. Their charge is influenced by the pH of the surrounding medium. The pH at which the number of positively and negatively charged groups is equal, is called the isoelectric point (IP) of the protein. At the isoelectric point, a protein reaches its lowest solubility and highest susceptibility for denaturation. (Coultate, 2002)

The stabilisation mechanism of food-grade emulsifiers differs in nature and extent. Proteins adsorb to and unfold at emulsion interfaces. Lateral interactions between the adsorbed protein molecules via non-covalent mechanisms and/or disulphide cross-linking contribute to the creation of a highly viscoelastic interfacial film. (Bos and van Vliet, 2001) Viscoelasticity is important for protecting emulsions droplets against coalescence (Heiden-Hecht and Drusch, 2022). The unfolding leads to the exposition of hydrophobic parts of the protein. These segments then adsorb to the interface in train conformations. Conversely, the hydrophilic parts protrude from the interface reaching out into the continuous phase in tail and loop conformations. (Coultate, 2002) This results in a good steric stability and an interfacial layer resistant to coalescence and mechanical stresses (McClements et al., 1993a).

Denaturation, at least to a certain extent, is required for proteins to undergo conformational changes upon adsorption (Darling and Birkett, 1986). These unfolding processes slow down the adsorption process. Diffusion to the interfaces also takes longer for proteins as compared to LMWEs as proteins are much larger (Taboada et al., 2020).

Caseins are random-coil proteins lacking secondary or tertiary structure. This disordered molecular conformation allows them to flexibly and rapidly adsorb to emulsion interfaces providing a good resistance to heat and pressure treatments (Bos and van Vliet, 2001, Truong et al., 2014). Caseins adsorb at higher surface concentrations and show more pronounced surface activity as compared to whey proteins (Relkin et al., 2003). They form interfacial layers of about 10 nm in thickness (Bayard et al., 2022). Conversely, beta lactoglobulin (β -lg), the main whey protein fraction, is a globular protein with a highly ordered, rigid structure. Upon interfacial adsorption, unfolding of β -lg is limited but can be enhanced by heat denaturation. When heated, β -lg exposes its hydrophobic patches leading to aggregation and restructuring. (Truong et al., 2014, Rayner, 2015) Beta lactoglobulin molecules, adsorbed to oil-water interfaces, can polymerise via disulphide bridging. This can exert an overall destabilising effect when leading to inter-droplet bridging and subsequent flocculation. However, when limited to the individual droplet surfaces, bridging of β -lg molecules has a favourable effect on the emulsion stability by increasing the interfacial viscosity. This increase can be two orders of magnitude higher than that of flexible proteins like caseins (Bos and van Vliet, 2001). The resulting interfacial layer is about 2 nm thick. (Bayard et al., 2022) Generally, the lower the conformational flexibility of the protein, the higher the viscoelastic modulus of the created interfacial adsorption layer (Rousseau, 2000). The different interfacial conformations of rigid and less structured proteins are illustrated in Figure 2-7.

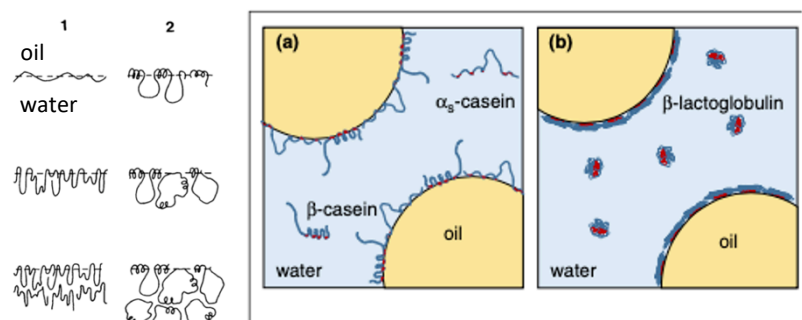


Figure 2-7 Left to right: Schematic representation of the conformation of a generic random-coil protein (1) as opposed to a globular protein (2) upon adsorption to an emulsion interface with increasing protein concentration from top to bottom (Darling and Birkett, 1986, p.11). Schematic representation of the interfacial conformation of caseins (left) and β -lactoglobulin (right) upon adsorption to an oil droplet surface (dimensions not to scale) (Rayner, 2015, p.100).

Low molecular weight emulsifiers used in food applications are mainly lipid based, like mono- and diacylglycerols and phospholipids. Phospholipids (PL) consist of a glycerol backbone esterified with two fatty acids of varying degree of saturation and chain length and a hydrophilic, phosphate-containing headgroup (Pichot et al., 2013). The overall structure of a phospholipid molecule and the main headgroups found in milk PLs are shown in Figure 2-8.

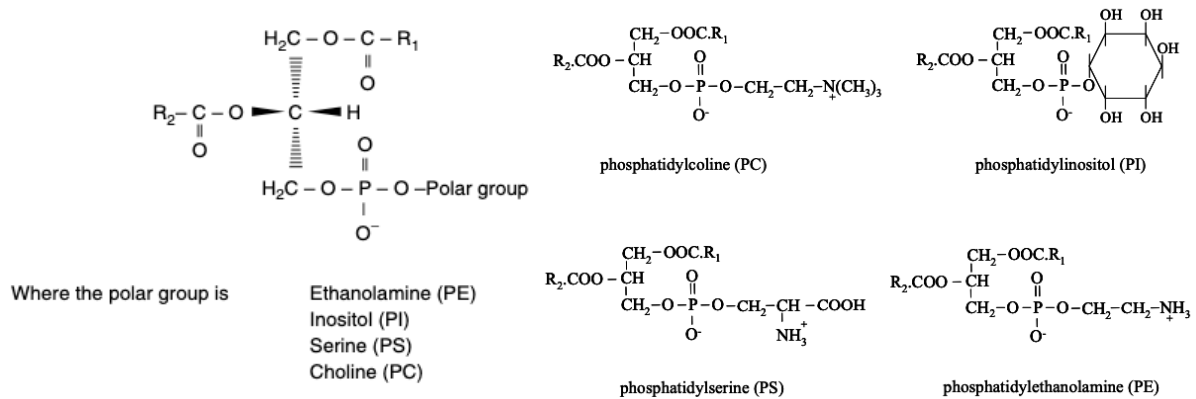
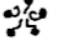


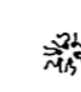
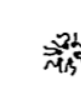


Figure 2-8 (From left to right) Fischer projection of a glycerophospholipid (Wright and Marangoni, 2006, p.20) and structure of the most common hydrophilic head groups found in milk phospholipids (Contarini and Povolo, 2013, p.2810).

Phosphatidylcholines (PC) and phosphatidylethanolamines (PE) are two subgroups of phospholipids having zwitterionic character. In a pH range of 4-7.5, they are overall neutral (Akimov et al., 2018). PCs with a FA chain length identical to their PE counterpart have a higher melting point (Tian and Chius, 2018). The choline headgroup is larger in size compared to ethanolamine, which accounts for the different geometry of PCs and PEs. While PCs, with their large headgroup, have a morphology of a truncated cone, the hydrophobic moiety dominates over the comparably smaller headgroup in PEs (Salminen et al., 2014). The balance between the hydrophobic and the hydrophilic part of a LMWE is the basis of the classification system called the hydrophilic-lipophilic balance (HLB) concept. The HLB concept allows to quantitatively describe the emulsifying capacity of a given emulsifier on a scale from 0 to 20. An HLB value between eight to 18, indicating a high hydrophilicity and water solubility, is required for O/W emulsions (Coultate, 2002). In O/W emulsions with a crystalline disperse phase, the adsorption of hydrophilic emulsifiers can enhance emulsion destabilisation as they increase the wettability of the fat crystals by the aqueous phase (Bergenståhl and Alander, 1997). The HLB value of a LMWE is directly correlated to its chemical structure and allows to predict the geometry of the structures that it assembles in, when in an environment with a surplus of water. PCs are reported to form more compact interfacial monolayers when used as emulsifier in O/W emulsions as compared to PEs. This confers better stability and is related to the PC molecule being in a liquid condensed state as opposed to PEs being in a liquid expanded state. (Handa et al., 1990) Friberg (1997) was the first to claim that O/W emulsion interfaces could be stabilised by lipid based LMWEs in their lamellar liquid phase forming interfacial films. In Figure 2-9 the liquid lamellar phase structures formed by soy PC, PE and phosphatidylinositol are depicted.

	Hydrophilic		Hydrophobic			
	Micellar	Hexagonal	Lamellar	Cubic	Reversed Hexagonal	Reversed Micellar
						
Phospholipids:						
Soybean PC			—			
Soybean PE					—	
Soybean PI			—			

Current Opinion in Colloid & Interface Science

Figure 2-9 Self-assembly structures of soybean phospholipids formed at surplus of water (adopted and modified from Bergenst ahl and Alander, 1997, p.591).

When added to an O/W emulsion, phospholipids adsorb to the oil-water-interfaces orienting their headgroups towards the aqueous phase. LMWEs stabilise emulsions based on the Gibbs-Marangoni effect and electrostatic effects (Heiden-Hecht and Drusch, 2022). They form interfacial films with a low layer thickness corresponding to the size of their hydrophilic headgroup (McClements et al., 1993a). This makes emulsion droplets stabilised with LMWEs more prone to (partial) coalescence.

Interactions with water in aqueous environments lead to the hydration of the PL. Hydrated PCs have been shown to bind with each other upon interfacial adsorption if added above their critical micelle concentration (CMC). This results in an aggregation of the hydrated PCs and ultimately in the formation of a 3D adsorption layer (Shchipunov and Kolpakov, 1991). The swelling behaviour of a PL depends on the nature of its headgroup. Ionisable headgroups are positively charged at low pH and attract negatively charged ions from the surrounding aqueous phase (Coultate, 2002). Thereby, a repulsive barrier builds up, which protects the emulsion droplet against coalescence as depicted in Figure 2-10.

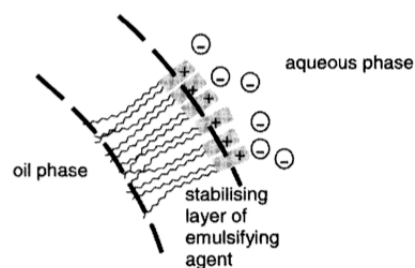


Figure 2-10 Adsorption of phospholipid molecules to an oil-water interface at low pH (Coultate, 2002, p.115).

If added in high amounts, PLs tend to form multilayers at O/W emulsion interfaces (Hernqvist, 1986, Pichot et al., 2013). A schematic representation of this phenomenon is given in Figure 2-11. Heiden-Hecht and Drusch (2022) reported multilayer and network formation for crystalline PC molecules adsorbed to O/W interfaces. Adsorption of multiple layers of PLs amplifies the effect of PLs to decrease the surface tension across emulsion interfaces and improves the steric stabilisation provided by the thicker interfacial layer.

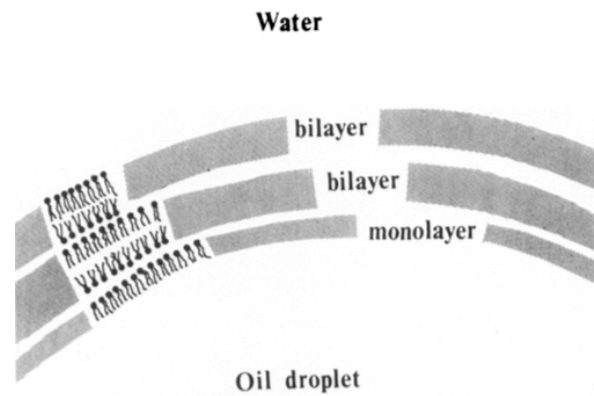


Figure 2-11 Multi-layered interfacial film formed by adsorption of phospholipids to an O/W emulsion at high concentration (Hernqvist, 1986, p.159).

LMWEs generally have a high mobility and diffusion rate and thus show fast adsorption kinetics, which is due to their small size (Taboada et al., 2020). However, depending on the structures formed above the CMC, the rate of adsorption can vary for different LMWEs. Phospholipids commonly associate in big complexes such as liposomes and bilayers, which slows down adsorption. In stabilisation of SLNs, this limited mobility of phospholipids when added in excess, has been shown to lead to an inefficient adsorption and coverage of the emulsion droplet surfaces. (Westesen and Siekmann, 1997, Salminen et al., 2014). Westesen and Siekmann (1997) found that phospholipid stabilised SLNs undergo gelation due to recrystallisation that causes aggregation between uncovered crystal interfaces. The diffusion rate of phospholipids to emulsion interfaces can also be lowered if the degree of saturation of the phospholipid is highly similar to that of the fat phase. Heiden-Hecht and Drusch (2022) have reported this effect when studying the adsorption of PC to emulsion interfaces stabilised with whey proteins. They claim that the highly saturated PC molecules tend to get integrated into the packing structure of the fat, which hinders them from adsorbing to the emulsion droplet surface. This lowers the interfacial load and coverage and increases the concentration required to yield a monolayer formation. It also restricts the ability of PC to efficiently lower the interfacial tension. As a consequence, the stabilising effect of the phospholipid is impaired.

LMWEs have a higher interfacial activity than macromolecular emulsifiers. Due to their smaller size, LMWEs have a higher packing density leading to a more efficient reduction of the surface tension when adsorbing to emulsion interfaces. This is argued to account for the generally small oil droplet sizes that can be attained in emulsions stabilised with LMWEs (Taboada et al., 2020, Heiden-Hecht et al., 2021).

2.2.2 Combination of Food-Grade Emulsifiers

Generally, when combining emulsifiers, either associative, competitive or multi-layer adsorption may occur. This depends on the molecular structure and concentration of the added emulsifiers.

When different proteins compete for adsorption at emulsion interfaces, globular proteins tend to be displaced by more flexible proteins, such as caseins, as these undergo conformational changes more easily and rapidly (Bos and van Vliet, 2001).

Due to their fast adsorption kinetics and high interfacial activity, LMWEs are very efficient in stabilising newly created, uncovered oil-water interfaces and in displacing proteins adsorbed at existing interfaces (Heiden-Hecht et al., 2021, Heiden-Hecht and Drusch, 2022). Water-soluble LMWEs show stronger displacement of proteins from the interface than oil soluble LMWEs. That is because they act in the vicinity of the adsorbed protein layer, which is not equally distributed on both sides of the interface but located closer to the water phase (see Figure 2-7).

Whether cooperative or competitive interaction dominates in multi-emulsifier systems is highly concentration dependent. Bylaite et al. (2000) have found that low concentrations of soybean lecithin increased the amount of β -lactoglobulin adsorbed to the olive oil-water interface in emulsions, while high concentrations of soybean lecithin led to a decrease in the protein surface coverage. However, a complete displacement was not observed even at high phospholipid : protein ratios. Studies on spray-dried emulsions stabilised with whey proteins and lecithins have shown that the two emulsifiers coexist at the interface and exert a synergistic effect, provided that the amount of LMWE is below and the amount of protein is above their critical micelle and critical interfacial concentration respectively. Ratios of 1 to 0.1 to 0.01 wt% of medium-chain triacylglycerols (MCT) to whey protein to lecithins has been proven to substantially improve the stabilisation of the emulsions droplets against coalescence by raising the interfacial tension and lowering the emulsion droplet size. (Taboada et al., 2020, Heiden-Hecht et al., 2021)

In mixed-emulsifier surface films, proteins and low molecular weight emulsifiers may interact via hydrogen bonding, hydrophobic and electrostatic effects. The latter strongly depend on the pKa and isoelectric point of the LMWE and the protein respectively and on the pH and ionic strength of the aqueous phase. Hydrophobic effects arise from the interaction of the hydrophobic tail of LMWEs and the hydrophobic core of proteins. Co-existence of emulsifiers influences the viscoelasticity of the interfacial film with attractive interactions promoting high viscoelasticity as opposed to repulsive or hydrophobic interactions decreasing interfacial viscoelasticity. (Heiden-Hecht et al., 2021, Heiden-Hecht and Drusch, 2022) Complexation of LMWEs and proteins at emulsion interfaces affects the structure and local concentration of the constituent emulsifiers. This may alter their adsorption behaviour and surface activity. Complexed emulsifiers may even display higher surface activity as compared to the individual constituents. (Bos and van Vliet, 2001)

2.2.3 Impact of Food-Grade Emulsifiers on Triacylglycerol Crystallisation

Lipid based LMWEs can promote nucleation in O/W emulsions via interfacial or bulk effects depending on their solubility and their partitioning between the continuous and disperse phase (Bayard et al., 2022). As this project focuses on phospholipids and because these have a high interfacial activity and thus localise at the oil-water-interface, interfacial effects will be discussed in the following.

Upon adsorption to the oil-water-interphase, lipid based LMWEs decrease the interfacial tension, which reduces the activation energy for nuclei formation. This makes nucleation thermodynamically more favourable (McClements et al., 1993c, McClements, 2012). The tails of lipid based LMWEs, being oriented towards the disperse fat phase in O/W emulsions, can initiate surface heterogeneous nucleation by conferring a certain degree of order to neighbouring TAG molecules (McClements et al., 1993c, Bunjes and Koch, 2005). This phenomenon is called template effect and depends on the molecular structure of the lipid based LMWE. The higher the similarity in terms of chain length and degree of saturation between the LMWE and the oil phase, the more pronounced is the template effect (McClements et al., 1993c, Coupland, 2002, McClements, 2012, Truong et al., 2014). As the tails of the lipid based LMWE crystallise prior to the disperse fat phase, they act as nucleation site inducing nuclei formation in the emulsion droplets. The template effect increases the rate of nucleation and onset of crystallisation temperature in O/W emulsions. (Bunjes and Koch, 2005)

Heiden-Hecht and Drusch (2022) report that PC molecules, if reaching a high coverage at O/W emulsion interfaces, form a network upon crystallisation. This network formation induces a shape transformation of the emulsion droplets, which was observed to be especially pronounced when adding PCs with long saturated FA tails.

LMWEs have also been shown to have an impact on the polymorphic behaviour of crystallised emulsion droplets in O/W emulsions. Bunjes and Koch (2005) observed retarded polymorphic transitions in emulsified TAGs upon addition of phospholipids with similar molecular structure to that of the disperse fat phase. 60-64 % of the emulsified, saturated TAGs stabilised with a saturated PC phospholipid remained in the alpha polymorph even after one year of storage. Conversely, emulsions with added native soy lecithin, containing a high fraction of oleic acid, transitioned into the β polymorph nearly directly after the onset of crystallisation. Both Bunjes and Koch (2005) and Bayard et al. (2022) hypothesise that this effect might be due to the restriction of fluidity and mobility of the TAG crystals by the crystalline phospholipids at the interface, inhibiting crystal rearrangement. As polymorphic transitions have been shown to promote emulsion instability (see 2.1.5), this inhibitory effect of LMWEs on polymorphic transitions is assumed to contribute to improved colloidal stability in emulsions.

Proteins do not initiate surface heterogeneous nucleation as seen with lipid based LMWEs (Truong et al., 2014). That is because their hydrophobic patches lack compatibility with the chemical structure of the emulsified TAGs and thus, they do not get incorporated into compound fat crystals (Heiden-Hecht et al., 2021). Depending on the type of protein used as emulsifier, there is however evidence for a different effect on the rate of supercooling. Relkin et al. (2003) report that emulsions of hydrogenated palm oil showed higher supercooling when stabilised with a mixture of whey proteins and caseins as compared to emulsions stabilised with whey proteins alone.

2.3 Colloidal Structure of Milk

Cow's milk, in the following termed 'milk', is a colloidal dispersion with an aqueous continuous phase and a dispersed fat phase. The main constituent of milk is water, making up 87 % of the total mass on average. Depending on seasonal factors and the cow's genetics and diet, milk contains around 2.5-6.0 wt% fat. The remaining 9 wt% are solids, which are suspended or dissolved in the aqueous continuous phase (serum phase). These are mainly proteins, lactose and mineral salts. Milk also contains trace amounts of vitamins, enzymes, pigments and organic acids. Caseins constitute the major protein fraction in milk. They assemble in specific structures, which are suspended in the serum phase. The other milk solids are solubilised in the aqueous continuous phase, while the fat fraction is dispersed as droplets. Thus, the colloidal structure of milk is both that of an O/W emulsion, a suspension and a true solution. (Bylund, 1995) Milk is either homogenised by high pressure homogenisation reaching peak pressures of 200 MPa or by conventional homogenisation. The latter is most commonly performed as a two-step process: The milk is preheated to 50-60 °C and then forced through a first stage valve under a pressure of 10-30 MPa. This creates rupture forces such as shear, turbulence and cavitation, and breaks up the milk fat globules (MFG). A second stage valve is passed at a lower pressure of about 3-5 MPa to separate agglomerating fat globules. Both methods result in similar MFG sizes. (Truong et al., 2016)

2.3.1 Dairy Proteins

Dairy proteins are divided into two main fractions: whey proteins and caseins. Caseins make up the majority of all dairy proteins and about 2.6 wt% of the total mass of milk. When present in the serum phase of milk, the casein molecules form distinct structures of about 0.4 µm in size, which are called casein micelles (Bylund, 1995) There are mainly four other protein types found in milk, that are grouped together as whey proteins. These are α -lactalbumin, β -lactoglobulin (β -lg), BSA (blood serum albumin) and immunoglobulins. Whey proteins also comprise a number of minor compounds such as lactoferrin, glycoproteins, blood transferrin and proteoso-peptones. All whey proteins have a globular, compact structure. They are more hydrated than caseins but significantly more heat-sensitive. Denaturation starts at about 65 °C and is almost complete when heating to 90 °C and holding for 5 minutes. Beta lactoglobulin constitutes the major whey protein fraction making up roughly 10 wt% of all dairy proteins. It contains a free thiol group, which is exposed upon heating and induces inter-molecular aggregation and gelation. A third of the total amount of β -lg is denatured after 30 min heat treatment at 75 °C. (Macej et al., 2002) Milk has a pH of around 6.5 to 6.7. The isoelectric point of β -lg and that of sodium caseinate are close to 5.2 and 4.6 respectively (O'Mahony and Fox, 2014). These proteins therefore have a net negative charge when present in the native serum phase of milk.

2.3.2 Dairy Fat

The fat content of milk can vary significantly. Values in the range of 3.5 to 4.7 wt% are most common. Milk fat consists almost exclusively of triacylglycerols. Other minor components are phospholipids, di- and monoacylglycerols, free fatty acids, sterols, carotenoids and fat-soluble vitamins. Milk fat is one of the most complex natural fats; at least 200 different TAGs and over 400 different FAs have been found in milk. This great compositional variety has an important impact on the key properties of milk fat such as the melting and crystallisation behaviour. Every TAG molecule with its individual FA composition and arrangement has a distinct melting point. This widens the melting range of milk fat to temperatures as low as -40 to up to 40 °C. Triacylglycerols with similar structure and thus similar melting point are grouped into fractions. In calorimetric measurements, these fractions appear as three overlapping endothermic peaks and are termed low melting (LMF), middle melting (MMF) and high melting (HMF) fraction. (Logan et al., 2021, Bayard et al., 2022) Upon heating, the proportion of TAGs containing fatty acids with the shortest chain length and the highest level of unsaturation (LMF) melt at the lowest temperatures. Triacylglycerols with longer and more saturated FA chains can dissolve in the low melting liquified fat fraction. Only once the temperature is raised above the melting point of the highest melting TAG fraction (HMF), the milk fat is completely liquid. (Coultate, 2002) The complex composition of milk fat also makes it difficult to determine the exact concentration of the individual fatty acids, which is therefore commonly indicated as a concentration range and not a single discrete value. The most abundant FAs in milk fat are oleic, myristic, stearic and palmitic acid all of which qualify as long-chain FAs. (Wright and Marangoni, 2006, Truong et al., 2016) Milk fat is an overall saturated fat and solid at room temperature. Table 2-2 gives an overview over the main FAs, their structure and approximate amount.

Table 2-2 Molecular structure and concentration of the principal fatty acids in milk fat (modified from Bylund, 1995, p.19).

Fatty acid	Molecular structure	Percentage of total FAs [%]
Butyric acid	4:0	3.0-4.5
Caproic acid	6:0	1.3-2.2
Caprylic acid	8:0	0.8-2.5
Capric acid	10:0	1.8-3.8
Lauric acid	12:0	2.0-5.0
Myristic acid	14:0	7.0-11
Palmitic acid	16:0	25-29
Stearic acid	18:0	7.0-3.0
Oleic acid	18:1	30-40
Linoleic acid	18:2, ω -6	2.0-3.0
Linolenic acid	18:3, ω -3	up to 1.0
Arachidonic acid	20:4, ω -6	up to 1.0

The fat in milk is dispersed as colloidal droplets in the aqueous continuous phase. These milk fat globules have a broad size distribution ranging from 0.03 to 11 μm with a peak value of 4 μm . Based on a number weighted average, 80 % of the MFGs have a size within the submicron range. In volume based size distributions, intermediate droplet diameters of 1-8 μm predominate. The size of the milk fat globules affects their physicochemical properties; some effects are shown in Figure 2-12.

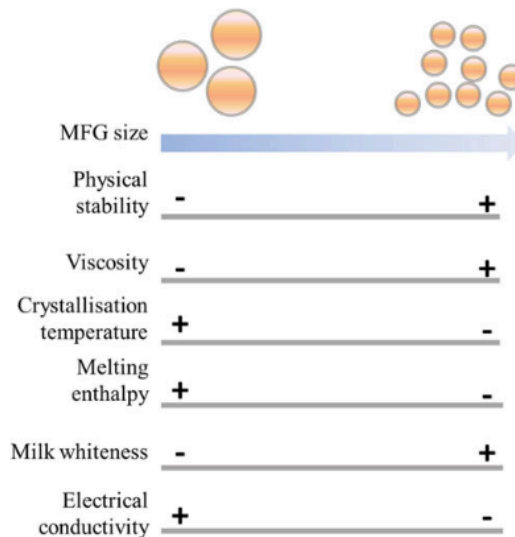


Figure 2-12 Illustration of the impact of the size of milk fat globules on their physicochemical properties (Truong et al., 2016, p.36).

The milk fat globules are stabilised by a membrane with a thickness of 5-10 nm and a complex composition including proteins and polar lipids such as glycerophospholipids and glycosphingolipids. This stabilising layer gives the MFG a net negative charge. Upon homogenisation, it gets ruptured and reforms with a different composition. (Truong et al., 2016)

Glycerophospholipids account for about 0.5-1 wt% of the total milk fat. Other than associated to the MFG membrane, they are also found in the serum phase as their amphiphilic nature allows them to exist in an aqueous environment. PE and PC are the most abundant glycerophospholipids in milk. The PE fraction is highly unsaturated, while the PC fraction is mainly saturated. The most common FAs are stearic, palmitic, oleic and arachidic acid. Very long FAs are however generally rare. (Wright and Marangoni, 2006, Contarini and Povolo, 2013)

2.3.3 Dairy Sugar

Lactose is the main carbohydrate and the second most abundant component in milk making up about 4.8 % of the total mass. Lactose is a disaccharide consisting of a glucose and a galactose unit linked by a β -1,4 glycosidic linkage. As a reducing sugar, lactose can participate in the Maillard reaction by reacting with the free amino groups of milk proteins under high temperatures. This leads to a quality loss in terms of browning, a deterioration of the nutritional value and the formation of free radicals and off-flavours. (Bylund, 1995)

In dairy products, lactose occurs as an amorphous solid or in either of its two crystalline stereoisomers: the α -monohydrate or the β -anhydrous form. One anomer can convert into the other via mutarotation; an equilibrium is reached at a ratio of 1:1.7 of the α - to the β -form. Lactose in solution contains both crystal forms. Lactose solubility is temperature dependent and strongly influenced by the presence of other solutes. In milk, the solubility of lactose is reduced by the water binding capacity of the dairy proteins. Mineral salts such as potassium and sodium phosphate also have an impact on lactose solubility by exhibiting either a “[...] water-structure-making [...]” or a “[...] water-structure-breaking [...]” effect (Huppertz and Gazi, 2016, p.6844). In powdered dairy products, lactose is mostly present as an amorphous solid in its glassy state. That is because the water removal upon spray drying is so rapid that it restricts the molecular mobility to an extent that crystallisation is inhibited. While crystalline lactose shows only little hygroscopicity, amorphous lactose is highly hygroscopic. Because of the plasticizing effect of water, the entry of water to powdered dairy products entails recrystallisation of the amorphous lactose. The same phenomenon is observed if the temperature is raised above the glass transition temperature of lactose. Lactose recrystallisation leads to an increased milk fat mobility and results in stickiness and caking and finally a loss of product quality. (Huppertz and Gazi, 2016, Roos and Drusch, 2016)

3 Objectives and Hypotheses

3.1 Objectives and Motivation of the Study Design

Crystallising emulsified triacylglycerols with a mixed FA profile is challenging. That is both because crystallisation of fats in their emulsified state mainly proceeds via a homogenous nucleation process, thereby requiring a high level of supercooling, and because TAGs that are composed of FAs with different chain lengths and degrees of unsaturation each have an individual melting point. This is why natural fats, when used as the disperse phase in emulsion based products, tend to only crystallise partially upon cooling from the process to the storage temperature. This makes the final product prone to undergo (re-)crystallisation upon distribution and long-term storage. Uncontrolled crystallisation processes can affect the physicochemical properties of the emulsified fat phase (size and size distribution, composition, polymorphic form and morphology) and thereby impair the functional and sensory characteristics of the product and the overall stability of the emulsion system.

It is the goal of this project to investigate the effect and interplay of different parameters on the storage stability of emulsified triacylglycerols from a product quality perspective and to evaluate different methods to quantify this effect. This study is intended to provide industry relevant recommendations for an optimised formulation and manufacturing process to yield products with a high colloidal stability and quality. A mechanistic understanding of the underlying interfacial or colloidal phenomena is however beyond the scope of this project.

The composition of the model emulsion system, investigated in this report, is designed to resemble that of cow's milk. That is because one important area of application of the knowledge intended to be gained from this study are dairy products. All emulsion ingredients and components are food-grade, so that the results of this project are transferrable to edible products. The samples contain β -lactoglobulin, which is a milk-inherent (naturally sourced), industrially highly available and extensively studied emulsifier. It was chosen due to its beneficial impact on the interfacial properties of O/W-emulsions. It is known to polymerise at emulsion interfaces upon heating, thereby creating a high interfacial viscosity. Its rigid, globular structure adds to this effect and allows β -lg to build thick interfacial layers that provide a good steric stability. The equipment and methods used in this study are known to be available to the food, cosmetics, chemical and pharmaceutical industry. The experiments are carried out at laboratory scale only; it remains to be tested if the results are reproducible at pilot or industrial scale.

Based on the existing scientific evidence discussed in the previous chapter, it has been shown that a higher product quality and a prolonged shelf life of TAG emulsions can be achieved by inducing a guided crystallisation process and by creating a thick and highly viscoelastic interfacial film.

The latter prevents the disperse fat particles from aggregating or coalescing upon collision. The crystallisation conditions have to be specifically designed to prevent or limit polymorphic transitions and to yield small, uniform, spherical and fully crystalline fat particles. Small fat crystals are desired because the interparticle distance is greater, which makes collisions less frequent. The entropy of mixing is lower for fat particles with a monodisperse size distribution and a fully crystalline profile. This limits redistribution and mass transport processes between the individual fat particles. Spherical fat crystals have been shown to be more resistant against recrystallisation. They are also less likely to aggregate and to induce partial coalescence as compared to platelet like crystal morphologies.

The central idea of this project is to test two possible approaches to yield a liquid emulsion system with the above mentioned features as these have been shown to be effective to promote a high shelf life and product quality. These two approaches include the manipulation of a processing and a formulation parameter.

3.2 Hypotheses

The cooling rate and level of supercooling applied to the crystallisation process of emulsified triacylglycerols are known to influence the nucleation and crystallisation behaviour of the TAG molecules and to thereby affect their crystal polymorphism, size and shape. All of these factors have been shown to have an impact on the tendency of emulsion systems to undergo polymorphic transitions and partial coalescence. It was therefore decided to manipulate the cooling rate and to investigate the effect of a fast, moderate and slow cooling process on the colloidal stability of a liquid TAG emulsion.

It is hypothesised that a high cooling rate will improve the storage stability of the model emulsion system. This is motivated by the fact that, at high levels of supercooling, the rate of nucleation exceeds the rate of crystal growth. This is expected to lead to a small and uniform size of the TAG crystals. A quick cooling process also leaves little time for the TAG molecules to restructure and thus to undergo polymorphic transitions. It also makes the TAG molecules crystallise in the loosest packing structure, i.e. the α polymorph. This is beneficial as the α polymorphic form is associated with a spherical crystal morphology.

The second approach, decided to be tested in order to improve the storage stability of the model emulsion system, was to add a low molecular weight emulsifiers (LMWE) to complement the stabilising effect provided by β -lactoglobulin. A phospholipid was chosen as LMWE because phospholipids have been shown to co-adsorb with proteins at oil-water interfaces and to thereby exert a synergistic effect on the viscosity of the interfacial film and the stability of the dispersed fat particles. Phospholipids are comparatively expensive but can be naturally sourced and are well studied. As compared to proteins, they are much smaller in size which accounts for their higher interfacial packing density and higher

mobility. This in turn allows them to adsorb faster to newly created emulsion interfaces and to reduce the surface tension more efficiently. Phospholipids have also been shown to act as crystallisation templates, triggering a surface heterogeneous nucleation process in dispersed TAG particles and to thereby reduce the level of supercooling required to fully crystallise the fat phase. A prerequisite for this phenomenon to occur is a structural similarity between the phospholipid and the fat phase in terms of the degree of unsaturation and chain length of their FAs. As the model emulsion system is based on a hydrogenated palm oil, which consists predominantly of palmitic and stearic fatty acids, a phospholipid with C18:0 chains was chosen as additional emulsifier.

It is hypothesised that the addition of a phospholipid with a similar molecular structure to the fat phase will have a positive impact on the overall stability of the model emulsion system.

Apart from the nature of the FA tails, the effect of the headgroup of the phospholipid was also considered in this study. As a phospholipid with a highly polar headgroup is expected to have a higher affinity for the emulsion interface, when administered together with the fat phase, **it is hypothesised that a phospholipid with a higher HLB value will adsorb faster and provide better stability to the emulsified TAG particles.** Therefore, DSPC and DSPE, being structurally identical apart from the polarity of their headgroup, were both tested in this study. DSPC is hypothesised to lead to a better colloidal stability not only because of its higher HLB value but also because it has a higher melting point and has been shown to build more compact interfacial films as compared to DSPE.

4 Materials and Methods

4.1 Materials and Tools

Table 4-1 Ingredients for emulsion preparation.

Softisan® 154 hydrogenated palm oil	IOI Oleo GmbH, Wittenberge, Germany
Beta lactoglobulin	courtesy of Technical University Munich, Germany
LIPOID PC 18:0/18:0	Lipoid GmbH, Ludwigshafen, Germany
1,2-distearoyl-sn-glycero-3-phosphocholine (DSPC)	Lipoid GmbH, Ludwigshafen, Germany
LIPOID PE 18:0/18:0	Lipoid GmbH, Ludwigshafen, Germany
1,2-distearoyl-sn-glycero-3-ethanolamine (DSPE)	Lipoid GmbH, Ludwigshafen, Germany
Potassium sorbate C ₆ H ₇ KO ₂	VWR International bvba, Leuven, Belgium

Table 4-2 Chemicals needed for DSC measurements and pH adjustment.

Nitrogen	AIR LIQUIDE GmbH, Düsseldorf, Germany
1 M Sodium hydroxide NaOH	Carl Roth GmbH + Co. KG, Karlsruhe, Germany

Table 4-3 Analytical devices and homogenisers.

IKA® T25 digital ULTRA-TURRAX® tooth-rim dispersing machine	IKA-Werke GmbH & Co. KG, Staufen im Breisgau, Germany
IKA® magic LAB® single stage dispersing machine	IKA-Werke GmbH & Co. KG, Staufen im Breisgau, Germany
Corning® PC-420D HS 7 stirring hot plate	Corning Inc., New York, USA
MC1 LC 4800 P precision scale	Sartorius AG, Goettingen, Germany
edge® multiparameter pH meter	Hanna Instruments Deutschland GmbH, Voehringen, Germany
HORIBA LA-950V2 laser diffraction particle size analyser	HORIBA Ltd., Minami-Ku Kyoto, Japan
DSC 8500 differential scanning calorimeter	Perkin Elmer Inc., Waltham, USA
Nikon Eclipse LV100ND polarised light microscope	Nikon, Shinagawa, Tokyo, Japan
Empyrean X-ray diffractometer	Malvern Panalytical, Worcestershire, UK
Thermo Scientific™ Barnstead™ MicroPure™ water purification system	Thermo Fisher Scientific Inc., Waltham, USA

Table 4-4 Software.

Microsoft Excel 2019	Microsoft Corp., Redmond, USA
GraphPad Prism version 9	GraphPad Inc., San Diego, USA
DIFFRAC.EVA version 4.1.1	Bruker Crop., Billerica, USA

4.2 Emulsion Preparation

The samples are prepared by a melt emulsification process as discussed in chapter 2.1.2. First, a coarse premix is produced, which is then processed into a finely dispersed emulsion. In order to prevent premature crystallisation, the whole process is carried out at a temperature of + 10 K above the melting point of the fat phase. A ratio of the different emulsion components that has proven to yield a stable system has been established by Heiden-Hecht et al. (2021) and is accepted to 1 : 0.1 : 0.01 disperse fat phase to protein to phospholipid.

4.2.1 Coarse Emulsion Preparation

A 0.53 wt% protein solution is prepared from β -lactoglobulin (TU Munich, Munich, Germany) and purified, neutralised water by mixing and stirring at room temperature for 2 h. The pH is raised above the protein's isoelectric point to 6.5 with 1 M NaOH (Carl Roth GmbH + Co. KG, Karlsruhe, Germany). The protein solution is stored cold overnight to allow full protein hydration.

For the preparation of the reference samples, a 5 % mass fraction of Softisan[®] 154 (IOI Oleo GmbH, Wittenberge, Germany) is molten in an 85 °C water bath for 20 min to erase crystal memory. Softisan[®] 154 is a hydrogenated palm oil. According to the manufacturer's specifications it has a melting range of 53-58 °C and consists of mixed TAGs esterified with over 95 % 16:0/18:0 FAs and a rest of 12:0/14:0 FAs. All samples other than the reference samples, are prepared from 5 wt% Softisan[®] 154 and an additional 0.05 or 0.1 wt% of either one of the two phospholipids featured in Table 4-5. The phospholipid and fat fraction are mixed, and heat treated as described for the fat phase alone. The temperature of the protein solution is raised to match the temperature of the fat phase by heating for 5 min in an 85 °C water bath. The protein solution is then added to the fat phase or fat-phospholipid-mixture respectively, yielding a final sample composition as proposed by Heiden-Hecht et al. (2021) (see Table 4-6). A coarse emulsion is prepared using an IKA[®] T25 digital ULTRA TURRAX tooth-rim dispersing machine (IKA-Werke GmbH & Co. KG, Staufen im Breisgau, Germany). The pre-emulsification is performed in an 85 °C water bath at a tangential speed of 2.5 m s⁻¹ (3,200 rpm, outer diameter of the dispersing tool = 13 mm) for 2 min.

Table 4-5 Composition of commercially available lecithins according to manufacturer's specification (Lipoid GmbH, Ludwigshafen, Germany). n. sp. = not specified.

Components [%]	LIPOID PC 18:0/18:0	LIPOID PE 18:0/18:0
Phosphatidylcholine	≥ 99.0	n. sp.
Phosphatidylethanolamine	n. sp.	≥ 98.0
Lysophospholipids	≤ 0.5	≤ 0.5
Triacylglycerols	≤ 0.3	≤ 0.3
C16:0	n. sp.	n. sp.
C18:0	≥ 98.0	min. 98.0
Source	Synthetic	Synthetic

4.2.2 Fine Emulsion Preparation

The coarse premix is finely dispersed with an IKA® magic LAB® colloid mill (IKA-Werke GmbH & Co. KG, Staufen im Breisgau, Germany) for 10 min. The average circumferential speed is set to 36.7 m s^{-1} (25,000 rpm respectively, upper radius of the rotor = 11.5 mm, lower radius of the rotor = 16.5 mm, radial gap = 0.159 mm). The device is preheated with boiling water and subsequently cooled with cold water to keep the process temperature constant at 65 °C. Each sample volume is equally split over three glass vials. One vial is allowed to cool at room temperature (RT), the other two are transferred to a 5 °C refrigerator (RF) and a 0 °C ice bath (IB) respectively until they reach a final temperature of 22 °C. These cooling conditions are to mimic a low (RT), moderate (RF) and high (IB) cooling rate (Reiner et al., 2022). Every sample is produced in two copies (two ‘sample replicates’). The composition of the samples and the applied rate of cooling are summarised in Table 4-6.

Table 4-6 Composition and process parameters of prepared emulsions.

Sample name	Cooling rate	Softisan® 154	β -lg	LIPOID PC 18:0/18:0	LIPOID PE 18:0/18:0
B-RT	Low	5 wt%	0.5 wt%		
B-RF	Moderate				
B-IB	High				
C-RT	Low	5 wt%	0.5 wt%	0.05 wt%	
C-RF	Moderate				
C-IB	High				
CC-RT	Low	5 wt%	0.5 wt%	0.1 wt%	
CC-RF	Moderate				
CC-IB	High				
E-RT	Low	5 wt%	0.5 wt%		0.05 wt%
E-RF	Moderate				
E-IB	High				
EE-RT	Low	5 wt%	0.5 wt%		0.1 wt%
EE-RF	Moderate				
EE-IB	High				

4.2.3 Storage Conditions

All samples are stored in the dark at a constant temperature of 22 °C and in an upright, resting position. Whenever a sample aliquot is needed for analysis, the sample container is gently inverted three times to allow a homogenous sampling process while avoiding excessive mechanical energy input. In order to prevent spoilage during storage, 0.2 wt% potassium sorbate (VWR International bvbr, Leuven, Belgium) is added to all samples. The pH is checked regularly and corrected to 6.5 with 1 M sodium hydroxide (Carl Roth GmbH + Co. KG, Karlsruhe, Germany).

4.3 Analytical Methods

Sample analysis is carried out over a total period of two months. If not stated otherwise, the analytical measurements are performed on all samples (and sample replicates) and repeated at the following intervals: t_0 = directly after sample preparation, t_2 = after two weeks, t_4 = after four weeks, t_8 = after eight weeks.

4.3.1 Laser Diffraction Analysis

The size of a spherical particle can be described with just one characteristic dimension: its diameter. Particles with a morphology deviating from that of a perfect sphere can be characterised by multiple descriptors such as different length and width measures. The concept of the equivalent sphere diameter is based on the assumption that the size of a non-spherical particle can be adequately approximated by that of a sphere. Thus the equivalent volume diameter would be the diameter of a sphere having the same volume as the actual particle. This assumption is valid for most colloidal particles apart from morphologies such as fibres or needles where one descriptor strongly dominates over the others (Merkus, 2009, p. 908).

The particle size distribution of the samples is determined by laser diffraction analysis with a HORIBA LA-950V2 particle size analyser (HORIBA Ltd., Minami-Ku Kyoto, Japan). The measurement principle is based on light scattering analysis according to Mie theory and Fraunhofer diffraction theory. A laser diode and an LED, emitting light of 650 nm and 405 nm wavelength respectively, irradiate the sample leading to angle-dependent (particle size is $> \lambda/10$) interaction phenomena such as diffraction, refraction, absorption and reflection (Bhattacharjee, 2016). This creates a particle-specific light scattering pattern, which can be related back to the particle's size. A stirred fraction cell is filled with purified water and a blank measurement is performed to calibrate the system. The samples are pre-dilute at a 1:6 ratio before being added to the fraction cell. All measurements are performed in ambient purified water. The refractive index of Softisan® 154 is accepted to $1.460 - 0.001i$.

The resulting equivalent particle size distribution is stated as a cumulative normalised undersize distribution Q [%] based on the particle volume (Q_3) or count (Q_0). The width of the distribution is commonly described by the x_{10} , x_{50} and x_{90} percentiles. In the case of a volume based undersize distribution the $x_{10,3}$; $x_{50,3}$ and $x_{90,3}$ define the diameter of the particles that make up the lower 10 %, 50 % and 90 % of the total volume of all particles. The span is calculated from these three percentiles as per (Merkus, 2009, p.26):

$$span = \frac{x_{90,3} - x_{10,3}}{x_{50,3}} \quad \text{Equation 4-1}$$

The average equivalent particle size can be expressed by the median ($x_{50,3}$) or mode (peak diameter) of the distribution or in terms of different weighted means, which are defined as (Merkus, 2009, p.24):

$$d_{1,0} = \frac{\sum n_i d_i}{\sum n_i} \wedge d_{3,2} = \frac{\sum n_i d_i^3}{\sum n_i d_i^2} \wedge d_{4,3} = \frac{\sum n_i d_i^4}{\sum n_i d_i^3} \quad \text{Equation 4-2}$$

where $d_{1,0}$ = number weighted mean diameter or arithmetic mean, $d_{3,2}$ = surface area weighted mean diameter or Sauter mean, $d_{4,3}$ = volume weighted mean diameter or DeBroukere mean, n_i = frequency of occurrence of particles in size class i , d_i = mean particle diameter in size class i .

4.3.2 Polarised Light Microscopy

The microstructure of the samples is assessed at room temperature using a polarised light microscope Nikon Eclipse LV100ND (Nikon, Shinagawa, Tokyo, Japan) with 20x objective magnification. Polarised light allows to distinguish between isotropic and anisotropic materials. Anisotropy describes “the optical properties of an object or propagation medium, having dissimilar properties in different directions, such as variations in refractive index along different directions of propagation of light [...]” (Murphy and Davidson, 2013, p.467). Crystals are highly ordered structures with directional orientation, thus, light travels differently through crystalline materials depending upon the direction of propagation. Polarised light interacts with polarisable bonds of ordered molecules in a direction-dependent way (Murphy and Davidson, 2013). This principle allows to visualise anisotropic materials as bright coloured structures as opposed to isotropic materials, which appear non-coloured. In emulsions with a (semi-) crystalline disperse phase, polarised light makes liquids, i.e. isotropic materials, distinguishable from crystal solids, i.e. anisotropic materials. This allows to assess the degree of crystallinity or solid fat content (SFC) of the emulsion and to characterise the size and shape of crystallised colloidal particles. Polarised light microscopy also allows to track changes of the emulsion microstructure that result from instability phenomena. Flocculation leads to particle/droplet aggregation, whereas coalescence and Ostwald ripening result in a growing particle/droplet size. Both native and diluted (1:10) samples are assessed to study interaction phenomena as well as to characterise individual colloidal particles. 10 μ l of the sample are pipetted onto an object slide and covered with an 18 mm x 18 mm cover slip, resulting in a sample thickness of close to 30 μ m.

4.3.3 Visual Analysis

As proposed by Zhang et al. (2020) the colloidal stability of an emulsion can be assessed visually by photographing the sample in a transparent storage container against a black background. Measuring the height of the top creamed layer and the total emulsion allows to calculate the creaming index (CI):

$$CI(\%) = 100 \times \frac{H_C}{H_T} \quad \text{Equation 4-3}$$

where H_T = total emulsion height and H_C = top creamed layer height in millimetres respectively.

4.3.4 Differential Scanning Calorimetry

The samples are analysed with a double-furnace differential scanning calorimeter DSC 8500 (Perkin Elmer Inc., Waltham, USA) to determine the melting behaviour of the emulsified fat phase,

as well as the polymorphic characteristics and the purity of the TAG crystals.

Differential scanning calorimetry (DSC) is the “most commonly used thermal technique for studying the amorphous and crystalline nature of foods” (Bund and Hartel, 2010, p.201). Differential scanning calorimeters measure the change in specific heat capacity of a sample material as a function of temperature. The specific heat capacity c_p of a material is defined as “the quantity of heat that is gained or lost by a unit mass of [a material] to accomplish a unit change in temperature, without a change in state” (Singh and Heldman, 2014, p.275) and has the unit [$\text{kJ kg}^{-1} \text{K}^{-1}$]. The change in the material’s specific heat capacity is tracked as change in the heat flow [W g^{-1}] as the sample is subjected to a temperature programme (Perkin Elmer Inc., 2013). By convention, when using a double-furnace heat flow DSC, endothermic events ($+\Delta H$), i.e. “thermal event[s] [...] where energy is absorbed by the material, e.g. melting” (Perkin Elmer Inc., 2013, p.8) are reported as peaks pointing upwards. Exothermic events ($-\Delta H$), i.e. “thermal event[s] [...] where energy is expelled by the material, e.g. crystallisation” (Perkin Elmer Inc., 2013, p.8) are reported as peaks pointing downwards.

DSC measurements provide extensive information about the melting behaviour of a material including the onset temperature of melting, the melting point T_m and the energy needed for the melting transition ΔH_m . The melting point, i.e. the temperature at which the material is fully melted, is given as the peak temperature of the melting event. The melting endotherm corresponds to the area under the peak of the melting event. ΔH_m is an indicator of the quantity of crystalline material or SFC of the sample. (Rabelo et al., 2018) As TAGs crystallise in three different polymorphs with increasing melting point from the α to the β form, polymorphic characteristics can be distinguished. Likewise, mixed TAG and pure monoacid TAG crystals can be distinguished with α polymorphs being most likely to give rise to mixed crystals as they have a loose structure that allows for the incorporation of impurities and/or TAGs with compositional variety. It has been observed that bulk fats generally show several exothermic peaks corresponding to the low, middle and high melting fat fraction which each consists of TAGs with similar chain length and saturation level. Emulsified fats however tend to show only one single exothermic event, corresponding to mixed crystals that form in the α polymorph. (Bayard et al., 2022) The calorimeter is calibrated against indium ($T_m = 156.6 \text{ }^\circ\text{C}$), water ($T_m = 0.000 \text{ }^\circ\text{C}$) and n-decane ($T_m = -29.65 \text{ }^\circ\text{C}$) at scanning rates of $\pm 2.5 \text{ }^\circ\text{C}/\text{min}$. 9-11 mg of the samples are loaded into aluminium pans (50 μl , 10 x 2.1 mm, Perkin Elmer Inc., Waltham, USA) and are hermetically sealed. An empty pan serves as reference. The samples and reference are cooled to 20 $^\circ\text{C}$ and the temperature is hold for 2.5 min. The pans are then heated to 70 $^\circ\text{C}$ at a constant scanning rate of $2.5 \text{ }^\circ\text{C min}^{-1}$. After 5 min holding time, the pans are cooled back to 22 $^\circ\text{C}$ at $20 \text{ }^\circ\text{C min}^{-1}$ scanning rate. The melting temperature is determined at t_0 and t_8 over the duration of the sample storage. Both sample replicates are tested but only one technical replicate is performed.

4.3.5 X-Ray Diffraction

There are different parallel planes of atoms dissecting the unit cell of a crystal. The vector coordinates (hkl) of these planes are known as Miller indices. (Speakman, n.d.) They allow to clearly identify and characterise a set of parallel planes as shown in Figure 4-1.

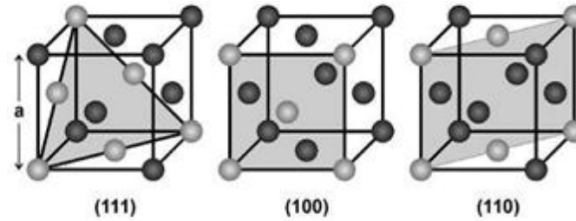


Figure 4-1 Schematic representation of a crystal unit cell with its parallel planes of atoms. The vector coordinates below are the Miller indices defining the orientation of the planes (adopted from Lebouin et al., 2009).

Every crystal system has a specific set of parallel planes with a set distance between them. This allows for instance to distinguish between the α , β' and β polymorphs of a TAG crystal as the three polymorphic forms are built from different unit cells and thereby also have individual sets of parallel planes.

X-rays are a type of electromagnetic radiation with a wavelength of 10 pm to 10 nm. Within this range of the electromagnetic spectrum, interaction with atoms can occur. An X-ray diffractometer emits X-rays of a constant wavelength λ that meet the sample surface at an incident angle ω and detect scattered X-rays at a diffraction angle 2θ . The diffraction vector s bisects the angle between the incident and diffracted beam and is normal to the sample surface. (Speakman, n.d.) A schematic representation of an X-ray diffractometer is given in Figure 4-2.

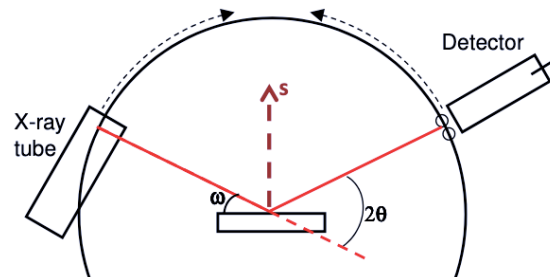


Figure 4-2 Schematic representation of an X-ray diffractometer with a Bragg-Brentano geometry, where the incident and diffracted beam slits move on a circle around the sample. The incident angle ω is half of the diffraction angle 2θ and the diffraction vector s bisects the angle between the incident and diffracted beam (adopted from Speakman, n.d.).

Because of the periodic array of the atoms in a crystal, irradiation of a crystalline material with X-rays creates a specific diffraction pattern. Every crystal structure has a unique diffraction pattern that is related to the shape of its component unit cells and thus to the orientation of its parallel planes. A peak in the diffraction pattern results from constructive interference between the emitted X-rays and a statistically significant number of properly oriented crystals within the sample material. Constructive interference occurs only with crystals which are oriented in a way that one set of parallel planes scatters the incident X-ray beam such as that the plane normal [hkl] is parallel to the diffraction vector s . (Speakman, n.d.) This is illustrated by Figure 4-3.

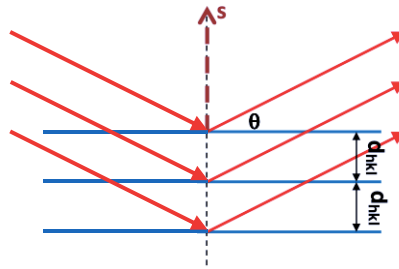


Figure 4-3 Schematic representation of a properly oriented crystal that creates a diffraction peak in an XRD measurement. The orientation of the parallel planes in the crystal structure diffracts the incident X-rays in a way to cause constructive interference. The diffraction vector s bisects the incident and the diffracted angle. d_{hkl} denotes the distance or d-spacing between the parallel planes with the Miller indices (hkl) (adopted and modified from Speakman, n.d.).

Based on the diffraction pattern of a crystalline sample and the wavelength λ of the incident X-rays, Bragg's law allows to translate the peak position, i.e. the detection angles at which diffraction peaks are recorded, into the distance or d-spacing d_{hkl} between the set of parallel planes that the peaks originate from (Romo-Urbe, 2022):

$$n\lambda = 2d_{hkl} \sin \theta \quad \text{Equation 4-4}$$

with $n =$ diffraction order = 1, $\theta =$ half of the detection angle at which constructive interference occurs, $\lambda =$ wavelength of the incident beam, $d_{hkl} =$ distance between the set of parallel planes with the vector coordinates (hkl) .

The peak intensity is a function of the location and nature of the atoms constituting the parallel plane where constructive interference occurs. In order to identify the crystalline sample, the recorded diffraction pattern can be matched with the reference patterns stored in databases such as the powder diffraction file (PDF) (Speakman, n.d.). The diffraction pattern of mixed polymorphic TAG crystals with the characteristic d-spacing of the β' and β crystal polymorphs is shown in Figure 4-4.

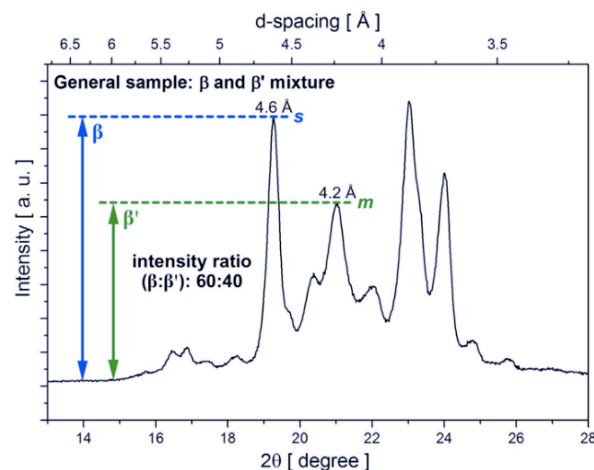


Figure 4-4 Exemplary diffraction pattern of a TAG with β' and β polymorphic crystals. The labels 's' and 'm' indicate a strong and medium peak intensity (adopted from Calligarisa et al., 2018).

There is however only very little crystallographic data available on the α polymorphic form, which is due to its instability and its tendency to rapid polymorphic transition (Golodnizky et al., 2022). Table 4-7 shows the characteristic diffraction peaks for all three polymorphs of milk fat.

Table 4-7 Characteristic diffraction peak positions of the three main polymorphic forms found in milk fat as measured by small and wide angle X-ray diffraction (adopted from Mazzanti et al., 2004, p.1304).

polymorph	q, Å ⁻¹ (<i>d</i> spacing, Å)	
	small angle reflections	wide angle reflections
α	0.137 (47.2)	1.514 (4.15)
β'	0.151 (41.6)	1.654 (3.80)
		1.472 (4.27)
β	0.166 (38.0)	1.366 (4.60)

The XRD measurements are performed by the technical team at the Institute of Applied Materials and Electrochemical Technologies at the Karlsruhe Institute of Technology using an Empyrean X-ray diffractometer with a Bragg-Brentano geometry (Malvern Panalytical, Worcestershire, UK). The X-ray source is a copper tube ($\lambda = 0.154060$ nm) operating at 40 kV and 40 mA. The diffraction patterns are determined at t_0 and t_8 for the B, C and E samples cooled at low and high cooling rate respectively. The other samples and sample replicates were not analysed because of resource restrictions. One sample droplet is pipetted onto the sample holder and the diffraction pattern is acquired by scanning 2θ diffraction angles from 10.0001° to 90.0011° in intervals of 0.01023° . The data are postprocessed with DIFFRAC.EVA version 4.1.1 (Bruker Crop., Billerica, USA).

4.3.6 Statistical Analysis

All measurements are performed on two sample replicates ($N = 2$) with one or three technical replicates ($n = 3$ or $n = 1$) each. The statistical analysis is performed using Microsoft Excel 2019 (Microsoft Corp., Redmond, USA) and GraphPad Prism 9 (GraphPad Inc., San Diego, USA). All data points are given as average with their respective standard error of the mean (SEM). The data are checked for normal distribution using Shapiro-Wilk and Kolmogorov-Smirnov test. Normally distributed data are analysed using one-way analysis of variance (ANOVA) with a significance level of $p^* < 0.05$. For non-normally distributed data, Kruskal-Wallis tests or Mann-Whitney tests are performed.

5 Results and Discussion

5.1 Results on the Macrostructure

The macrostructure of the samples was assessed by photographing the sample containers in front of a black background. In Figure 5-1, Figure 5-2 and Figure 5-3, pictures of the samples at the beginning (t_0) and at the end of the storage period (t_8) are compared. The remaining images taken at t_2 and t_4 , are shown in Figure 8-1 to Figure 8-5 in the appendix.

The total sample volume decreased over time as sample aliquots were taken to perform the different analytical measurements. The surface of some samples appeared foamy because the homogenisation process in the colloidal mill lead to a more or less substantial foam formation.

All samples, irrespective of the formulation, cooling rate or storage time, appeared heterogenous. An intensely white and opaque top layer was clearly visually separated from a main phase that split up again into a thin, clear layer at the very bottom of the sample container and a remaining large phase. From the images shown below, this split up or gradient within the main phase is most clearly visible in the E and EE samples in Figure 5-3. All samples could be easily turned visually homogenous again once the sample containers were gently shaken. The top layer on the B samples however grew increasingly rigid over time. Thus, the B samples stayed heterogenous when mixed. It was not possible to quantify this observation as a separation of the top layer and a subsequent rheological analysis would have destroyed the sample.

The creaming index (CI) of the samples were determined by measuring the height of the top layer and by applying Equation 4-3. The results are summarised in Figure 8-6 and Figure 8-7 in the appendix. The samples stabilised by β -lg alone showed a constant increase of the CI from 3-5 % to 7-10 % over eight weeks of storage. The absolute height of the top layer stayed however more or less constant at around 5 mm on average, irrespective of the cooling rate (see Figure 5-1).

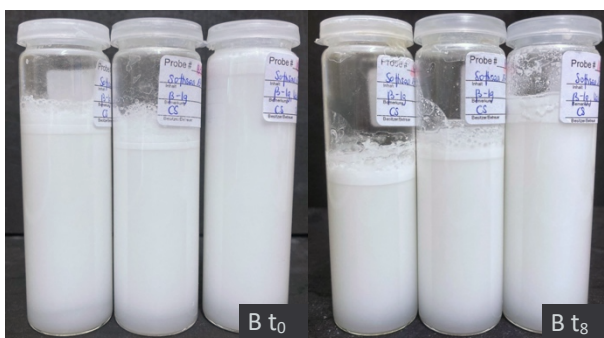


Figure 5-1 Images of B samples cooled at slow (left), moderate (middle) and fast (right) rate, taken at t_0 and t_8 .

The phospholipid containing samples showed an opposite tendency, i.e. a decrease of the CI from an initial 10-15 % to 5-7 %, which was slow in the beginning of the storage period and sharp between t_4 and t_8 . The absolute height of the top layer dropped after four weeks of storage from an initial constant value of about 10 mm to 5-7 mm. The top layer was always liquid and easily miscible.

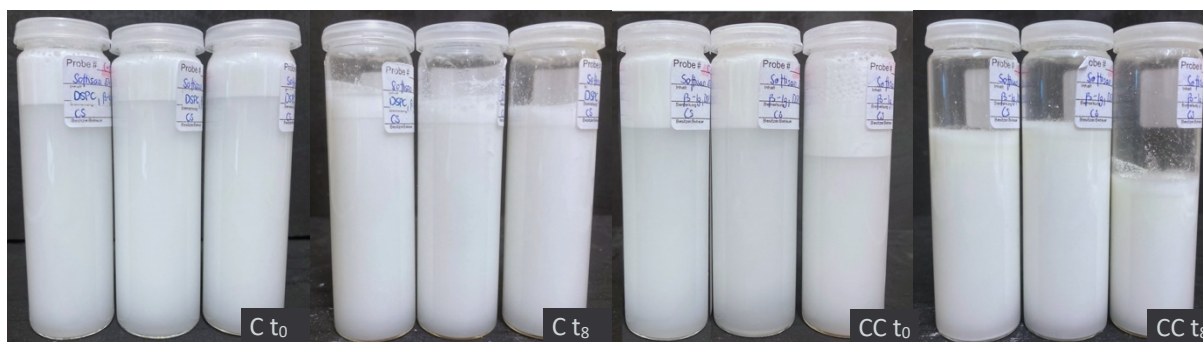


Figure 5-2 Images of C and CC samples cooled at slow (left), moderate (middle) and fast (right) rate, taken at t_0 and t_8 .

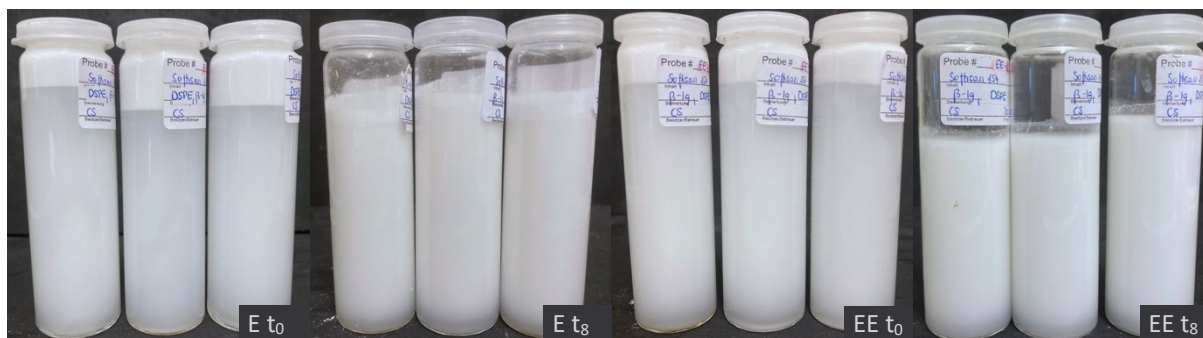


Figure 5-3 Images of E and EE samples cooled at slow (left), moderate (middle) and fast (right) rate, taken at t_0 and t_8 .

All samples, irrespective of the formulation or cooling rate, were comparable in terms of the thickness of the top layer after eight weeks of storage. Kruskal-Wallis tests performed on the creaming indices showed no statistically significant effects (see Figure 8-6 and Figure 8-7 in the appendix).

When examining the main phase of the samples, a difference in the level of turbidity between the B samples and the phospholipid containing samples, that is independent of the cooling rate and the phospholipid concentration, can be noted. While the main phase of the B samples showed a constant intense opacity, the main phase of the C, CC, E and EE samples was clear at t_0 and turned turbid after eight weeks of storage (see also Figure 8-2 to Figure 8-5 in the appendix). Photometric measurements could have allowed to quantify this effect if it had been anticipated.

5.2 Results of the Equivalent Particle Size Distribution and Microstructure

5.2.1 Results on the Microstructure

At 20x magnification in the polarised light microscope, the emulsion particles of the B samples appeared spherical and brightly coloured (see Figure 5-4). The emulsion particles showed a polydisperse size distribution: While the majority of the particles had a diameter of about 3 μm , there were many big particles with a size of up to 20 μm . The samples crystallised at high cooling rate (IB) appeared overall slightly more monodisperse as compared to those crystallised at low (RT) or moderate (RF) cooling rate. Over time, the polydispersity seemed to decrease in all samples irrespective of the cooling rate. The size of the biggest emulsion particles was lowered to about 15 μm . Particle flocs occurred in all samples but were overall small and did not involve many emulsion particles (see white arrows).

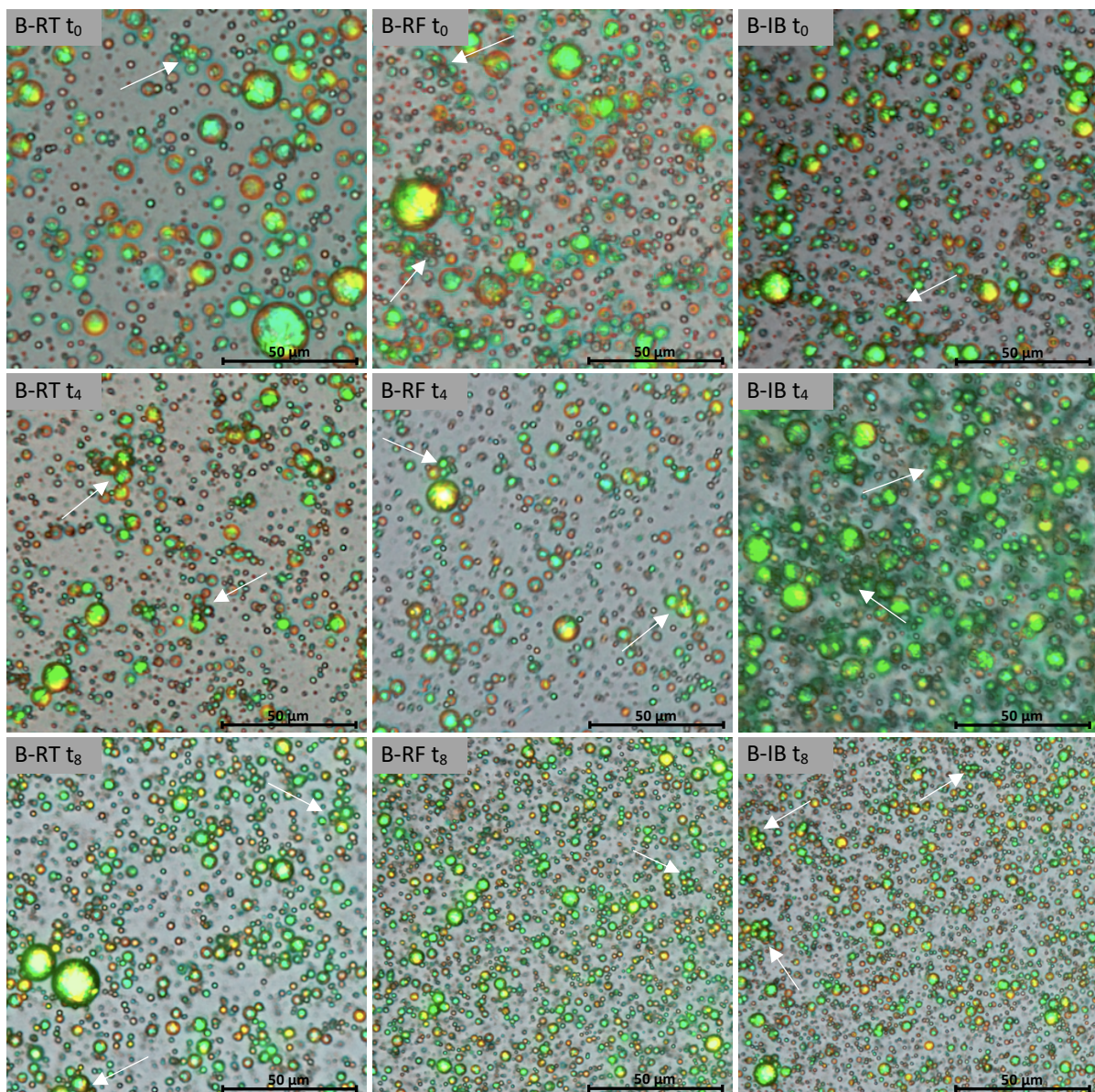


Figure 5-4 Microscopic images of undiluted B samples cooled at slow (left), moderate (middle) and fast cooling rate (right) taken at t_0 (top), t_4 (middle) and t_8 (bottom). 20x magnification. Arrows point to emulsion particle flocs.

The emulsion particles of the DSPC containing samples appeared spherical and brightly coloured (see Figure 5-5 and Figure 5-6). The maximum particle size and the diameter of the majority of the emulsion particles were a bit lower as compared to the B samples. The biggest particles reached a size of about 15 μm in the C samples and 10 μm in the CC samples. Thus, the DSPC containing samples seemed overall more monodisperse as compared to the B samples and increasingly monodisperse with an increasing DSPC concentration. Flocculation however was slightly more pronounced, especially for the samples crystallised at low (RT) and moderate (RF) cooling rate.

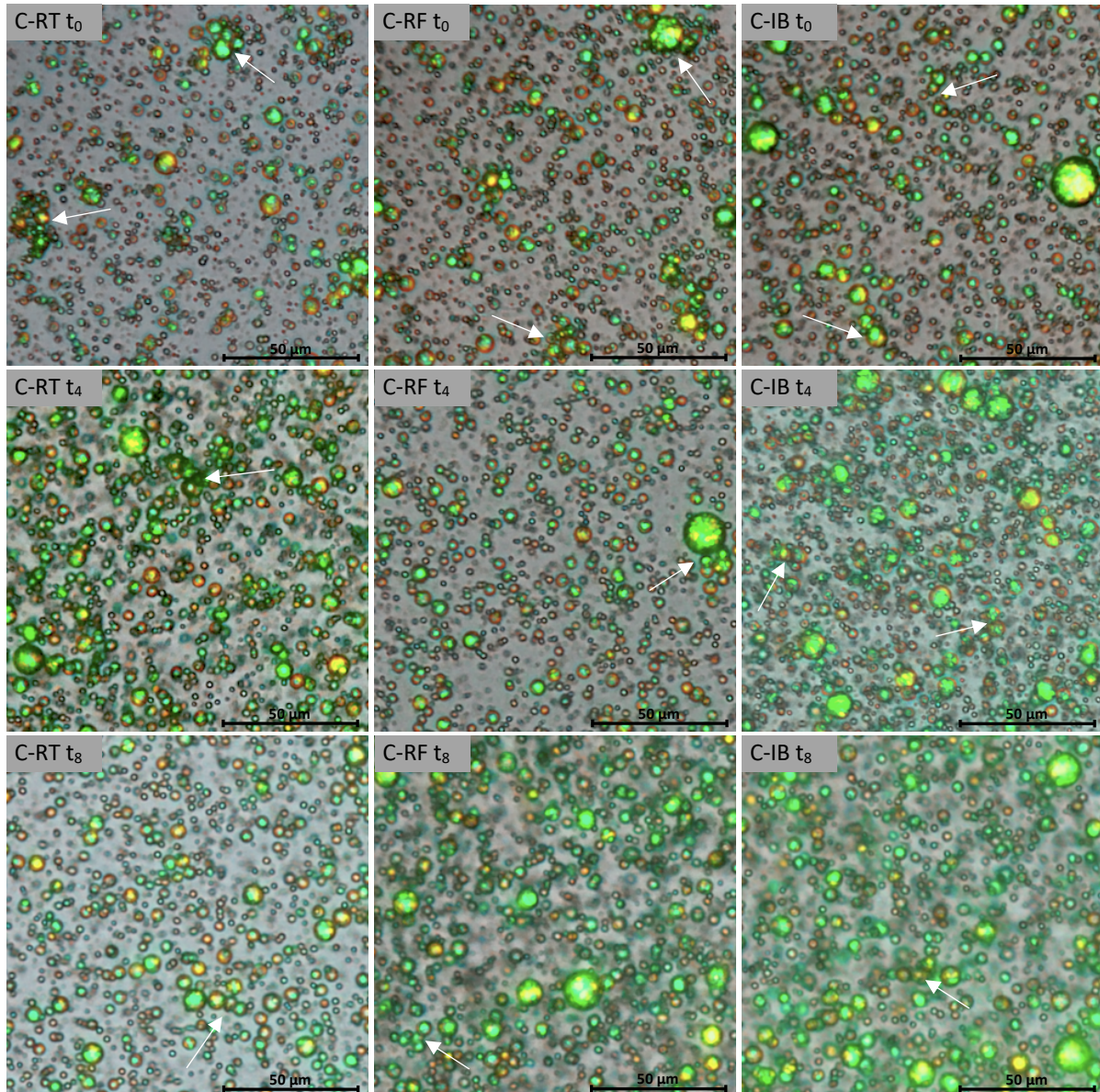


Figure 5-5 Microscopic images of undiluted C samples cooled at slow (left), moderate (middle) and fast cooling rate (right) taken at t_0 (top), t_4 (middle) and t_8 (bottom). 20x magnification. Arrows point to emulsion particle flocs.

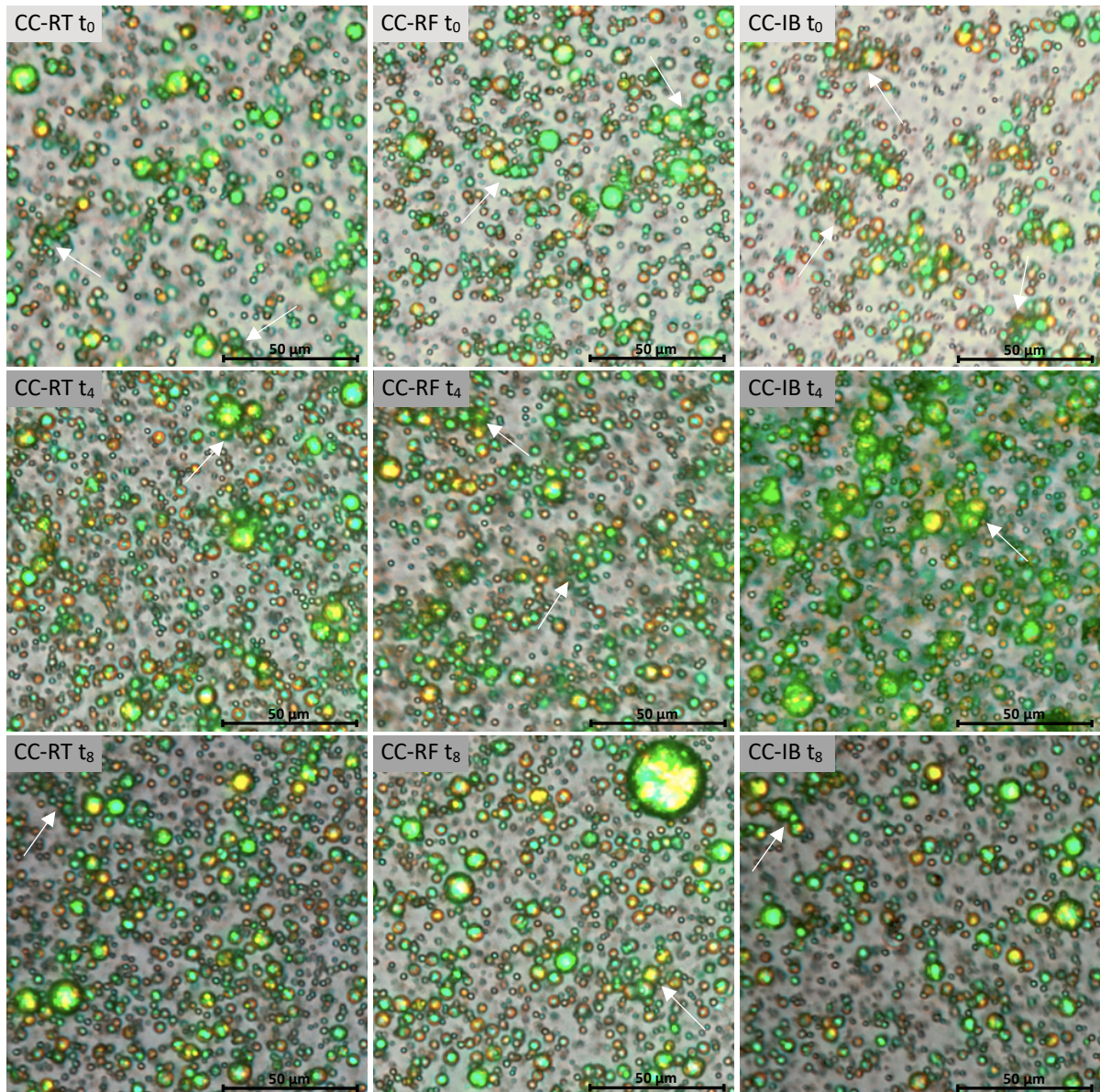


Figure 5-6 Microscopic images of undiluted CC samples cooled at slow (left), moderate (middle) and fast cooling rate (right) taken at t_0 (top), t_4 (middle) and t_8 (bottom). 20x magnification. Arrows point to emulsion particle flocs.

Just as for the samples stabilised with DSPC or with β -lg alone, the emulsion particles in the DSPE containing samples appeared spherical and brightly coloured (see Figure 5-7 and Figure 5-8). The majority of the particles had a small size of 2 μm or less and the biggest particles had a maximum diameter of around 8 μm in the E samples and 6 μm in the EE samples. The DSPE containing samples therefore showed the most monodisperse particle size distribution of all samples but also the highest amount of flocculated particles. The flocs involve more particles as compared to the B, C or CC samples and therefore reached a similar size even though the individual particles, that formed the flocs, were smaller. Over the storage time, the size distribution seemed to narrow down slightly in all samples (E and EE) irrespective of the cooling rate as the amount of big droplets appeared to decrease.

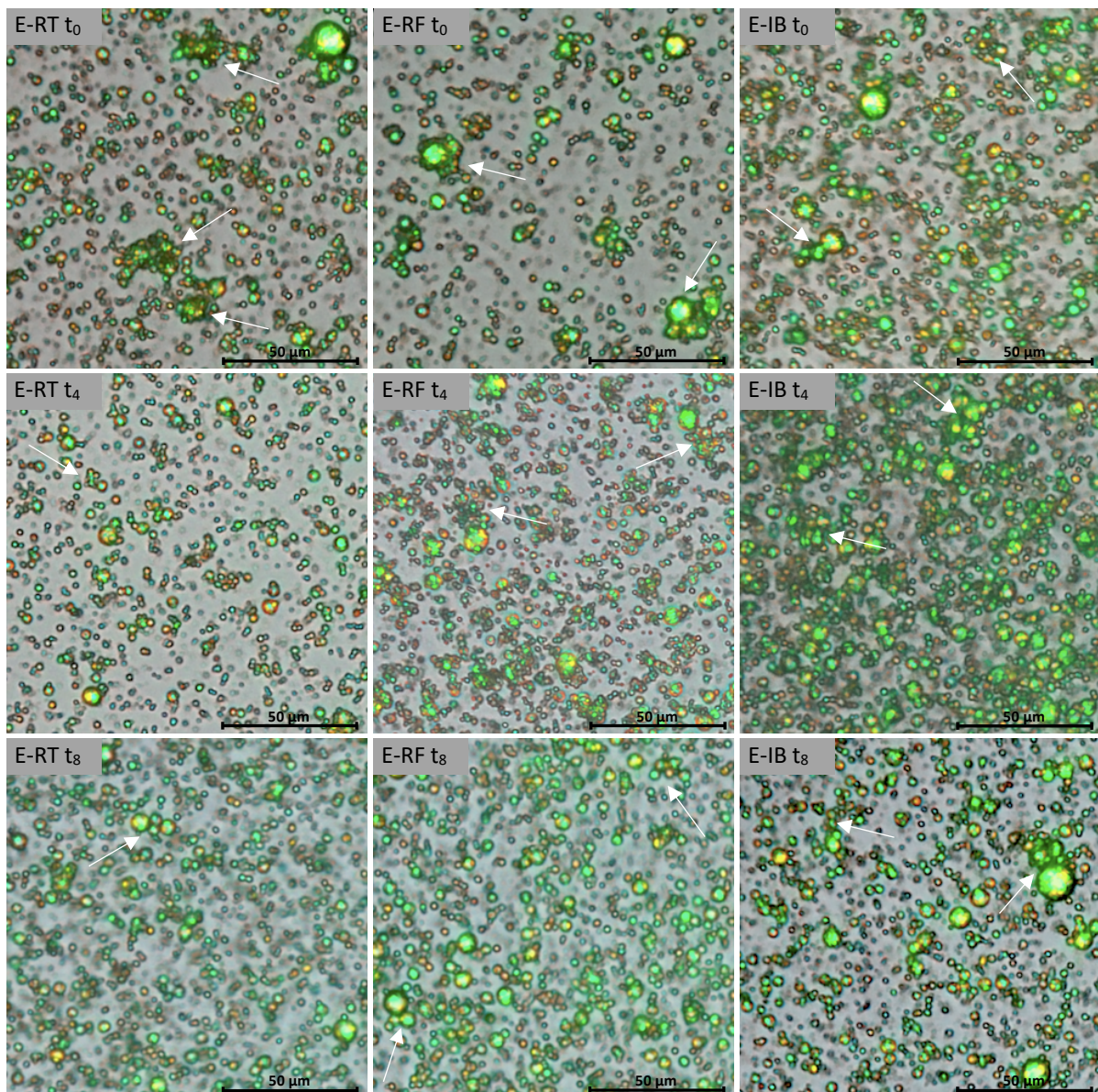


Figure 5-7 Microscopic images of undiluted E samples cooled at slow (left), moderate (middle) and fast cooling rate (right) taken at t_0 (top), t_4 (middle) and t_8 (bottom). 20x magnification. Arrows point to emulsion particle flocs.

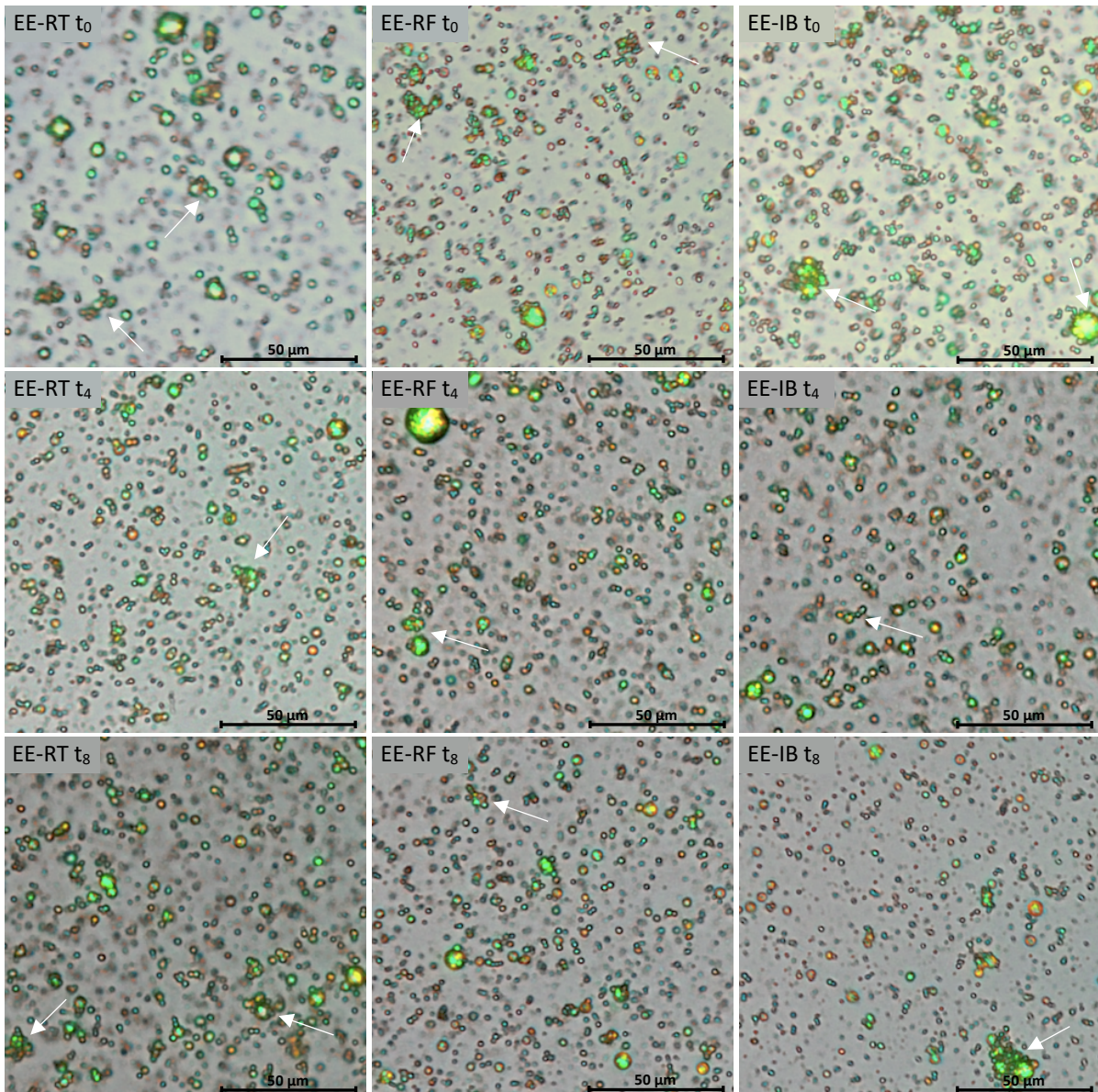


Figure 5-8 Microscopic images of undiluted EE samples cooled at slow (left), moderate (middle) and fast cooling rate (right) taken at t_0 (top), t_4 (middle) and t_8 (bottom). 20x magnification. Arrows point to emulsion particle flocs.

In Figure 5-9 general observations made on all samples are illustrated based on some examples. The emulsion particles marked by the red frame in the pictures on the middle-left and left deviate from the spherical morphology. The structures seem to consist of two merging particles that lost their individual boundaries. The red frames on the images on the centre-right and right highlight emulsion particles with a particular appearance known as the Maltese cross. The red circle indicates two emulsion particles that remained uncoloured.

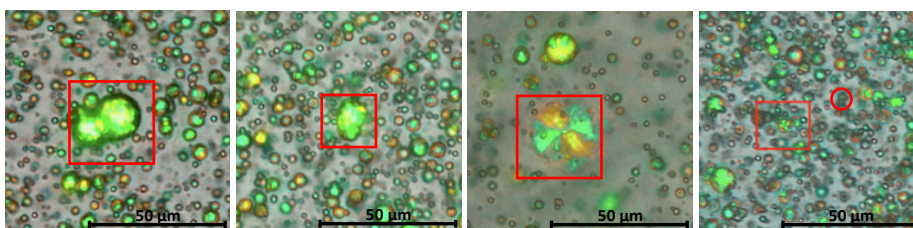


Figure 5-9 Partially (left) and totally merged (centre-left) emulsion particles and Maltese crosses (centre-right and right) found in different samples and after different storage periods. 20x magnification.

5.2.2 Results of the Equivalent Particle Size Distribution

The size of the emulsion particles was assessed via laser diffraction analysis and visualised as a cumulative normalised undersize distribution (Q3) in Figure 8-8 to Figure 8-12 in the appendix.

In Figure 5-10 to Figure 5-12 three descriptors of these Q3 distributions are shown. The black icons depict the samples crystallised at a low cooling rate (RT), while the samples crystallised at a moderate (RF) and high (IB) cooling rate are represented by grey and blue icons respectively. The 90 % percentile of the Q3 distribution is shown as a circle, the 50 % and 10 % percentile by the crosses and diamonds. In all samples, irrespective of the cooling rate, formulation or storage period, the $x_{50,3}$ and $x_{10,3}$ diameter of the emulsion particles lied within a narrow range of 1-2 μm and 2-4 μm respectively. The $x_{90,3}$ however differed significantly between the samples depending on how they were formulated and for how long they had been stored. The 90 % percentile of the Q3 distributions is therefore additionally shown in a table format in Table 5-1 to Table 5-6.

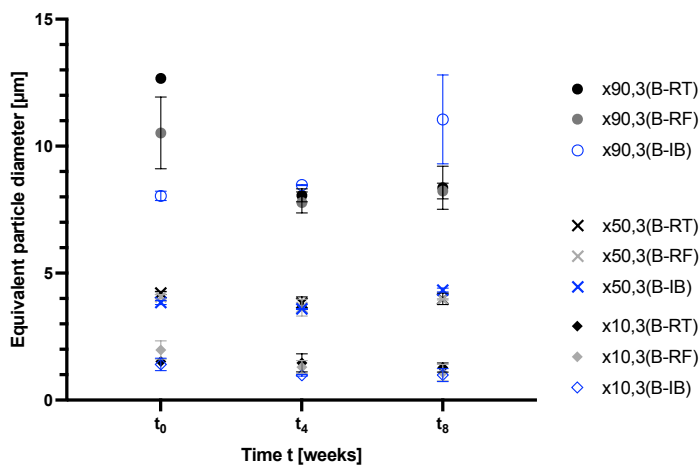


Figure 5-10 10 %, 50 % and 90 % percentile of the cumulative normalised undersize distribution of the B samples based on the particle volume. All values are averaged, the error bars indicate the SEM (N = 2, n = 3).

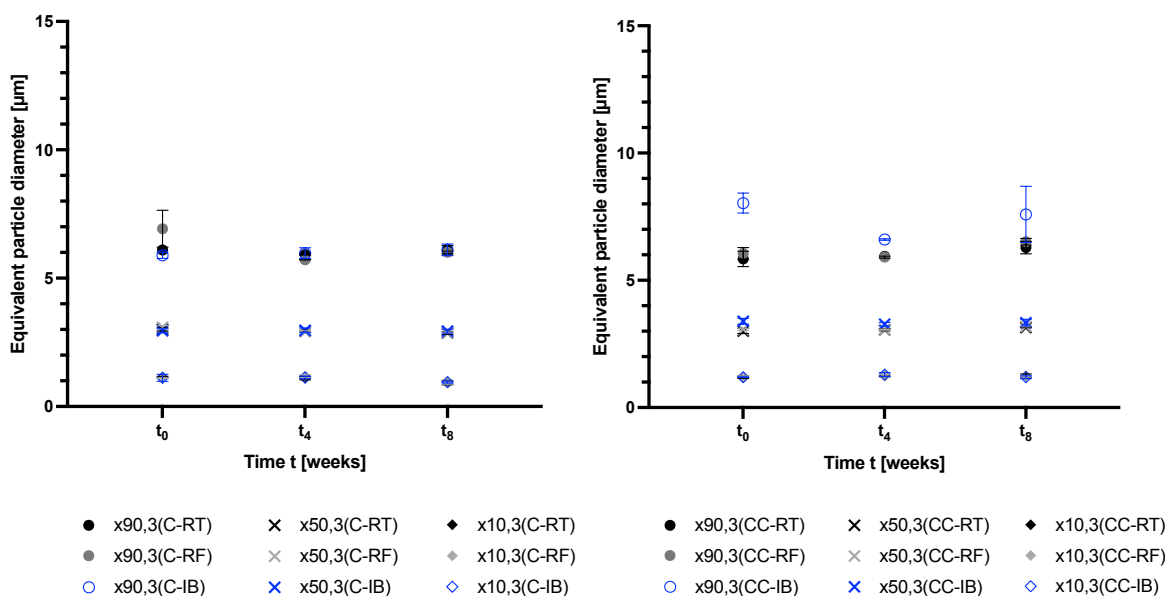


Figure 5-11 10 %, 50 % and 90 % percentile of the cumulative normalised undersize distribution of the C samples (left) and CC samples (right) based on the particle volume. All values are averaged, the error bars indicate the SEM (N = 2, n = 3).

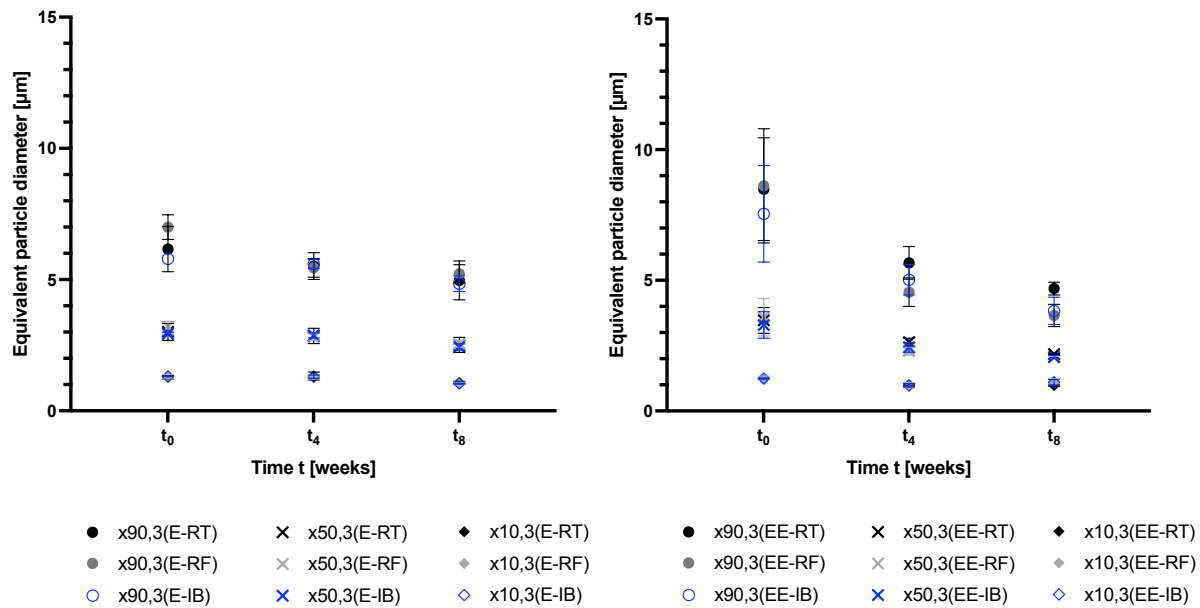


Figure 5-12 10 %, 50 % and 90 % percentile of the cumulative normalised undersize distribution of the E samples (left) and EE samples (right) based on the particle volume. All values are averaged, the error bars indicate the SEM (N = 2, n = 3).

Shapiro-Wilk and Kolmogorov-Smirnov tests proved that the data issued from the laser diffraction analysis were normally distributed ($p = 0.05$). Therefore one-way ANOVA ($p = 0.05$) was performed to check for statistical significance. The results for the effect of the formulation are shown in Table 5-1 to Table 5-6.

The $x_{90,3}$ diameter of the samples stabilised by β -lg alone was on average 30 % higher than that of the phospholipid containing samples. The effect was statistically significant for all cooling rates and at all measurement intervals but for the IB samples at t_0 (see Table 5-1, Table 5-2 and Table 5-3).

Table 5-1 90 % percentile of the cumulative normalised undersize distribution of the colloidal particles in all samples crystallised at low cooling rate (RT). B samples serve as reference. Values are given as mean \pm SEM, values marked with matching letters are significantly different according to one-way ANOVA with $p = 0.05$ (N = 2, n = 3).

RT					
	B	C	CC	E	EE
t_0	13 ± 0.027^{abcd}	6.1 ± 0.16^a	5.8 ± 0.30^b	6.2 ± 0.86^c	8.5 ± 2.0^d
t_4	8.1 ± 0.25^{efgh}	5.9 ± 0.028^e	5.9 ± 0.12^f	5.5 ± 0.51^g	5.7 ± 0.63^g
t_8	8.4 ± 0.85^{ijkl}	6.1 ± 0.18^i	6.3 ± 0.24^j	5.0 ± 0.74^k	4.7 ± 0.24^l

Table 5-2 90 % percentile of the cumulative normalised undersize distribution of the colloidal particles in all samples crystallised at moderate cooling rate (RF). B samples serve as reference. Values are given as mean \pm SEM, values marked with matching letters are significantly different according to one-way ANOVA with $p = 0.05$ (N = 2, n = 3).

RF					
	B	C	CC	E	EE
t_0	10.5 ± 1.4^{abcd}	6.9 ± 0.72^a	6.1 ± 0.23^b	7.0 ± 0.47^c	8.6 ± 2.2^d
t_4	7.8 ± 0.41^{efgh}	5.7 ± 0.012^e	5.9 ± 0.038^f	5.4 ± 0.36^g	4.5 ± 0.55^h
t_8	8.2 ± 0.31^{ijkl}	6.0 ± 0.043^i	6.5 ± 0.13^j	5.2 ± 0.35^k	3.7 ± 0.42^l

Table 5-3 90 % percentile of the cumulative normalised undersize distribution of the colloidal particles in all samples crystallised at high cooling rate (IB). B samples serve as reference. Values are given as mean \pm SEM, values marked with matching letters are significantly different according to one-way ANOVA with $p = 0.05$ ($N = 2$, $n = 3$).

IB					
	B	C	CC	E	EE
t_0	8.0 ± 0.18	5.9 ± 0.12	8.0 ± 0.39	5.8 ± 0.16	7.5 ± 1.8
t_4	8.5 ± 0.020^{abcd}	6.0 ± 0.21^a	6.6 ± 0.028^b	5.6 ± 0.17^c	5.0 ± 0.58^d
t_8	11 ± 1.7^{efgh}	6.1 ± 0.23^e	7.6 ± 1.1^f	4.8 ± 0.30^g	3.8 ± 0.52^h

When comparing the $x_{90,3}$ between the samples over the course of the storage period (see Table 5-4, Table 5-5 and Table 5-6), a statistically significant decrease of 20-30 % of the initial diameter was noted for the B samples crystallised at moderate and low cooling rate. The DSPE containing samples showed the same tendency. The effect was most pronounced in the samples with the higher DSPE concentration (EE) where the $x_{90,3}$ is on average 50 % lower at t_8 as compared to t_0 . The 90 % percentile of the Q3 distribution in the C and CC samples was stable over time.

Table 5-4 90 % percentile of the cumulative normalised undersize distribution of all B samples. Values are given as mean \pm SEM, values marked with matching letters are significantly different according to one-way ANOVA with $p = 0.05$ ($N = 2$, $n = 3$).

B			
	RT	RF	IB
t_0	13 ± 0.027^{ab}	10.5 ± 1.4^{cd}	8.0 ± 0.18^e
t_4	8.1 ± 0.25^a	7.8 ± 0.41^c	8.5 ± 0.020^f
t_8	8.4 ± 0.85^b	8.2 ± 0.31^d	11 ± 1.7^{ef}

Table 5-5 90 % percentile of the cumulative normalised undersize distribution of all C and CC samples. Values are given as mean \pm SEM, values marked with matching letters are significantly different according to one-way ANOVA with $p = 0.05$ ($N = 2$, $n = 3$).

C			CC			
	RT	RF	IB	RT	RF	IB
t_0	6.1 ± 0.16	6.9 ± 0.72^{ab}	5.9 ± 0.12	5.8 ± 0.30	6.1 ± 0.23	8.0 ± 0.39^d
t_4	5.9 ± 0.028	5.7 ± 0.012^a	6.0 ± 0.21	5.9 ± 0.12	5.9 ± 0.038^c	6.6 ± 0.028^d
t_8	6.1 ± 0.18	6.0 ± 0.043^b	6.1 ± 0.23^e	6.3 ± 0.24^i	6.5 ± 0.13^c	7.6 ± 1.1

Table 5-6 90 % percentile of the cumulative normalised undersize distribution of all C and CC samples. Values are given as mean \pm SEM, values marked with matching letters are significantly different according to one-way ANOVA with $p = 0.05$ ($N = 2$, $n = 3$).

E			EE			
	RT	RF	IB	RT	RF	IB
t_0	6.2 ± 0.86	7.0 ± 0.47^{ab}	5.8 ± 0.16^c	8.5 ± 2.0^{ef}	8.6 ± 2.2^{gh}	7.5 ± 1.8^{ij}
t_4	5.5 ± 0.51	5.4 ± 0.36^a	5.6 ± 0.17^d	5.7 ± 0.63^e	4.5 ± 0.55^g	5.0 ± 0.58^i
t_8	5.0 ± 0.74	5.2 ± 0.35^b	4.8 ± 0.30^{cd}	4.7 ± 0.24^f	3.7 ± 0.42^h	3.8 ± 0.52^j

The span describes the width of a cumulated undersize distribution and is calculated based on the $x_{10,3}$, $x_{50,3}$ and $x_{90,3}$ diameter as per Equation 4-3. While the 10 % and 50 % percentile of the particle size distributions have been shown to be more or less constant between the samples and over the storage time, the $x_{90,3}$ diameter differed depending on the formulation and the storage time.

Thus, the span showed a tendency corresponding to the observations made on the $x_{90,3}$ diameter, i.e. a more pronounced polydispersity of the emulsion particles in the B samples as compared to the phospholipid containing samples and an overall slightly increasing monodispersity over the storage time. The effects are however not statistically significant for all samples which can be read from Table 8-1 to Table 8-6 in the appendix. The time dependent increasing monodispersity is strongest in the B and EE samples, which show a significant drop of the span between t_0 and t_8 of up to 40 % of the initial value respectively.

5.3 Results on the Melting Behaviour and Crystal Polymorphism

5.3.1 Results on the Crystal Polymorphism

The X-ray diffraction patterns of the B, C and E samples measured at t_0 and t_8 are shown in Figure 5-13, Figure 5-14 and Figure 5-15. Due to resource restrictions, the CC and EE samples were excluded from the analysis and single measurements were performed on only one replicate of each sample.

On the x-axis the detection angle 2θ [°] was translated into the distance between the set of parallel planes in the fat crystals, i.e. the d-spacing [Å], according to Equation 4-4. The y-axis of the diagrams is omitted as the analysis of the X-ray diffraction measurements is done exclusively qualitatively. The background, produced by any amorphous structures in the samples, has not been subtracted from the diffraction patterns. Thus, only the peak position is of interest, the peak height however does not allow for interpretation. The data sets are normalised as to fit the results of two different measurement intervals (t_0 and t_8) into one diagram.

All samples, irrespective of the formulation, cooling rate and storage time, showed a broad, flat peak at 3.2 Å and a prominent, narrow peak at 4.2 Å. In most diffraction patterns, an additional more or less apparent peak at 3.8 Å could be identified. Only the samples crystallised at high cooling rate (IB) and the DSPC containing sample crystallised at low cooling rate (C-RT) displayed a peak at 4.6 Å after being stored for eight weeks.

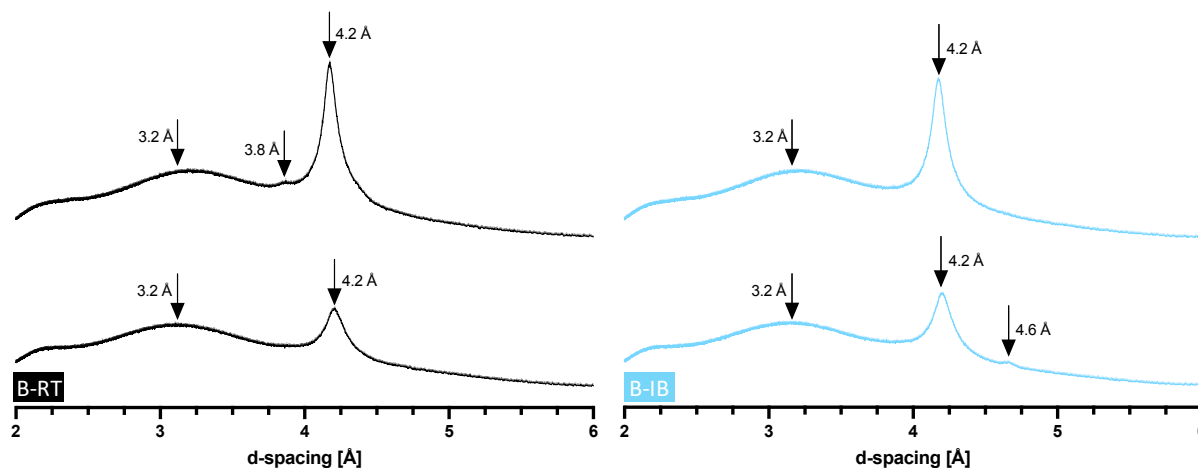


Figure 5-13 X-ray diffraction pattern of the B samples crystallised at low (left) and high cooling rate (right). Measurements performed at t_0 (top) and t_8 (bottom) ($N = 1$, $n = 1$). Arrows point to detectable peaks.

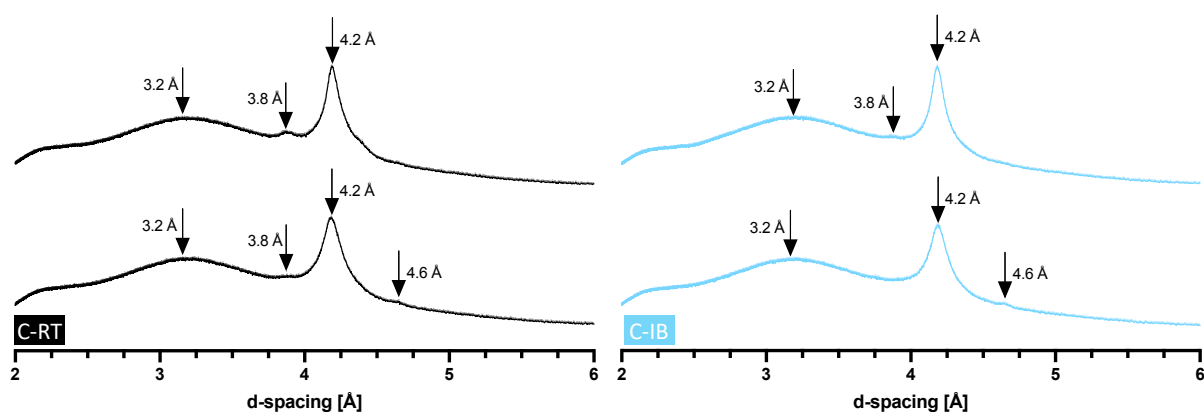


Figure 5-14 X-ray diffraction pattern of the C samples crystallised at low (left) and high cooling rate (right). Measurements performed at t_0 (top) and t_8 (bottom) ($N = 1$, $n = 1$). Arrows point to detectable peaks.

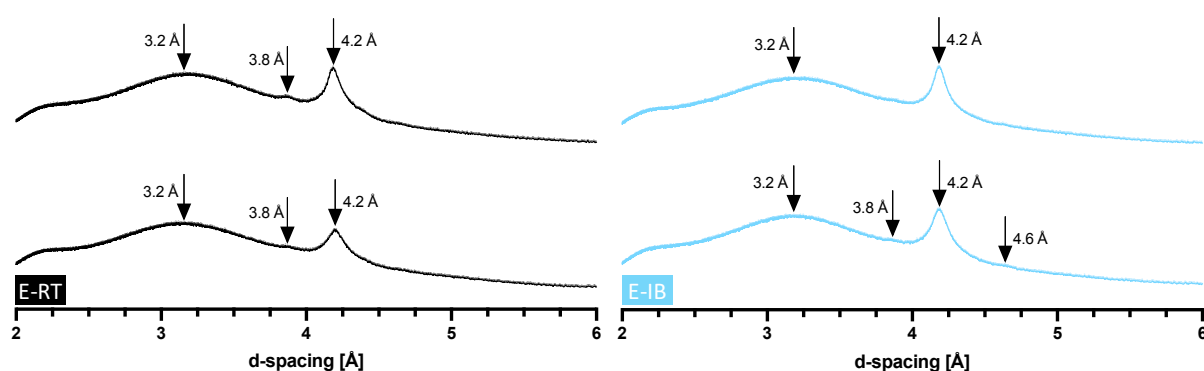


Figure 5-15 X-ray diffraction pattern of the E samples crystallised at low (left) and high cooling rate (right). Measurements performed at t_0 (top) and t_8 (bottom) ($N = 1$, $n = 1$). Arrows point to detectable peaks.

5.3.2 Results on the Melting Behaviour

The results of the differential scanning calorimetry are shown as curves averaged over both sample replicates in Figure 5-16 to Figure 5-20. The raw data, i.e. the DSC curves of the individual sample replicates can be found in Figure 8-13 to Figure 8-42 in the appendix. The y-axis in the figures below is omitted as the data were normalised to allow the representation of the results of two measurement intervals (t_0 and t_8) in one diagram respectively.

The melting behaviour of all samples, irrespective of the cooling rate and formulation, was characterised by two endothermic events, i.e. a first melting endotherm at about 47–48 °C and a second at about 56 °C, and one exothermic event, the latter with a peak temperature of 49–50 °C. After eight weeks of storage, a third endothermic peak appeared at a temperature varying between 41.5 °C and 44.9 °C. This ‘additional endotherm’ is most clearly visible in samples C-RT and E-RT in Figure 5-16 and Figure 5-17 below but was actually detected in all samples apart from the B samples crystallised at a moderate cooling rate (B-RF). The additional endotherm is best perceived from the DSC curves of the individual sample replicates in the appendix (see Figure 8-13 to Figure 8-42).

The endothermic peaks of the DSPE containing samples in Figure 5-19 and Figure 5-20 were generally lower and flatter as compared to those of the samples containing DSPC or β -lg alone (Figure 5-16 to Figure 5-18). The higher the DSPE concentration, the more reduced the peak height appeared.

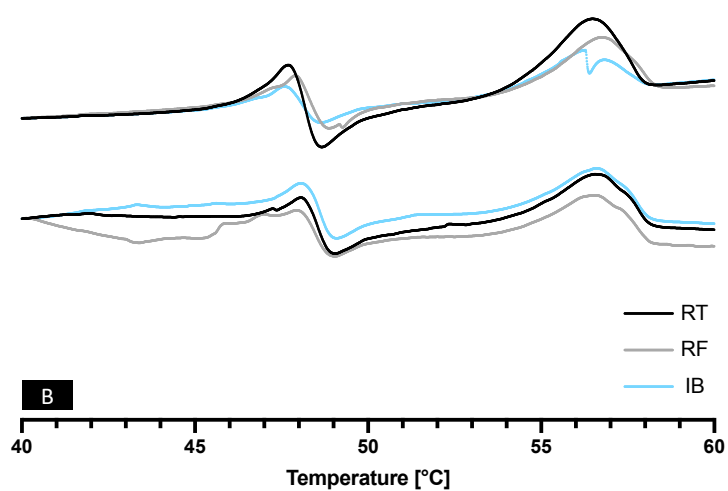


Figure 5-16 DSC curves of the B samples measured at t_0 (top) and t_8 (bottom). The curves are averaged over both sample replicates ($N = 2$, $n = 1$).

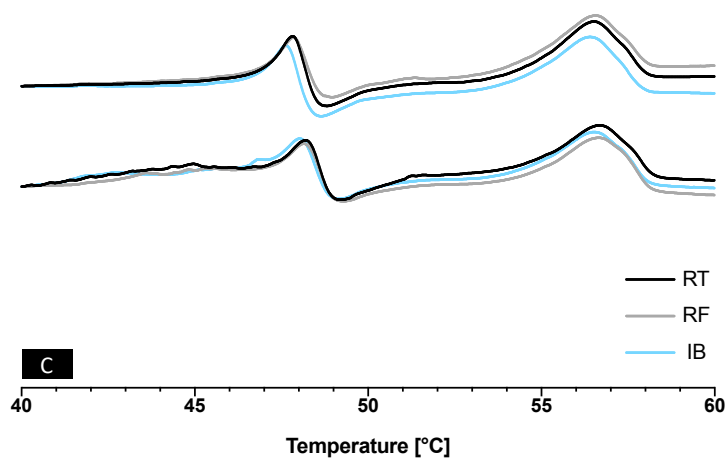


Figure 5-17 DSC curves of the C samples measured at t_0 (top) and t_8 (bottom). The curves are averaged over both sample replicates ($N = 2$, $n = 1$).

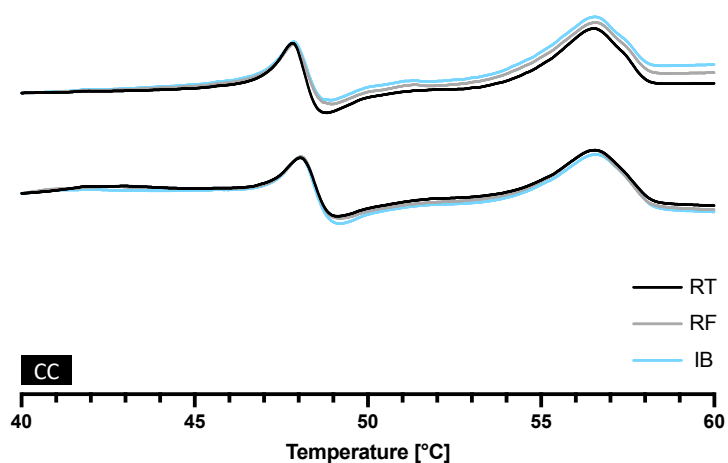


Figure 5-18 DSC curves of the CC samples measured at t_0 (top) and t_8 (bottom). The curves are averaged over both sample replicates ($N = 2$, $n = 1$).

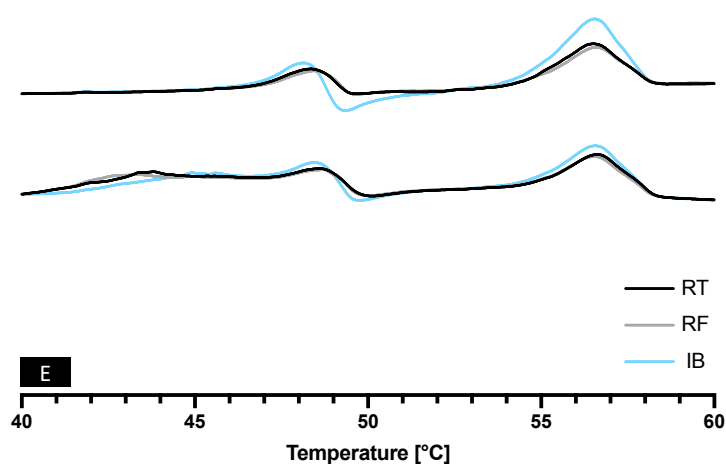


Figure 5-19 DSC curves of the E samples measured at t_0 (top) and t_8 (bottom). The curves are averaged over both sample replicates ($N = 2$, $n = 1$).

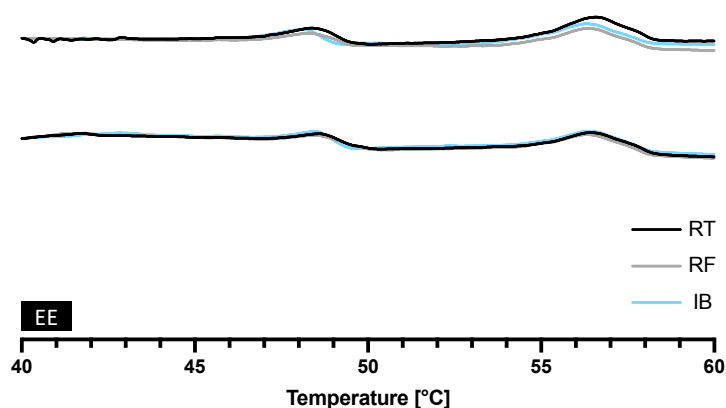


Figure 5-20 DSC curves of the EE samples measured at t_0 (top) and t_8 (bottom). The curves are averaged over both sample replicates ($N = 2$, $n = 1$).

More detailed conclusions on the samples' endo- and exothermic events can be drawn from the data in Table 5-7 to Table 5-11. The second endotherm had a constant peak temperature of 56.5 °C independent of the formulation, cooling rate or storage time. Conversely, the first endothermic event occurred at an average temperature of 47.9 °C at t_0 and only at 48.3 °C when determined at t_8 . This increase of the peak melting temperature of the first endothermic event over the storage time is however not statistically significant, which was accounted for by performing Mann-Whitney tests ($p = 0.05$). An increase of the peak temperature was also noted between t_0 and t_8 when considering the exothermic event. The average crystallisation temperature T_c was 49 °C for the freshly prepared samples and increased to 49.4 °C for the samples stored for eight weeks. This effect also turned out not to be statistically significant.

Table 5-7 Peak melting and crystallisation temperature of the endo- and exothermic peaks in the DSC curves of the B samples. Values are given as mean \pm SEM (N = 2, n = 1). T_m = melting temperature, T_c = crystallisation temperature, T_m add. = melting temperature of the additional endotherm, *no endotherm in the second sample replicate.

		B				
		no. of endotherms	T_m add. endotherm	T_m 1 st endotherm	T_m 2 nd endotherm	T_c exotherm
RT	t_0	2		47.6 \pm 0.150	56.2 \pm 0.255	48.7 \pm 0.065
RT	t_8	3	41.5 \pm 0.380	48.0 \pm 0.0500	56.5 \pm 0.600	49.0 \pm 0.070
RF	t_0	2		47.6 \pm 0.205	56.2 \pm 0.255	48.6 \pm 0.170
RF	t_8	2		48.0 \pm 0.0550	56.5 \pm 0.00500	49.0 \pm 0.025
IB	t_0	2		47.7 \pm 0.0650	56.4 \pm 0.210	48.6 \pm 0.020
IB	t_8	3	43.2*	48.0 \pm 0.0150	56.5 \pm 0.00	49.0 \pm 0.030

Table 5-8 Peak melting and crystallisation temperature of the endo- and exothermic peaks in the DSC curves of the C samples. Values are given as mean \pm SEM (N = 2, n = 1). T_m = melting temperature, T_c = crystallisation temperature, T_m add. = melting temperature of the additional endotherm, no endotherm in the second sample replicate.

		C				
		no. of endotherms	T_m add. endotherm	T_m 1 st endotherm	T_m 2 nd endotherm	T_c exotherm
RT	t_0	2		47.7 \pm 0.00500	56.4 \pm 0.0500	48.7 \pm 0.065
RT	t_8	3	44.9*	48.1 \pm 0.0550	56.6 \pm 0.00500	49.1 \pm 0.040
RF	t_0	2		47.8 \pm 0.0200	56.4 \pm 0.0500	48.6 \pm 0.170
RF	t_8	3	44.1 \pm 0.580	48.1 \pm 0.0400	56.6 \pm 0.0600	49.2 \pm 0.035
IB	t_0	2		47.6 \pm 0.160	56.3 \pm 0.175	48.6 \pm 0.020
IB	t_8	3	43.8 \pm 1.180	48.0 \pm 0.0100	56.5 \pm 0.0150	49.0 \pm 0.045

Table 5-9 Peak melting and crystallisation temperature of the endo- and exothermic peaks in the DSC curves of the CC samples. Values are given as mean \pm SEM (N = 2, n = 1). T_m = melting temperature, T_c = crystallisation temperature, T_m add. = melting temperature of the additional endotherm, no endotherm in the second sample replicate.

		CC				
		no. of endotherms	T_m add. endotherm	T_m 1 st endotherm	T_m 2 nd endotherm	T_c exotherm
RT	t_0	2		47.6 \pm 0.00	56.3 \pm 0.0300	48.6 \pm 0.020
RT	t_8	3	41.7*	48.1 \pm 0.110	56.5 \pm 0.150	49.0 \pm 0.110
RF	t_0	2		47.7 \pm 0.350	56.4 \pm 0.0850	48.7 \pm 0.130
RF	t_8	3	41.6 \pm 0.820	48.1 \pm 0.0500	56.5 \pm 0.0850	49.1 \pm 0.210
IB	t_0	2		47.6 \pm 0.0800	56.3 \pm 0.0800	48.6 \pm 0.020
IB	t_8	3	41.4 \pm 0.375	48.0 \pm 0.115	56.5 \pm 0.155	49.1 \pm 0.195

Table 5-10 Peak melting and crystallisation temperature of the endo- and exothermic peaks in the DSC curves of the E samples. Values are given as mean \pm SEM (N = 2, n = 1). T_m = melting temperature, T_c = crystallisation temperature, T_m add. = melting temperature of the additional endotherm.

		E				
		no. of endotherms	T_m add. endotherm	T_m 1 st endotherm	T_m 2 nd endotherm	T_c exotherm
RT	t_0	2		48.2 \pm 0.165	56.4 \pm 0.155	49.5 \pm 0.135
RT	t_8	3	43.5 \pm 0.240	48.6 \pm 0.0300	56.6 \pm 0.0300	50.0 \pm 0.090
RF	t_0	2		48.4 \pm 0.0250	56.5 \pm 0.0850	49.6 \pm 0.035
RF	t_8	3	42.7 \pm 0.360	48.6 \pm 0.0850	56.5 \pm 0.0950	49.9 \pm 0.090
IB	t_0	2		48.2 \pm 0.145	56.4 \pm 0.0250	49.3 \pm 0.170
IB	t_8	3	43.8 \pm 1.020	48.5 \pm 0.120	56.5 \pm 0.0150	49.7 \pm 0.170

Table 5-11 Peak melting and crystallisation temperature of the endo- and exothermic peaks in the DSC curves of the EE samples. Values are given as mean \pm SEM (N = 2, n = 1). T_m = melting temperature, T_c = crystallisation temperature, T_m add. = melting temperature of the additional endotherm, *no exo-/endotherm in the sample replicate.

		EE				
		no. of endotherms	T_m add. endotherm	T_m 1 st endotherm	T_m 2 nd endotherm	T_c exotherm
RT	t_0	2		48.3 \pm 0.0250	56.5 \pm 0.0750	49.7 \pm 0.265
RT	t_8	3	41.7*	48.6 \pm 0.0800	56.4 \pm 0.0800	50.3 \pm 0.255
RF	t_0	2		48.2 \pm 0.0800	56.3 \pm 0.0650	49.4*
RF	t_8	3	41.4 \pm 0.315	48.5 \pm 0.115	56.3 \pm 0.0450	50.0 \pm 0.400
IB	t_0	2		48.1 \pm 0.115	56.2 \pm 0.110	49.2 \pm 0.170
IB	t_8	3	41.7 \pm 1.085	48.5 \pm 0.0300	56.4 \pm 0.0850	49.7 \pm 0.215

The difference of the peak height observed between the DSPE containing samples and the remaining samples in the DSC curves, can be quantified by integrating the peak area from the point where the signal leaves and regains the baseline respectively. The graphical determination of the area under the endothermic peaks are shown in Figure 8-13 to Figure 8-42 in the appendix. The peak area is related to the energy H_m [mJ] that the samples absorb upon melting. A melting event is an energy consuming, i.e. endothermic, process. Thus, by heating the samples in the calorimeter, the change of the enthalpy of the samples, ΔH_m [mJ], is positive. This melting enthalpy is an indicator for the amount of solid fat (SFC) in the samples. As there were up to three melting events recorded in the DSC curves, the respective areas under the endothermic peaks can be summed up ('total melting enthalpy'), to give an estimation of the overall amount of solid fat, irrespective of the melting fraction or polymorphic form. The sample mass, that was used for the calorimetric measurements, differed between 9 mg and 11 mg (see 4.3.4). Dividing the melting enthalpy ΔH_m [mJ] by the sample mass [mg] and considering the mass percentage of disperse fat (5 wt%) in the samples, yields the melting enthalpy per unit mass of fat $\Delta H'_m$ [Jg⁻¹], which the comparison of the SFC between the samples can be based on. The experimental set-up of the DSC measurements does not allow for an absolute determination of the amount of crystalline fat in the samples but serves to compare the samples among themselves. These data are summarised in Figure 5-21 and Figure 5-22.

The total melting enthalpy per unit mass of fat of the DSPC containing samples was similar to that of the samples stabilised by β -lg alone. The DSPE containing samples however had a lower total peak area than the B samples. The effect was more pronounced for the EE samples than for the E samples with a decrease of 50 % and 30 % of the total melting enthalpy per unit mass of fat as compared to the corresponding B sample respectively (see Figure 5-22). The peak area of the B, E and EE samples cooled at slow and high rate (apart from EE-IB) decreased by 33 % on average between t_0 and t_8 (see Figure 5-22). Mann-Whitney tests showed that none of the observations made above were statistically significant ($p = 0.05$).

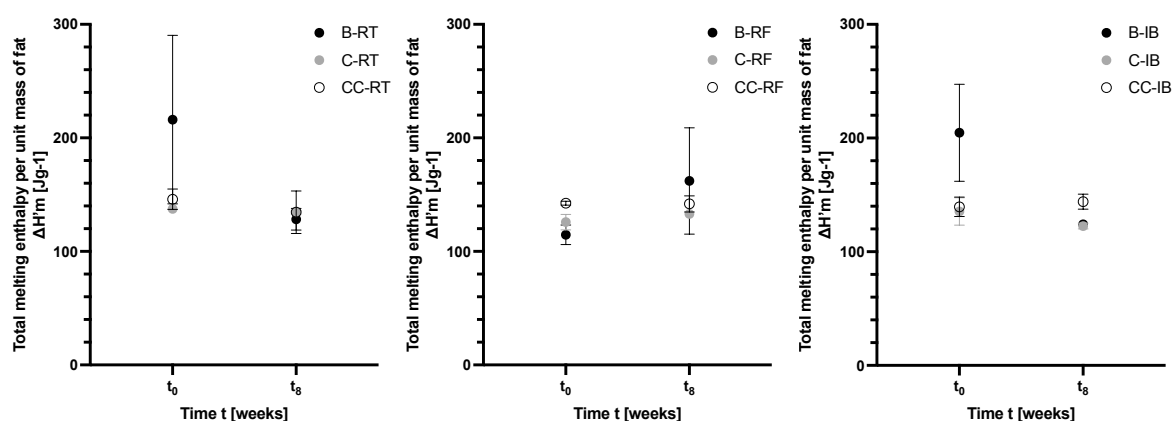


Figure 5-21 Sum of the melting enthalpy of all endothermic events recorded in the DSC curves of the B, C and CC samples (see Fig. 4-16 to 4-18) cooled at low (left), moderate (middle) and high (right) cooling rate respectively. Values are given as mean \pm SEM ($N = 2$, $n = 1$).

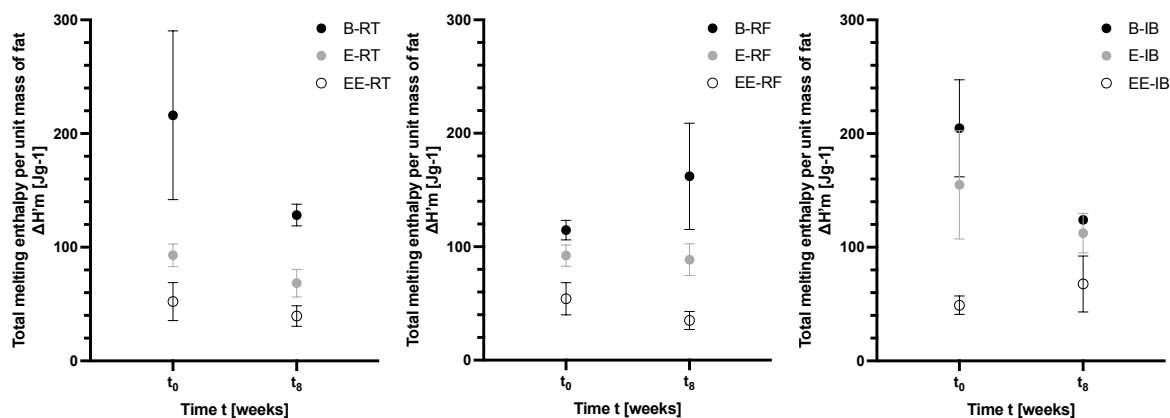


Figure 5-22 Sum of the melting enthalpy of all endothermic events recorded in the DSC curves of the B, E and EE samples (see Fig. 4-16, 4-19 and 4-20) cooled at low (left), moderate (middle) and high (right) cooling rate respectively. Values are given as mean \pm SEM ($N = 2$, $n = 1$).

5.4 Discussion

The results presented in chapters 4.1 to 4.3 are discussed in terms of their contribution to track and quantify colloidal instability mechanisms. The samples stabilised by β -lg alone (B samples) serve as reference. The samples with added DSPC (C and CC samples) and DSPE (E and EE samples) will sometimes be discussed together and therefore be combined under the term 'phospholipid containing samples'.

5.4.1 Evidence for Creaming

The phase separation, that occurred in all samples and over the entire storage period (see Figure 5-1 to Figure 5-3 and Figure 8-1 to Figure 8-5 in the appendix), is assumed to be the result of a creaming process. The top layer is considered to consist of fat particles, that float up due to their low density and may be aggregated and/or (partially) coalesced. The bottom phase ('serum phase') would consequently be mainly composed of aqueous continuous phase. The observations suggest that the fat particles creamed and floated up slowly, thereby creating a gradient within the serum phase. This would then have led to the visual separation into a thin, clear layer at the very bottom of the sample containers and main serum phase. The bottom layer was probably completely void of fat particles, while the remaining serum phase still contained fat particles but at a lower volume fraction compared to the initial emulsion. Neither the cooling rate, nor the formulation seemed to have had an impact on the tendency of the emulsion system to undergo phase separation, given that the absolute height of the creamed layer reached an identical level in all samples after eight weeks of storage (see chapter 5.1). As the phases were miscible again upon agitation, the fat particles in the creamed layer cannot have fully merged by coalescence. This is in agreement with the microscopic images, where no extensive coalesced structures were found (see Figure 4-4 to Figure 4-9). That also proves that the rigidity of the creamed layer, observed in the B samples, was not a result of more extensive coalescence but might instead have been provoked by bridging between the protein-covered particles surfaces (see chapter 2.2.1). The addition of DSPC or DSPE might have prevented that, which would explain why the phospholipid containing samples had a more liquid and more easily miscible creamed layer. This would also be consistent with the findings made by McClements et al. (1993b). They show that flocculation is enhanced in emulsions stabilised by whey proteins alone whereas the addition of low molecular weight emulsifiers (LMWE) leads to the dissolution of the flocs by a displacement of the proteins from the interface. This is what might have happened to the emulsion particles in the creamed layer. The hypothesis could be tested by examining the interfacial composition of the emulsion particles and by quantifying the rigidity of the creamed layer. This could be done by microscopic and rheological analyses of the creamed layer. Tensiometric measurements would allow to characterise the type and concentration of emulsifier adsorbed at the oil-water interface.

5.4.2 Evidence for Mass Transport Processes

There are several colloidal instability mechanisms that lead to a change of the average diameter and size distribution of the disperse fat particles in O/W emulsions. These can be tracked and quantified by laser diffraction analysis and microscopy.

Flocculation is detectable as an increased average particle size and an overall shift of the size distribution pattern from smaller to bigger diameters. The dilution and intense stirring of the samples in the fraction cell bear the risk of disrupting flocculated emulsion particles, which can thereby distort the results. The light scattering pattern of partially or fully coalesced droplets is undistinguishable from that of flocculated particles as it shows the same characteristics: an increased average droplet size and a shift of the size distribution from smaller to bigger diameters. Partially coalesced droplets are however unlikely to dissociate when stirred in the fraction cell. As total coalescence is an irreversible process, fully coalesced droplets are completely insensitive to dilution and mechanical stresses. Unlike flocculation and (partial) coalescence, Ostwald ripening results in a polarisation of the light scattering pattern, i.e. a broadening of the size range, as the diameter of the small particle fraction decreases and that of the big particle fraction grows.

Microscopic examinations are non-destructive and allow to easily identify flocs of emulsion particles as tightly packed groups of particles, that retain their identity. Because only a very small volume of each sample (10 μl) was analysed microscopically, it was vital to mix the sample thoroughly prior to taking a sample aliquot. Partial coalescence is visible as solid or liquid bridges between particles, that are closely aligned. The microscopic analysis of the samples could not be performed dynamically, i.e. the development of the microstructure of one and the same sample aliquot could not be observed over the course of time, because evaporation of the sample could not be prevented even if the cover lid was sealed with glue. Instead, snapshots of different sample aliquots were taken at distinct sampling intervals. These snapshots most often only reveal the result or endpoint of a development that the sample has undergone during storage. It is however rare to capture a phenomenon in process. The resolution limit of the microscope, used in this study, is reached at about 1 μm . Thus, emulsion particles with a diameter in the submicron range could not be visualised.

There is little evidence for the occurrence of coalescence in the microscopic images (see Figure 5-9). Flocculated emulsion particles however were found in all samples and over the entire storage period (see Figure 5-4 to Figure 5-8). While the cooling rate did not seem to have had an impact on the rate of flocculation, flocculation was clearly more pronounced in the phospholipid (PL) containing samples and occurred most extensively in the samples with added DSPE. The emulsion particles are assumed to be stabilised by a mixed interfacial layer consisting of β -lg and DSPE or DSPC respectively. A total displacement of the proteins by the PLs is not to be expected as the emulsifiers are known to be able coexist at oil-water interfaces (see chapter 2.2.2). Although the exact composition of the interfacial

layer was not determined in this study, it can be hypothesised that the interactions between the PLs and the β -lg at the emulsion interfaces led to the observed amplified flocculation in the phospholipid containing samples. LMWEs and proteins have been shown to undergo complexation when co-adsorbed at the surface of emulsion particles. The complexes can then have new characteristics, that differ from those of the individual emulsifiers (Bos and van Vliet, 2001). This is what might have happened to the β -lg and the DSPE or DSPC molecules; they formed complexes, which had a reduced stabilising effect on the emulsion interfaces.

Over the course of the sample storage, the median and the 10 % percentile of the particle size distribution remained largely unaltered, deviating only by about ± 1 -2 μm (see 5.2.2). Changes of the particle size within this range cannot reasonably be assumed to have an impact on the physiochemical characteristics or the colloidal stability of the emulsion particles. The $x_{90,3}$ diameter however showed a clear time- and formulation-dependent tendency. It decreased by about 20 % in the reference samples and by 50 % on average in the DSPE containing samples over eight weeks of storage. The emulsion particles in the phospholipid containing samples had an overall 30 % lower $x_{90,3}$ diameter than the emulsion particles stabilised by β -lg alone. Hence, the results of the laser diffraction analysis suggest that the particle size distribution in the B, E and EE samples became more monodisperse over time and that the size span of the emulsion particles in the phospholipid containing samples was generally narrower. The greater polydispersity of the emulsion particles in the reference samples was already apparent in the freshly prepared samples (at t_0). The higher amount and bigger diameter of the fraction of big particles in the reference samples must therefore have been a result of a less successful droplet stabilisation during the homogenisation of the samples. Maybe it was due to the generally slower adsorption kinetics of the proteins (see chapter 2.2.1), that the emulsion droplets in the reference samples were less efficiently stabilised directly after the droplet break-up in the colloidal mill. A less stabilised, partly uncovered emulsion particle interface might then have made some emulsion droplets coalesce and fuse to become bigger droplets. The addition of phospholipids, which adsorb faster due to their smaller size and higher surface affinity (see chapter 2.2.1), might have counteracted coalescence in the phospholipid containing samples and therefore have led to the occurrence of fewer and smaller above-average sized emulsion particles in those samples.

The microscopic images support the findings made based on the laser diffraction analysis. The majority of the emulsion particles had a diameter of about 2-3 μm irrespective of how long the samples had been stored, how fast they had been crystallised or how they had been formulated. In the B samples, the emulsion particles had a maximum size of up to 20 μm and a highly disperse size distribution (see Figure 5-4). The emulsion particles in the DSPC and DSPE containing samples only reached a maximum size of about 10-15 μm and 6-8 μm respectively and the size distribution appeared more monodisperse (see Figure 5-5 to Figure 5-8). The monodispersity was more pronounced the higher the phospholipid

concentration. Between t_0 and t_8 fewer big droplets were found in the B, E and EE samples. A monodisperse particle size distribution is favourable for the colloidal stability of an emulsion system. In this regard, the addition of DSPC or DSPE must therefore be judged to contribute to an improved colloidal stability of the samples.

To summarise, all samples had a comparable average particle size, that remained unchanged over eight weeks of storage. The size distribution of the reference samples was generally more polydisperse than that of the phospholipid containing samples. This was due to a higher number of above-average sized particles that additionally had the biggest maximum diameter. The size distribution narrowed down in the B, E and EE samples over a period of eight weeks, which was again a result of a change in the fraction of the biggest emulsion particles.

These findings are inconsistent with colloidal instability mechanisms common for O/W emulsions. The latter would lead to a polarisation of the particle size distribution and/or a shift of the average particle size. A possible assumption, that would explain the above mentioned observations, is that extensive mass transport processes occurred between the fat particles of the studied emulsions. These would lead to a redistribution of the TAG molecules between the fat particles and could thereby entail a change of the particle size distribution. Two mass transport mechanisms, namely compositional ripening and solubilisation have been shown to occur in triacylglycerol emulsions (see chapter 2.1.5). McClements et al. (1993b) argue that these two processes generally dominate over Ostwald ripening as the difference in Laplace pressure, driving Ostwald ripening, is lower than the driving force for compositional ripening and solubilisation, i.e. the entropy of mixing. The authors assume this to account for the fact that they did not see an increase in the average droplet size in their samples. The same might apply to the model emulsions studied in the scope of this project and explain the finding that there is no difference in the $x_{50,3}$ diameter.

Samtlebe et al. (2012) have observed the migration of individual fat molecules between a fraction of liquid emulsion droplets containing MCT oil and a fraction of solid lipid nanoparticles made from hydrogenated palm oil. They claim that the unbalanced distribution between the two fat fractions, differing in their nature and state, leads to a diffusion of liquid MCT oil molecules to the solid palm oil particles. The authors believe that the liquid MCT oil molecules get solubilised in the aqueous phase, diffuse to the surface of the SLNs, adsorb at their surfaces and dissolve solid palm oil crystals in the adsorbed surface layer. According to this mechanism, the dissolved fat crystals would then diffuse in the opposite direction, i.e. towards the liquid MCT oil droplets, which would further enhance the entropically favourable mixing process. It is reasonable to assume that the emulsion systems studied in this report contain fully solidified TAG particles, as well as partially crystalline and supercooled liquid TAG droplets. That is because emulsified fats show a crystallisation behaviour different from that of the bulk fats. Emulsified TAGs crystallise mainly via a homogenous nucleation process and therefore a

significantly higher level of supercooling is needed to induce nucleation and subsequent crystal growth (see chapter 2.1.4). Even though nearly all emulsion particles (see circled structure in Figure 5-9) appeared coloured under polarised light and would thereby be assumed to be fully crystalline, the microscopic images do not allow to draw conclusions about the crystallinity of the submicron-sized emulsion droplets as these are below the resolution limit of the method. Yet the smallest emulsion droplets are the ones to be most likely to remain in a supercooled liquid state. That is because the smaller the droplet size, the higher the Laplace pressure and the lower the melting and crystallisation temperature. Thus, a high level of supercooling is needed to induce crystallisation. Additionally, due to their small volume, small emulsion droplets have a low probability to contain a catalytic impurity and therefore mainly crystallise via a homogenous nucleation mechanism, which again requires a high level of supercooling (see chapter 2.1.4). Differential scanning calorimetry complements the microscopic images in this regard. It allows to determine the fraction of crystalline fat in all emulsions droplets irrespective of their size. Thus, even though the microscopic images revealed no clear difference of the solid fat content between the samples, it is not contradictory that the results of the DSC measurements suggest otherwise. However, caution has to be paid when analysing the DSC data of this study. The results lack statistical significance as the DSC measurements were performed on both sample replicates but without a technical replicate ($N = 2$, $n = 1$) due to time constraints. This is assumed to have severely impaired the statistical power of the analysis. It must also be expected that the sampling process has failed to provide homogenous sample aliquots. The sample aliquots must have contained a higher amount of disperse fat (> 5 wt%) as compared to the actual emulsion system. This might have been due to the glass pipettes used for the sampling process. Upon wetting of the glass pipettes with the sample material, the acting capillary forces might have led to a disproportionately high transfer of fat droplets into the sample aliquot volume. This would explain why the melting enthalpy for some samples was higher than the literature value for the β' polymorphic form of a mixed TAG molecule containing stearic and palmitic fatty acids (expected to be around 200 Jg^{-1} , see Zéberg-Mikkelsen and Stenby (1999), i.e. the two major FA fractions of the hydrogenated palm oil used as the disperse fat phase. Repeated measurements and a more accurate sampling process would have allowed to draw more reliable conclusions. It also needs to be pointed out that the results of the DSC analysis allow for a comparison between the samples but not for a determination of the solid fat content in absolute terms. The area integrated over the endothermic peaks in the DSC curves served to quantify the amount of crystalline matter in the sample aliquots (see chapter 5.3.2). The peak area of the DSPE containing samples was lower than that of the B samples irrespective of the cooling rate and the storage time. The effect seemed however to be concentration dependent as the peak area was reduced by 30 % and 50 % in the E and EE samples respectively (as compared to the reference). This would suggest that DSPE has an inhibitory effect on the crystallisation of the emulsified TAGs. This

disproves the assumption that DSPE acts as a template to induce a surface heterogeneous nucleation process (see chapter 2.2.3). Given that the SFC was not raised by the addition of DSPC either (as compared to the reference), none of the two phospholipids tested in this study can be assumed to act as templates for the crystallisation of the emulsified hydrogenated palm oil. The similarity in terms of the chain length and the degree of saturation between the phospholipids and the fat phase seems to not have played a role to help crystallise the emulsified TAGs, conversely to what had been reported by several authors (see chapter 2.2.3).

The DSC measurements also revealed a decrease of the SFC in the B, E and EE samples of around 30 % between t_0 and t_8 (see Figure 5-21 and Figure 5-22). This might be due to the solubilisation process discussed above where the disbalance of the SFC between different fractions of emulsion particles would lead to the migration of liquid TAG molecules towards fully crystallised fat particles and a dissolution of fat crystals in the outer layer of the emulsion particles (Samtlebe et al., 2012).

The DSC patterns were marked by several distinct endothermic events, which is a highly uncommon finding in emulsified fats (see chapter 5.3). In the experimental design of this study, hydrogenated palm oil was used as the disperse fat phase. This type of complex natural fat is composed of mixed TAGs esterified with over 95 % 16:0/18:0 FAs and a remaining fraction of 12:0/14:0 FAs (see chapter 4.2.1). This compositional diversity commonly leads to the formation of mixed fat crystals with a very broad melting range, that results in a single, broad endothermic peak in DSC experiments (Bayard et al., 2022). The distinct endotherms observed in this study, must be assumed to be due to an unequal distribution of short- and long-chain FAs over the emulsion droplets. A separation into a fraction of TAG crystals containing short-chain FAs (12:0, 14:0 and 16:0), melting at lower temperatures (LMF), and a fraction of high-melting TAG crystals (HMF) with a long-chain FA profile (16:0 and 18:0) is to be expected. It was also noted that the first endothermic event approached the second endothermic event in all samples with a peak temperature rising from 47.9 °C on average at t_0 to 48.3 °C on average at t_8 (see Table 5-7 to Table 5-11). This might again be related to a mass transport process occurring between the emulsion particles as has been described by Samtlebe et al. (2012). In this case, the disbalance between the HMF and LMF of the TAG crystals would lead to the migration of liquid TAG molecules from the low melting fraction to the HMF of the emulsion particles. A dissolution of some long-chain, crystalline TAG molecules would occur, and these would then migrate back to the LMF emulsion particles. This would result in an increased melting temperature of the LMF.

In conclusion, it can be reasonably assumed that there is an overall unequal distribution of both high- and low-melting and solid, semi-crystalline and liquid TAG fractions over the emulsion particles. Following the line of reasoning of Samtlebe et al. (2012) and McClements et al. (1993b) this would enhance mass transport processes between the emulsion particles until reaching an equilibrium distribution of the different TAG molecules.

Other than the presumed strong compositional differences of the emulsion particles, mass transport processes can also be expected to be enhanced by the presence of β -lactoglobulin in the emulsions studied in the scope of this project. Beta lactoglobulin has a very specific tertiary structure which allows binding and transport of apolar ligands (see chapter 2.1.5). The formulation of all samples produced in the scope of this study includes β -lg in a concentration slightly above the protein's critical interfacial concentration (Schestkova et al., 2020). It can therefore be assumed that there was an excess of β -lg molecules that were not adsorbed to the emulsion droplet interfaces but instead solubilised in the aqueous continuous phase. These could have bound individual, liquid TAG molecules to their hydrophobic pocket and thereby have enhanced inter-droplet mass transfer processes. This is further supported by the observation that the serum phase of the samples differed in its turbidity depending on the emulsion formulation. While the serum phase of the emulsions stabilised by β -lg alone were highly opaque and intensely white over the total storage period, the phospholipid containing samples had a clear serum phase that turned turbid and white only after eight weeks of storage (see chapter 5.1). This cannot be related to a size difference of the emulsion particles given that particles were biggest in the reference samples (see results on $x_{90,3}$ in Table 5-1 to Table 5-3). Bigger particles would lead to less light scattering and thus a less turbid serum phase. Hence, it was hypothesised that the opacity of the serum phase was instead connected to the amount of solubilised protein. Consequently, there would be less beta lactoglobulin solubilised in the aqueous continuous phase and correspondingly more β -lg adsorbed to the oil-water interface in the phospholipid containing samples up until week eight, when the protein would desorb from the emulsion particle surface and the soluble protein fraction in the serum phase would increase and meet the level of the reference samples. Bylaite et al. (2000) proposed a mechanism that supports this hypothesis. They assume that the interfacial load of β -lg can be increased by the addition of small amounts of phospholipids. This could be tested by performing a Bradford assay on the serum phase of the samples to quantify the amount of solubilised protein and to determine the amount of adsorbed protein by subtraction.

Apart from proteins, other emulsion components are also able to promote mass transport processes of TAG molecules over the aqueous continuous phase. Weiss and McClements (2000) have studied the solubilisation of TAGs by incorporation into micelles formed by low molecular weight emulsifiers (LMWE). Whether a LMWE is micelle-forming or not depends on its concentration, which needs to be above its CMC, and its morphology. The C and E samples contain phospholipids added at a concentration below the CMC of their phospholipid component respectively. Micelle formation is therefore not assumed to occur in these samples. If DSPE is assumed to form reverse micelles just like soy PE (see Figure 5-9), no incorporation or solubilisation of TAG molecules would be expected. Conversely, DSPC might allow for the accommodation of TAG molecules in its hydrophobic core if it

forms lamellar structures as seen with soy PC (see Figure 2-9). If the micellar transport of TAG molecules would predominate over the 'protein carrier' mechanism, the CC samples would be clearly distinct from the other samples. This was however neither observed in the microscopic images nor concluded from the particle size distributions. Thus, the influence of β -Ig on mass transport processes must be assumed to be much more important in this emulsion system. A minor contribution of the micellar transport mechanism by the DSPC molecules is however still plausible.

5.4.3 Evidence for Polymorphic Transitions

The results of the XRD measurements suggest that the TAG crystals undergo polymorphic transitions over the storage time. Polymorphic transitions are known to promote flocculation because the rearrangement of one crystal form into another exposes patches on the emulsion particle surfaces that are not covered by emulsifier molecules and therefore attract each other (see chapter 2.1.5).

The broad peak at 3.2 Å, that appeared in all XRD spectra, did not match any reference values for the crystallographic data of TAG crystals. Conversely, the d-spacing corresponds to the diffraction pattern of potassium sorbate, which shows a prominent peak at 3.2 Å and several weak peaks in the range of 2.7 to 3.9 Å (Nakayama and Hayashi, 2014, Pang et al., 2015). As potassium sorbate was used in quite substantial amounts in this study to prevent sample spoilage, the 3.2 Å peak could be due to a fraction of this preservative, that crystallised in the aqueous continuous phase. The peaks at 4.2 Å and 3.8 Å, that were found in all or almost all XRD spectra, can be clearly assigned to the β' polymorph of TAG crystals (see Table 4-7). The occurrence of Maltese crosses in some emulsion particles, when observed under polarised light (see Figure 5-9 middle-right and right), supports this finding given that the β' crystal is known to produce this type of microscopic effect (Ueno et al., 2008).

The samples, that were crystallised at a fast cooling rate (IB), showed an additional peak at 4.6 Å when analysed after eight weeks of storage. A d-spacing of 4.6 Å is characteristic for the β polymorph (see Table 4-7). Based on these findings it can be concluded that the emulsified triacylglycerols existed in their β' polymorphic form in all samples and that this form was stable in the samples crystallised at low and moderate cooling rate over eight weeks of storage, while the samples crystallised at high cooling rate showed evidence for polymorphic transitions from the β' to the β polymorph when stored for eight weeks. This is in disagreement with the literature that states that a rapid cooling delays polymorphic transitions (Awad et al., 2008). The impact of the polymorphic transitions on the colloidal stability of the IB samples must however be minor as the other analytical methods gave no indication that the samples crystallised at high cooling rate would be any different from the others.

The results of the XRD analysis help to interpret the observations made on the melting behaviour of the samples. All DSC curves were marked by at least two endothermic and one exothermic event. The exotherm had a peak temperature of 49 °C on average. It appeared after the endothermic peak of the

low melting fat fraction and prior to the endotherm of the high melting fat fraction (see Figure 5-16 to Figure 5-20). Thus, a crystallisation event must have taken place at 49 °C. Polymorphic transitions lead to the formation of a thermodynamically more favourable crystal form and thereby release energy. Based on this, it can be hypothesised that the exothermic peak is due to the transition of a fat crystal polymorph of the low melting fat fraction into a polymorphic form with a melting temperature similar to that of the high melting fat fraction. Upon further melting, it would therefore blend into the second melting endothermic peak and not appear as an individual melting event. This would correspond to the observations made by Awad et al. (2008), who showed that TAGs, containing short-chain FAs, generally undergo polymorphic transitions faster than TAGs with a long-chain FA profile. As the XRD measurements did not show any evidence for the presence of alpha crystals, it can be ruled out that the exothermic peak was produced by the transition of an α to a β' polymorphic form. It is therefore reasonable to assume that the observed exothermic event is due to the transition of a number of low melting TAG crystals initially present in their β' form into their β polymorph. In a simplistic view, assuming the melting temperature of a mixed TAG molecule is about the average of the melting temperature of the FAs it is composed of, the β' crystals of a triacylglycerol esterified with one myristic, one lauric and one palmitic fatty acid would have a melting temperature of around 47 °C and its β polymorph would have a melting temperature of 55 °C (see Table 2-1). These temperatures approximate the peak temperatures of the exothermic and the second endothermic event of the DSC curves.

6 Conclusion and Outlook

6.1 Summary

Based on the data of the microscopic, visual and laser diffraction analysis, the model emulsion system investigated in the scope of this project can be described as storage stable over a period of eight weeks. The majority of all emulsion particles with a diameter of 1 μm and above appeared spherical and fully crystalline. Partial or total coalescence were only rarely observed. The average diameter of the emulsion particles was constant and small (about 2-3 μm). Only the DSPC containing samples and the samples crystallised at high cooling rate showed evidence for polymorphic transitions. The TAG crystals in all other samples existed in only one polymorphic form (β') that was stable over the studied storage time. Even if creaming occurred in all samples, the separated phases were more or less easily miscible again upon agitation. This was true for all samples independent of their formulation and cooling rate.

While (partial) coalescence and polymorphic transitions were not identified as a major risk factors to the structural integrity of the samples, the results of the laser diffraction analysis and the DSC measurements added a new dimension to the assessment of the overall stability of the studied emulsion system. These analytical methods provided evidence for the migration of individual TAG molecules between a high- and low-melting and a solid, semi-crystalline and liquid fraction of emulsion particles. This kind of mass transport process can potentially change the composition and size distribution of the emulsion particles and thereby alter their physicochemical properties such as their appearance, rheology and stability. These parameters affect for instance the sensory characteristics of food products. A changed viscosity, colour or mouthfeel can make the product unappealing. In other application areas, a transport or exchange of individual TAG molecules between the emulsion particles or between the disperse and the continuous phase might even lead to a loss of the products' functionality. This is true for products where the disperse fat phase acts as carrier for sensitive hydrophobic agents like drugs, functional ingredients or additives (e.g., colours, flavours or preservatives). Administering hydrophobic agents in a crystalline carrier allows for a more targeted and efficient delivery and an enhanced bioavailability. Migration and/or partial dissolution and solubilisation of the crystalline carrier material could therefore affect the delivery, stability and functionality of the hydrophobic agent.

Thus, mass transport processes occurring during storage can be expected to impair the quality and functionality of emulsion based products. This shows that there is an actual need to consider migration of individual TAG molecules as a factor causing colloidal instability in triacylglycerols emulsions with a semi-crystalline disperse phase. For a given product application, it can therefore be necessary to assess the consequences of this phenomenon and to explore possible approaches to prevent or to limit it.

6.2 Conclusions

In this study, the cooling rate was chosen to be investigated as a factor that could potentially lead to a smaller crystal size and to delayed polymorphic transitions. Apart from the adverse effect of a fast cooling process on the storage stability of the crystal polymorphs, the cooling rate did not have a clear impact on any of the emulsion characteristics. As a fast cooling process is highly energy demanding and did not bring about any benefit for the colloidal stability of the model emulsion system, it would be neither cost efficient nor sustainable to apply a high cooling rate to crystallise the dispersed fat phase.

Phospholipids (PLs), that are used as emulsifiers in O/W emulsions, have been shown to induce a surface heterogeneous crystallisation process via a mechanism known as 'template effect'. It requires the adsorption and premature crystallisation of the PLs on the emulsion interfaces and a highly similar FA profile of the emulsifier and the fat phase. In this study, the two phospholipids DSPC and DSPE were chosen, as they match the FA profile of the main TAG fraction of the dispersed fat phase in terms of the degree of saturation and chain length. It was therefore expected that a formulation with added DSPC or DSPE would yield a more fully crystalline fat phase. DSPC was thought to display a higher surface affinity as compared to DSPE because of its higher HLB value and to therefore locate more efficiently at the emulsion particle surfaces. The DSC measurements did however not confirm any of these expected effects. While DSPC had no influence on the solid fat content of the emulsions, DSPE seemed to even inhibit the fat crystallisation in the emulsion particles.

The observations made on the macro- and microstructure of the emulsions and the results of the laser diffraction analysis provide reasonable grounds to assume that DSPC and DSPE did successfully adsorb to the oil-water interface and that they co-existed and possibly interacted with the β -lg molecules. The turbidity of the serum phase of the emulsions gave an indication for a possible difference in the protein surface load depending on the addition of PLs. In this regard, the co-adsorbed emulsifiers would have had a beneficial effect on the elasticity of the creamed layer. When considering the size distribution of the emulsion particles, the addition of PLs was hypothesised to lead to a faster and more efficient stabilisation of the newly created surfaces upon the droplet break-up in the colloidal mill. This might have prevented premature coalescence and explain why the phospholipid containing samples had a more monodisperse particle size distribution than the samples stabilised by β -lg alone. The microscopic images however also revealed that the DSPE and DSPC containing emulsions flocculated more extensively. This was suspected to be the result of a complexation of the PLs with the proteins in the interfacial film. In summary, the addition of DSPC and DSPE had both beneficial and adverse effects on the colloidal stability of the model emulsion system, which seemed to be independent of their concentration. This study is based on analytical methods, that do not allow to draw conclusions on the actual composition of the interfacial layer. Additional methods such as tensiometry and SEM could shed light on the exact localisation of the phospholipids and their mode of interaction with β -lg.

The usage of additives in the food, cosmetics and pharma industry is not only a question of resource efficiency and costs but can also impair the attractiveness and even the safety of the product they are applied to. Consumers call for clean label products with short and transparent ingredient lists. Phospholipids are milk inherent, technologically appealing compounds but if they provide no benefit to the product stability, there is obviously no interest in using them as additives.

6.3 Outlook

This study was limited to a period of eight weeks. Some of the observed effect only became apparent at the last measurement interval, as for instance the change of the degree of turbidity of the serum phase. It has to be expected that longer storage times would bring about new results and observations. For future investigations on the colloidal stability of emulsified triacylglycerols, it would not only be interesting to prolong the evaluation period but also to study the effect of non-isothermal storage conditions with peak temperatures exceeding the melting range of the disperse fat phase. This would more realistically reflect the conditions under which products are being stored and distributed and would thus allow for a better transferability of the study results.

Spray-drying of emulsion based products such as infant formulae, instant dairy powders or compressible pharmaceutical excipients (e.g., lactose and dextrose) is commonly used to prolong the products' shelf life, to save shipping costs and, in the case of pharmaceuticals, to facilitate the tableting process. That is because the volume of the continuous phase is significantly reduced by evaporation. Powders are subjected to a set of colloidal instability mechanisms not found in liquid emulsions, i.e. plasticisation and caking. In dairy powders, the tendency of lactose to undergo recrystallisation poses an additional challenge to preserve product quality (especially redispersibility). Combining macromolecular and low molecular weight emulsifiers to stabilise emulsion interfaces has been shown to be effective in both liquid and spray-dried systems. It might therefore be a valid approach to transfer the study design of this project to spray-dried emulsions and to investigate whether the cooling rate or the addition of phospholipids have an effect on the physical and chemical stability of powdered emulsified triacylglycerols.

This project focused on emulsified triacylglycerols with a fully saturated fatty acid profile. TAGs composed of saturated FAs have a higher melting point and are therefore easier to crystallise as compared to TAGs with more unsaturated FA chains. From a nutritional perspective, saturated fats are however highly unfavourable. As the findings of this project are intended to benefit not only the cosmetics and pharmaceutical industry but also the food industry, there is a clear need to perform investigations on the colloidal stability and crystallisation behaviour of emulsion based foods with a more unsaturated fat phase.

7 References

- Abramov, S., Berndt, A., Georgieva, K., Ruppik, P. & Schuchmann, H. P., 2017. Investigation of the influence of mean droplet size and shear rate on crystallization behavior of hexadecane-in-water dispersions. *Colloids and Surfaces*, 529, p.513-522. DOI: 10.1016/j.colsurfa.2017.06.029.
- Abramov, S., Shah, K., Weißenstein, L. & Karbstein, H. P., 2018. Effect of Alkane Chain Length on Crystallization in Emulsions during Supercooling in Quiescent Systems and under Mechanical Stress. *Processes*, 6. DOI: 10.3390/pr6010006.
- Akimov, S. A., Polynkin, M. A., Jiménez-Munguía, I., Pavlov, K. V. & Batishchev, O. V., 2018. Phosphatidylcholine Membrane Fusion Is pH-Dependent. *International Journal of Molecular Sciences*, 19. DOI: 10.3390/ijms19051358.
- Awad, T. S., Helgason, T., Kristbergsson, K., Decker, E. A., Weiss, J. & McClements, D. J., 2008. Effect of Cooling and Heating Rates on Polymorphic Transformations and Gelation of Tripalmitin Solid Lipid Nanoparticle (SLN) Suspensions. *Food Biophysics*, 3, p.155-162. DOI: 10.1007/s11483-008-9057-8.
- Bayard, M., Cansella, M. & Leal-Calderon, F., 2022. Crystallization of emulsified anhydrous milk fat: The role of confinement and of minor compounds. A DSC study. *Food Chemistry*, 373. DOI: 10.1016/j.foodchem.2021.131605.
- Bergenståhl, B. & Alander, J., 1997. Lipids and colloidal stability. *Current Opinion in Colloid & Interface Science.*, 2, p.590-595. DOI: 10.1016/S1359-0294(97)80050-7.
- Bhattacharjee, S., 2016. DLS and zeta potential – What they are and what they are not? *Journal of Controlled Release*, 235, p.337-351. DOI: 10.1016/j.jconrel.2016.06.017.
- Bos, M. A. & van Vliet, T., 2001. Interfacial rheological properties of adsorbed protein layers and surfactants: a review. *Advances in Colloid and Interface Science*, 91, p.437-471. DOI: 10.1016/S0001-8686(00)00077-4.
- Bund, R. K. & Hartel, R. W., 2010. Crystallization in foods and food quality deterioration. In: Skibsted, L. H., Risbo, J. & Andersen, M. L. (eds.) *Chemical deterioration and physical instability of food and beverages*. Cambridge: Woodhead Publishing. DOI: 10.1533/9781845699260.frontmatter.
- Bunjes, H. & Koch, M. H. J., 2005. Saturated phospholipids promote crystallization but slow down polymorphic transitions in triglyceride nanoparticles. *Journal of Controlled Release*, 107, p.229-243. DOI: 10.1016/j.jconrel.2005.06.004.
- Bunjes, H., Steiniger, F. & Richter, W., 2007. Visualizing the Structure of Triglyceride Nanoparticles in Different Crystal Modifications. *Langmuir*, 23, p.4005-4011. DOI: 10.1021/la062904p.
- Bylaite, E., Nylander, T., Venskutonis, R. & Joensson, B., 2000. Emulsification of caraway essential oil in water by lecithin and β -lactoglobulin: emulsion stability and properties of the formed oil-aqueous interface. *Colloids and Surfaces*, 20, p.327-340. DOI: 10.1016/S0927-7765(00)00212-5.
- Bylund, G., 1995. *Tetra Pak Dairy Processing Handbook*. Lund: Tetra Pak Processing Systems AB.
- Calligarisa, G. A., da Silvab, T. L. T., Ribeirob, A. P. B., dos Santosc, A. O. & Cardoso, L. P., 2018. On the quantitative phase analysis and amorphous content of triacylglycerols materials by X-ray Rietveld method. *Chemistry and Physics of Lipids*, 212, p.51-60. DOI: 10.1016/j.chemphyslip.2018.01.003.
- Contarini, G. & Povolo, M., 2013. Phospholipids in Milk Fat: Composition, Biological and Technological Significance, and Analytical Strategies. *International Journal of Molecular Sciences*, 13. DOI: 10.3390/ijms14022808.
- Coulter, T. P., 2002. *FOOD The Chemistry of Its Components*. 4 ed. Cambridge: The Royal Society of Chemistry. DOI: 10.1039/9781847550903.

- Coupland, J. N., 2002. Crystallization in emulsions. *Current Opinion in Colloid and Interface Science*, 7, p.445-450. DOI: 10.1016/S1359-0294(02)00080-8.
- Darling, D. F. & Birkett, R. J., 1986. Food Colloids in Practice. In: Dickinson, E. (ed.) *Food Emulsions and Foams*. Cambridge: Woodhead.
- Federal Ministry of Food and Agriculture, 2020. *Understanding Farming. Facts and figures about German farming* [Online]. Available: https://www.bmel.de/SharedDocs/Downloads/EN/Publications/UnderstandingFarming.pdf?__blob=publicationFile [Accessed 19-08-2022].
- Food & Agriculture Organization of the United Nations, 2011. *Global food losses and food waste - Extent, cause and prevention*. Rome: Food & Agriculture Organization of the United Nations. DOI: 9789251072059.
- Friberg, S. E., 1997. Emulsion stability. In: Friberg, S. E. & Larsson, K. (eds.) *Food Emulsions*. 3 ed. New York: Marcel Dekker. DOI: 10.1080/01932699808956238.
- Golodnizky, D., Shmidov, Y., Bitton, R., Bernardes, C. E. S. & Davidovich-Pinhas, M., 2022. Isotropic liquid state of triacylglycerols. *Journal of Molecular Liquids*, 353. DOI: 10.1016/j.molliq.2022.118703.
- Goodwin, J. W., 2004. *Colloids and Interfaces with Surfactants and Polymers – An Introduction*. Chichester: John Wiley & Sons Ltd.
- Handa, T., Saito, H. & Miyajima, K., 1990. Phospholipid monolayers at the triolein-saline interface: production of microemulsion particles and conversion of monolayers to bilayers. *Biochemistry*, 29, p.2884-2890. DOI: 10.1021/bi00463a034.
- Hartel, R. W., 2001. Crystallization in foods. In: Myerson, A. S. (ed.) *Handbook of Industrial Crystallization*. 2 ed. Woburn: Butterworth-Heinemann. DOI: 10.1016/B978-0-7506-7012-8.X5000-9.
- Heiden-Hecht, T., Taboada, M. L., Brückner-Gühmann, M., Karbstein, H. P., Gaukel, V. & Druscha, S., 2021. Towards an improved understanding of spray-dried emulsions: Impact of the emulsifying constituent combination on characteristics and storage stability. *International Dairy Journal*, 121. DOI: 10.1016/j.idairyj.2021.105134.
- Heiden-Hecht, T. & Drusch, S., 2022. Impact of Saturation of Fatty Acids of Phosphatidylcholine and Oil Phase on Properties of β -Lactoglobulin at the Oil/Water Interface. *Food Biophysics*, 17, p.171-180. DOI: 10.1007/s11483-021-09705-8.
- Hernqvist, L., 1986. Polar Lipids in Emulsions and Microemulsions. In: Dickinson, E. (ed.) *Food Emulsions and Foams*. Cambridge: Woodhead.
- Huppertz, T. & Gazi, I., 2016. Lactose in dairy ingredients: Effect on processing and storage stability. *Journal of Dairy Science*, 99, p.6842-6851. DOI: 10.3168/jds.2015-10033.
- Lebouin, C., Olivier, Y. S., Sibert, E., Millet, P., Maret, M. & Faure, R., 2009. Electrochemically elaborated palladium nanofilms on Pt(1 1 1): Characterization and hydrogen insertion study. *Journal of Electroanalytical Chemistry*, 626, p.59-65. DOI: 10.1016/j.jelechem.2008.11.005.
- Logan, A., Lopez, C., Xu, M., Day, L., Oiseth, S. & Augustin, M. A., 2021. Tempering governs the milk fat crystallisation and viscoelastic behaviour of unprocessed and homogenised creams. *Food Research International*, 147. DOI: 10.1016/j.foodres.2021.110557.
- Macej, O. D., Jovanovic, S. T. & Djurdjevic, J. D. D., 2002. The Influence of High Temperatures on Milk Proteins. *Hemijaska Industrija*, 56, p.123-132. DOI: 10.2298/HEMINDO203123M.
- Mazzanti, G., Guthrie, S. E., Sirota, E. B., Marangoni, A. G. & Idziak, S. H. J., 2004. Effect of Minor Components and Temperature Profiles on Polymorphism in Milk Fat. *Crystal Growth & Design*, 4, p.1303-1309. DOI: 10.1021/cg0497602.
- McClements, D. J., 2012. Crystals and crystallization in oil-in-water emulsions: Implications for emulsion-based delivery systems. *Advances in Colloid and Interface Science*, 74, p.1-30. DOI: 10.1016/j.cis.2012.03.002.

- McClements, D. J., Dickinson, E., Dungan, S. R., Kinsella, J. E., Ma, J. G. & Povey, M. J. W., 1993a. Effect of Emulsifier Type on the Crystallization Kinetics of Oil-in-Water Emulsions Containing a Mixture of Solid and Liquid Droplets. *Journal of Colloid and Interface Science*, *160*, p.293-297. DOI: 10.1006/jcis.1993.1399.
- McClements, D. J., Dungan, S. R., German, J. B. & Kinsella, J. E., 1993b. Factors which affect oil exchange between oil-in-water emulsion droplets stabilized by whey protein isolate: protein concentration, droplet size and ethanol. *Colloids and Surfaces*, *81*, p.203-210. DOI: 10.1016/0927-7757(93)80247-C.
- McClements, D. J., Dungan, S. R., German, J. B., Simoneau, C. & Kinsella, J. E., 1993c. Droplet size and emulsifier type affect crystallization and melting of hydrocarbon-in-water emulsions. *Journal of Food Science*, *58*, p.1148-1151. DOI: 10.1111/j.1365-2621.1993.tb06135.
- Mehnert, W. & Mäder, K., 2001. Solid lipid nanoparticles: Production, characterization and applications. *Advanced Drug Delivery Reviews*, *47*, p.165-196. DOI: 10.1016/S0169-409X(01)00105-3.
- Merkus, H. G., 2009. *Particle Size Measurements. Fundamentals, Practice, Quality*. Dordrecht: Springer. DOI: 10.1007/978-1-4020-9016-5.
- Motoyama, M., Adno, M., Sasak, K. & Hamaguchi, H., 2010. Differentiation of Animal Fats from Different Origins: Use of Polymorphic Features Detected by Raman Spectroscopy. *Society for Applied Spectroscopy*, *64*, p.1244-1250. DOI: 10.1366/000370210793335070.
- Murphy, D. B. & Davidson, M. W., 2013. *Fundamentals of Light Microscopy and Electronic Imaging*. 2 ed. Hoboken: John Wiley & Sons Inc.
- Nakayama, H. & Hayashi, A., 2014. Mixing Acid Salts and Layered Double Hydroxides in Nanoscale under Solid Condition. *Pharmaceutics*, *6*, p.436-446. DOI: 10.3390/pharmaceutics6030436.
- O'Mahony, J. A. & Fox, P. F., 2014. Milk: An Overview. In: Singh, H., Thompson, A. & Boland, M. (eds.) *Milk Proteins*. 2 ed. London: Academic Press. DOI: 10.1016/B978-0-12-405171-3.00002-7.
- Pang, S., Ma, C., Zhang, N. & He, L., 2015. Investigation of the solubility enhancement mechanism of rebudioside D using a solid dispersion technique with potassium sorbate as a carrier. *Food Chemistry*, *174*, p.564-570. DOI: 10.1016/j.foodchem.2014.11.113.
- Pashley, R. M. & Karaman, M. E., 2004. *Applied Colloid and Surface Chemistry*. Chichester: John Wiley & Sons Ltd.
- Perkin Elmer Inc., 2013. *Differential Scanning Calorimetry (DSC). A Beginner's Guide. 20 Common Questions about DSC* [Online]. Available: https://resources.perkinelmer.com/lab-solutions/resources/docs/GDE_DSCBeginnersGuide.pdf?_ga=2.165224251.507400118.1651948512-41798240.1651948512 [Accessed 08-05-2022].
- Pichot, R., Watson, R. L. & Norton, I. T., 2013. Phospholipids at the Interface: Current Trends and Challenges. *International Journal of Molecular Sciences*, *14*, p.11767-11794. DOI: 10.3390/ijms140611767.
- Rabelo, R. S., Oliveira, I. F., da Silva, V. M., Prata, A. S. & Hubinger, M. D., 2018. Chitosan coated nanostructured lipid carriers (NLCs) for loading Vitamin D: A physical stability study. *International Journal of Biological Macromolecules*, *119*, p.902-912. DOI: 10.1016/j.ijbiomac.2018.07.174.
- Rayner, M., 2015. Current status on novel ways for stabilizing food dispersions by oleosins, particles and microgels. *Current Opinion in Food Science*, *3*, p.94-109. DOI: 10.1016/j.cofs.2015.05.006.
- Reiner, J., Ly, T. T., Liu, L. & Karbstein, H. P., 2022. Melt emulsions: Influence of the Cooling Procedure on Crystallization and Recrystallization of Emulsion Droplets and their Influence on Dispersion Viscosity upon Storage. *Chemie Ingenieur Technik*, *94*, p.356-364. DOI: 10.1002/cite.202100143.
- Relkin, P., Sourdet, S. & Fosseux, P.-Y., 2003. Fat Crystallization in Complex Food Emulsions. Effects of adsorbed milk proteins and of whipping process. *Journal of Thermal Analysis and Calorimetry*, *71*, p.187-195. DOI: 10.1023/A:1022282720983.

- Ritzoulis, C., 2013. *Introduction to the Physical Chemistry of Foods*. Boca Raton: CRC Press. DOI: 10.1201/b14705.
- Romo-Urbe, A., 2022. Wide-angle X-ray diffraction and small-angle X-ray scattering studies of elastomer blends and composites. In: Rangappa, S. M., Siengchin, S., Parameswaranpillai, J. & Ozbakkaloglu, T. (eds.) *Elastomer Blends and Composites: Principles, Characterization, Advances and Applications*. Netherlands: Elsevier. DOI: 10.1016/C2020-0-01558-6.
- Roos, Y. & Drusch, S., 2016. *Phase Transitions in Foods*. 2 ed. Waltham: Academic Press. DOI: 10.1016/B978-0-12-408086-7.00002-4.
- Rousseau, D., 2000. Fat crystals and emulsion stability - a review. *Food Research International*, 33, p.3-14. DOI: 10.1016/S0963-9969(00)00017.
- Salminen, H., Helgason, T., Aulbach, S., Kristinsson, B., Kristbergsson, K. & Weiss, J., 2014. Influence of co-surfactants on crystallization and stability of solid lipid nanoparticles. *Journal of Colloid and Interface Science*. DOI: 10.1016/j.jcis.2014.04.009.
- Samtlebe, M., Yucel, U., Weiss, J. & Coupland, J. N., 2012. Stability of Solid Lipid Nanoparticles in the Presence of Liquid Oil Emulsions. *Journal of the American Oil Chemists' Society*, 89, p.609-617. DOI: 10.1007/s11746-011-1944-3.
- Saraiva, A., Carrascosa, C., Raheem, D., Ramos, F. & Raposo, A., 2020. Natural Sweeteners: The Relevance of Food Naturalness for Consumers, Food Security Aspects, Sustainability and Health Impacts. *International Journal of Environmental Research and Public Health*, 17. DOI: 10.3390/ijerph17176285.
- Schestkova, H., Drusch, S. & Wagemans, A. M., 2020. FTIR analysis of β -lactoglobulin at the oil/water-interface. *Food Chemistry*, 302. DOI: 10.1016/j.foodchem.2019.125349.
- Shchipunov, Y. A. & Kolpakov, A. F., 1991. Phospholipids at the oil/water interface: adsorption and interfacial phenomena in an electric field. *Advances in Colloid and Interface Science*, 35, p.31-138. DOI: 10.1016/0001-8686(91)80020-k.
- Shirokanev, A. S., Kirsh, D. V. & Kupriyanov, A. V., 2019. The study of effectiveness of a high-performance crystal lattice parametric identification algorithm based on CUDA technology. *Journal of Physics: Conference Series*. DOI: 10.1088/1742-6596/1368/5/052040.
- Singh, P. R. & Heldman, D. R., 2014. *Introduction to Food Engineering*. 5 ed. London: Elsevier. DOI: 10.1016/B978-0-12-398530-9.00017-6.
- Speakman, S. A., n.d. *Basics of X-Ray Powder Diffraction. Training to Become an Independent User of the X-Ray SEF at the Center for Materials Science and Engineering at MIT*. [Online]. Available: <http://prism.mit.edu/xray> [Accessed 12-08-2022].
- Taboada, M. L., Leister, N., Karbstein, H. P. & Gaukel, V., 2020. Influence of the Emulsifier System on Breakup and Coalescence of Oil Droplets during Atomization of Oil-In-Water Emulsions. *ChemEngineering*, 47. DOI: 10.3390/chemengineering4030047.
- Tanner, D. & Amos, N., 2003. Temperature variability during shipment of fresh produce. *Acta Horticulturae*, 599, p.193-203. DOI: 10.17660/ActaHortic.2003.599.22.
- Tian, C. & Chius, C., 2018. Importance of Hydrophilic Groups on Modulating the Structural, Mechanical, and Interfacial Properties of Bilayers: A Comparative Molecular Dynamics Study of Phosphatidylcholine and Ion Pair Amphiphile Membranes. *International Journal of Molecular Sciences*, 1552. DOI: 10.3390/ijms19061552.
- Truong, T., Bansal, N., Sharma, R., Palmer, M. & Bhandari, B., 2014. Effects of emulsion droplet sizes on the crystallisation of milk fat. *Food Chemistry*, 145, p.725-735. DOI: 10.1016/j.foodchem.2013.08.072.
- Truong, T., Palmer, M., Bansal, N. & Bhandari, B., 2016. *Effect of Milk Fat Globule Size on the Physical Functionality of Dairy Products*. Cham: Springer. DOI: 10.1007/978-3-319-23877-7.
- Ueno, S., Nishida, T. & Sato, K., 2008. Synchrotron Radiation Microbeam X-ray Analysis of Microstructures and the Polymorphic Transformation of Spherulite Crystals of Trilaurin. *Crystal Growth & Design*, 8, p.751-754. DOI: 10.1021/cg0706159.

- Vanapalli, S. & Palanuwech, J., 2022. Stability of emulsions to dispersed phase crystallization: Effect of oil type, dispersed phase volume fraction, and cooling rate. *Colloids and Surfaces. A: Physicochemical and Engineering Aspects*, 204, p.227-237. DOI: 10.1016/S0927-7757(01)01135-9.
- Walstra, P. & van Beresteyn, E. C. H., 1975. Crystallization of milk fat in the emulsified state. *Netherlands Milk and Dairy Journal*, 29, p.35-65.
- Weiss, J. & McClements, D. J., 2000. Mass Transport Phenomena in Oil-in-Water Emulsions Containing Surfactant Micelles: Solubilization. *Langmuir*, 16, p.5879-5883. DOI: 10.1021/la9914763.
- Westesen, K. & Siekmann, B., 1997. Investigation of the gel formation of phospholipid-stabilized solid lipid nanoparticles. *International Journal of Pharmaceutics*. DOI: 10.1016/S0378-5173(97)04890-4.
- Wissing, S. A., Kayser, O. & Müller, R. H., 2003. Solid lipid nanoparticles for parenteral drug delivery. *Advanced Drug Delivery Reviews*, 56, p.1257-1272. DOI: 10.1016/j.addr.2003.12.002.
- Wright, A. J. & Marangoni, A. G., 2006. Crystallization and Rheological Properties of Milk Fat. In: Fox, P. F. & McSweeney, P. L. H. (eds.) *Advanced Dairy Chemistry. Volume 2 Lipids*. 3 ed. New York: Springer Science. DOI: 10.1007/0-387-28813-9_7.
- Zéberg-Mikkelsen, C. K. & Stenby, E. H., 1999. Predicting the melting points and the enthalpies of fusion of saturated triglycerides by a group contribution method. *Fluid Phase Equilibria*, 162, p.7-17. DOI: 10.1016/S0378-3812(99)00171-5.
- Zhang, N., Liu, C., Jin, L., Zhang, R., Siebert, H.-C., Wang, Z., Prakash, S., Yin, X., Li, J., Hou, D., Sun, B. & Liu, M., 2020. Influence of Long-Chain/Medium-Chain Triglycerides and Whey Protein/Tween 80 Ratio on the Stability of Phosphatidylserine Emulsions (O/W). *American Chemical Society Omega*, 5, p.7792-7801. DOI: 10.1021/acsomega.9b03702.

8 Appendix

Figure 8-1 Images of B samples cooled at low, moderate and high rate, taken at t_0 , t_2 , t_4 , t_8 (left to right respectively).....	XX
Figure 8-2 Images of C samples cooled at low, moderate and high rate, taken at t_0 , t_2 , t_4 , t_8 (left to right respectively).....	XX
Figure 8-3 Images of CC samples cooled at low, moderate and high rate, taken at t_0 , t_2 , t_4 , t_8 (left to right respectively).....	XX
Figure 8-4 Images of E samples cooled at low, moderate and high rate, taken at t_0 , t_2 , t_4 , t_8 (left to right respectively).....	XX
Figure 8-5 Images of EE samples cooled at low, moderate and high rate, taken at t_0 , t_2 , t_4 , t_8 (left to right respectively).....	XX
Figure 8-6 Creaming index of the B, C and CC samples at t_0 , t_2 , t_4 and t_8 as computed according to Equation 4-3. Data are averaged ($N = 2$, $n = 1$) and shown with their respective SEM.	XXI
Figure 8-7 Creaming index of the B, E and EE samples at t_0 , t_2 , t_4 and t_8 as computed according to Equation 4-3. Data are averaged ($N = 2$, $n = 1$) and shown with their respective SEM.	XXI
Figure 8-8 Q3 distribution of the B samples measured by laser diffraction analysis at t_0 , t_4 and t_8 (from left to right). Data are averaged ($N = 2$, $n = 3$) and shown with their respective SEM.	XXII
Figure 8-9 Q3 distribution of the C samples measured by laser diffraction analysis at t_0 , t_4 and t_8 (from left to right). Data are averaged ($N = 2$, $n = 3$) and shown with their respective SEM.	XXIII
Figure 8-10 Q3 distribution of the CC samples measured by laser diffraction analysis at t_0 , t_4 and t_8 (from left to right). Data are averaged ($N = 2$, $n = 3$) and shown with their respective SEM.	XXIV
Figure 8-11 Q3 distribution of the E samples measured by laser diffraction analysis at t_0 , t_4 and t_8 (from left to right). Data are averaged ($N = 2$, $n = 3$) and shown with their respective SEM.	XXV
Figure 8-12 Q3 distribution of the EE samples measured by laser diffraction analysis at t_0 , t_4 and t_8 (from left to right). Data are averaged ($N = 2$, $n = 3$) and shown with their respective SEM.	XXVI
Figure 8-13 DSC curve of the B sample replicates ($N = 2$) crystallised at a low cooling rate (RT). Melting point determined at t_0 by heating from 20 °C to 70 °C with 2.5 Kmin ⁻¹ (endo up).....	XXVIII
Figure 8-14 DSC curve of the B sample replicates ($N = 2$) crystallised at a low cooling rate (RT). Melting point determined at t_8 by heating from 20 °C to 70 °C with 2.5 Kmin ⁻¹ (endo up).....	XXVIII
Figure 8-15 DSC curve of the B sample replicates ($N = 2$) crystallised at a moderate cooling rate (RF). Melting point determined at t_0 by heating from 20 °C to 70 °C with 2.5 Kmin ⁻¹ (endo up).	XXVIII
Figure 8-16 DSC curve of the B sample replicates ($N = 2$) crystallised at a moderate cooling rate (RF). Melting point determined at t_8 by heating from 20 °C to 70 °C with 2.5 Kmin ⁻¹ (endo up).	XXIX
Figure 8-17 DSC curve of the B sample replicates ($N = 2$) crystallised at a high cooling rate (IB). Melting point determined at t_0 by heating from 20 °C to 70 °C with 2.5 Kmin ⁻¹ (endo up).....	XXIX
Figure 8-18 DSC curve of the B sample replicates ($N = 2$) crystallised at a high cooling rate (IB). Melting point determined at t_8 by heating from 20 °C to 70 °C with 2.5 Kmin ⁻¹ (endo up).....	XXIX

Figure 8-19 DSC curve of the C sample replicates (N = 2) crystallised at a low cooling rate (RT). Melting point determined at t_0 by heating from 20 °C to 70 °C with 2.5 Kmin ⁻¹ (endo up).....	XXX
Figure 8-20 DSC curve of the C sample replicates (N = 2) crystallised at a low cooling rate (RT). Melting point determined at t_8 by heating from 20 °C to 70 °C with 2.5 Kmin ⁻¹ (endo up).....	XXX
Figure 8-21 DSC curve of the C sample replicates (N = 2) crystallised at a moderate cooling rate (RF). Melting point determined at t_0 by heating from 20 °C to 70 °C with 2.5 Kmin ⁻¹ (endo up).	XXX
Figure 8-22 DSC curve of the C sample replicates (N = 2) crystallised at a moderate cooling rate (RF). Melting point determined at t_8 by heating from 20 °C to 70 °C with 2.5 Kmin ⁻¹ (endo up).	XXXI
Figure 8-23 DSC curve of the C sample replicates (N = 2) crystallised at a high cooling rate (IB). Melting point determined at t_0 by heating from 20 °C to 70 °C with 2.5 Kmin ⁻¹ (endo up).....	XXXI
Figure 8-24 DSC curve of the C sample replicates (N = 2) crystallised at a high cooling rate (IB). Melting point determined at t_8 by heating from 20 °C to 70 °C with 2.5 Kmin ⁻¹ (endo up).....	XXXI
Figure 8-25 DSC curve of the CC sample replicates (N = 2) crystallised at a low cooling rate (RT). Melting point determined at t_0 by heating from 20 °C to 70 °C with 2.5 Kmin ⁻¹ (endo up).....	XXXII
Figure 8-26 DSC curve of CC sample replicates (N = 2) crystallised at a low cooling rate (RT). Melting point determined at t_8 by heating from 20 °C to 70 °C with 2.5 Kmin ⁻¹ (endo up).....	XXXII
Figure 8-27 DSC curve of the CC sample replicates (N = 2) crystallised at a moderate cooling rate (RF). Melting point determined at t_0 by heating from 20 °C to 70 °C with 2.5 Kmin ⁻¹ (endo up).	XXXII
Figure 8-28 DSC curve of the CC sample replicates (N = 2) crystallised at a moderate cooling rate (RF). Melting point determined at t_8 by heating from 20 °C to 70 °C with 2.5 Kmin ⁻¹ (endo up).	XXXIII
Figure 8-29 DSC curve of the CC sample replicates (N = 2) crystallised at a high cooling rate (IB). Melting point determined at t_0 by heating from 20 °C to 70 °C with 2.5 Kmin ⁻¹ (endo up).....	XXXIII
Figure 8-30 DSC curve of the CC sample replicates (N = 2) crystallised at a high cooling rate (IB). Melting point determined at t_8 by heating from 20 °C to 70 °C with 2.5 Kmin ⁻¹ (endo up).....	XXXIII
Figure 8-31 DSC curve of the E sample replicates (N = 2) crystallised at a low cooling rate (RT). Melting point determined at t_0 by heating from 20 °C to 70 °C with 2.5 Kmin ⁻¹ (endo up).....	XXXIV
Figure 8-32 DSC curve of the E sample replicates (N = 2) crystallised at a low cooling rate (RT). Melting point determined at t_8 by heating from 20 °C to 70 °C with 2.5 Kmin ⁻¹ (endo up).....	XXXIV
Figure 8-33 DSC curve of the E sample replicates (N = 2) crystallised at a moderate cooling rate (RF). Melting point determined at t_0 by heating from 20 °C to 70 °C with 2.5 Kmin ⁻¹ (endo up).	XXXIV
Figure 8-34 DSC curve of the E sample replicates (N = 2) crystallised at a moderate cooling rate (RF). Melting point determined at t_8 by heating from 20 °C to 70 °C with 2.5 Kmin ⁻¹ (endo up).	XXXV
Figure 8-35 DSC curve of the E sample replicates (N = 2) crystallised at a high cooling rate (IB). Melting point determined at t_0 by heating from 20 °C to 70 °C with 2.5 Kmin ⁻¹ (endo up).....	XXXV
Figure 8-36 DSC curve of the E sample replicates (N = 2) crystallised at a high cooling rate (IB). Melting point determined at t_8 by heating from 20 °C to 70 °C with 2.5 Kmin ⁻¹ (endo up).....	XXXV
Figure 8-37 DSC curve of the EE sample replicates (N = 2) crystallised at a low cooling rate (RT). Melting point determined at t_0 by heating from 20 °C to 70 °C with 2.5 Kmin ⁻¹ (endo up).....	XXXVI

Figure 8-38 DSC curve of EE sample replicates (N = 2) crystallised at a low cooling rate (RT). Melting point determined at t_8 by heating from 20 °C to 70 °C with 2.5 Kmin ⁻¹ (endo up).....	XXXVI
Figure 8-39 DSC curve of the EE sample replicates (N = 2) crystallised at a moderate cooling rate (RF). Melting point determined at t_0 by heating from 20 °C to 70 °C with 2.5 Kmin ⁻¹ (endo up).	XXXVI
Figure 8-40 DSC curve of the EE sample replicates (N = 2) crystallised at a moderate cooling rate (RF). Melting point determined at t_8 by heating from 20 °C to 70 °C with 2.5 Kmin ⁻¹ (endo up).	XXXVII
Figure 8-41 DSC curve of the EE sample replicates (N = 2) crystallised at a high cooling rate (IB). Melting point determined at t_0 by heating from 20 °C to 70 °C with 2.5 Kmin ⁻¹ (endo up).....	XXXVII
Figure 8-42 DSC curve of the EE sample replicates (N = 2) crystallised at a high cooling rate (IB). Melting point determined at t_8 by heating from 20 °C to 70 °C with 2.5 Kmin ⁻¹ (endo up).....	XXXVII
Table 8-1 Span (dimensionless) of the cumulative normalised undersize distribution of all samples crystallised at slow cooling rate (RT). B samples serve as reference. Values are given as mean ± SEM, values marked with matching letters are significantly different according to one-way ANOVA with p = 0.05 (N = 2, n = 3).	XXVII
Table 8-2 Span (dimensionless) of the cumulative normalised undersize distribution of all samples crystallised at moderate cooling rate (RF). B samples serve as reference. Values are given as mean ± SEM, values marked with matching letters are significantly different according to one-way ANOVA with p = 0.05 (N = 2, n = 3).	XXVII
Table 8-3 Span (dimensionless) of the cumulative normalised undersize distribution of all samples crystallised at high cooling rate (IB). B-samples serve as reference. Values are given as mean ± SEM, values marked with matching letters are significantly different according to one-way ANOVA with p = 0.05 (N = 2, n = 3).	XXVII
Table 8-4 Span of the cumulative normalised undersize distribution of all B samples. Values are given as mean ± SEM, values marked with matching letters are significantly different according to one-way ANOVA with p = 0.05 (N = 2, n = 3).	XXVII
Table 8-5 Span(dimensionless) of the cumulative normalised undersize distribution of all C and CC samples. Values are given as mean ± SEM, values marked with matching letters are significantly different according to one-way ANOVA with p = 0.05 (N = 2, n = 3).	XXVII
Table 8-6 Span (dimensionless) of the cumulative normalised undersize distribution of all E and EE samples. Values are given as mean ± SEM, values marked with matching letters are significantly different according to one-way ANOVA with p = 0.05 (N = 2, n = 3).	XXVII

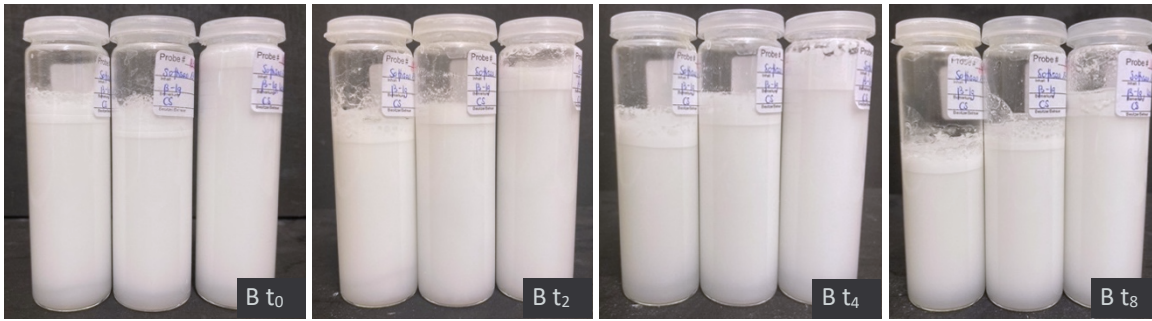


Figure 8-1 Images of B samples cooled at low, moderate and high rate, taken at t_0 , t_2 , t_4 , t_8 (left to right respectively).

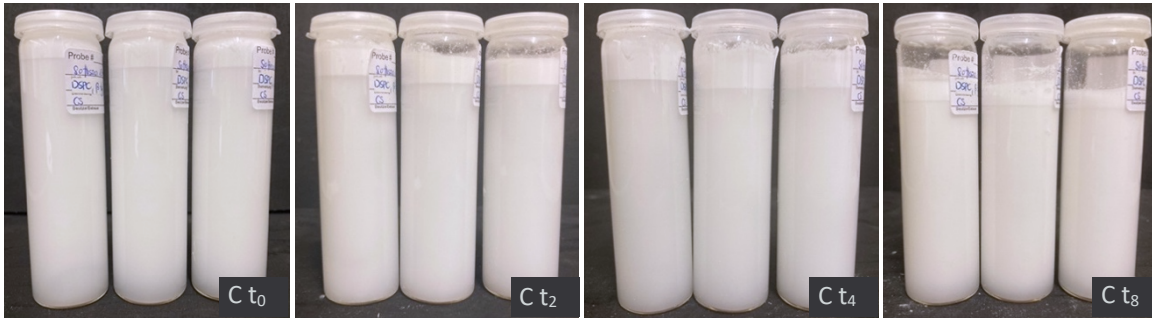


Figure 8-2 Images of C samples cooled at low, moderate and high rate, taken at t_0 , t_2 , t_4 , t_8 (left to right respectively).

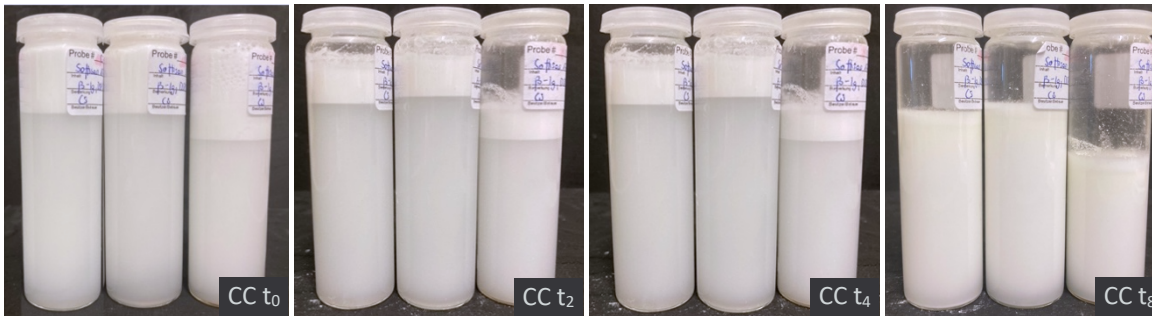


Figure 8-3 Images of CC samples cooled at low, moderate and high rate, taken at t_0 , t_2 , t_4 , t_8 (left to right respectively).

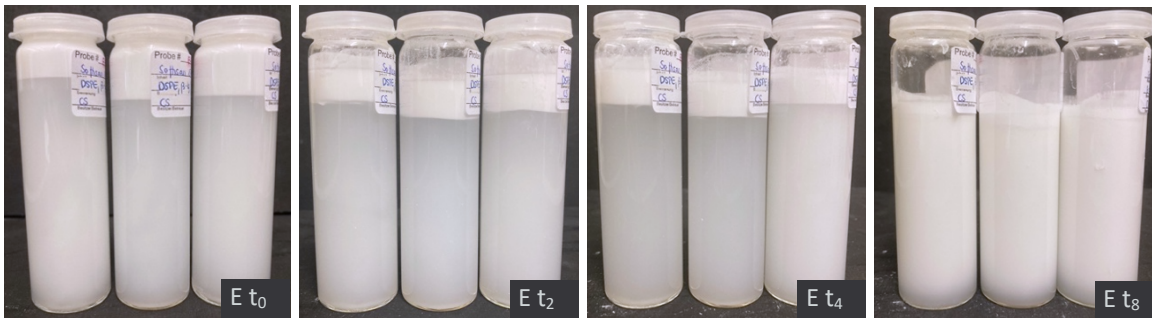


Figure 8-4 Images of E samples cooled at low, moderate and high rate, taken at t_0 , t_2 , t_4 , t_8 (left to right respectively).

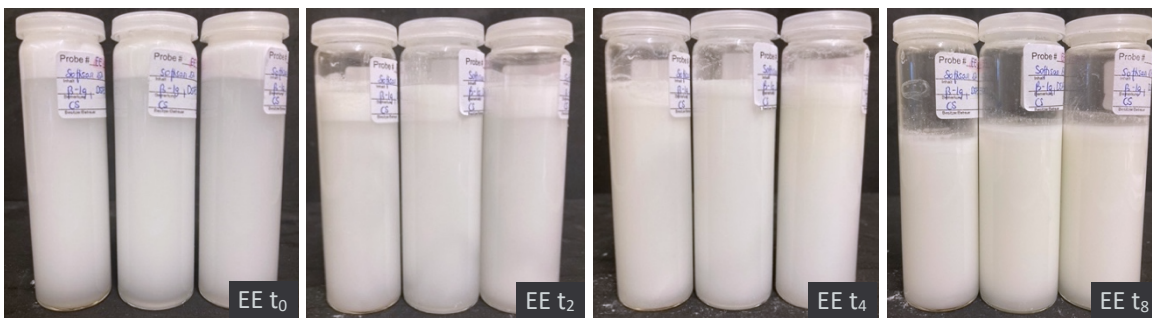


Figure 8-5 Images of EE samples cooled at low, moderate and high rate, taken at t_0 , t_2 , t_4 , t_8 (left to right respectively).

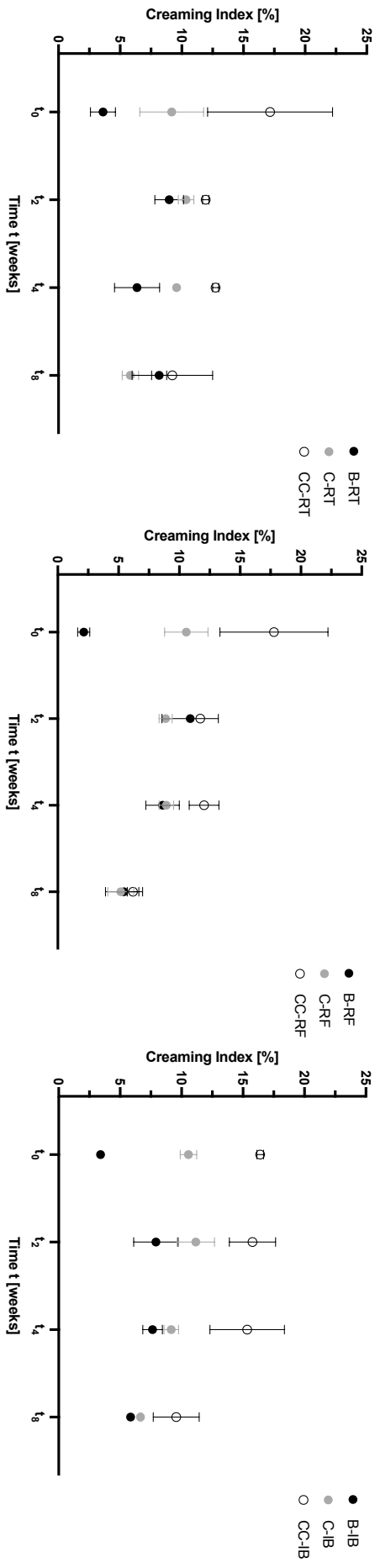


Figure 8-6 Creaming index of the B, C and CC samples at t_0 , t_2 , t_4 and t_8 as computed according to Equation 4-3. Data are averaged ($N = 2$, $n = 1$) and shown with their respective SEM.

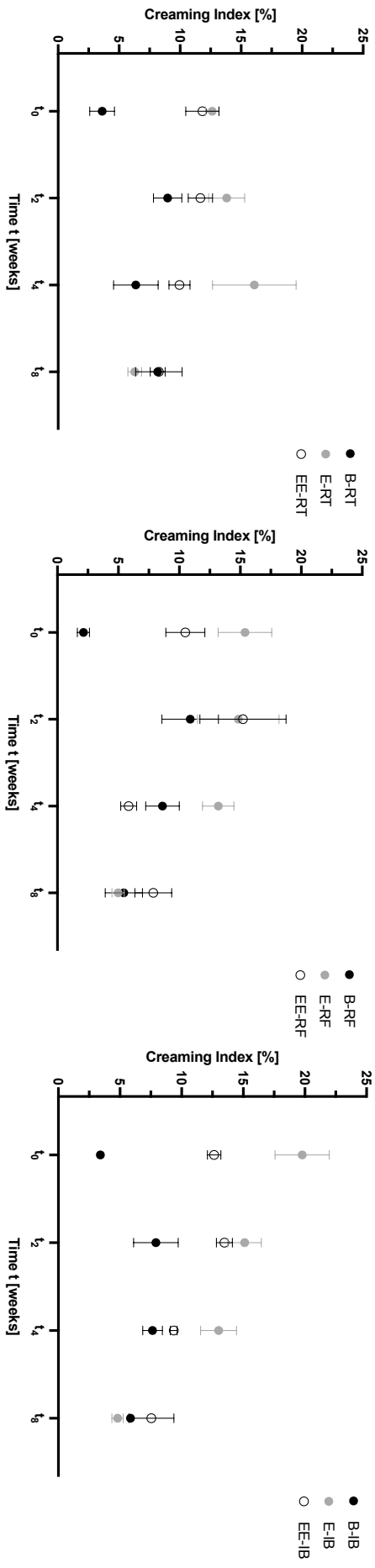


Figure 8-7 Creaming index of the B, E and EE samples at t_0 , t_2 , t_4 and t_8 as computed according to Equation 4-3. Data are averaged ($N = 2$, $n = 1$) and shown with their respective SEM.

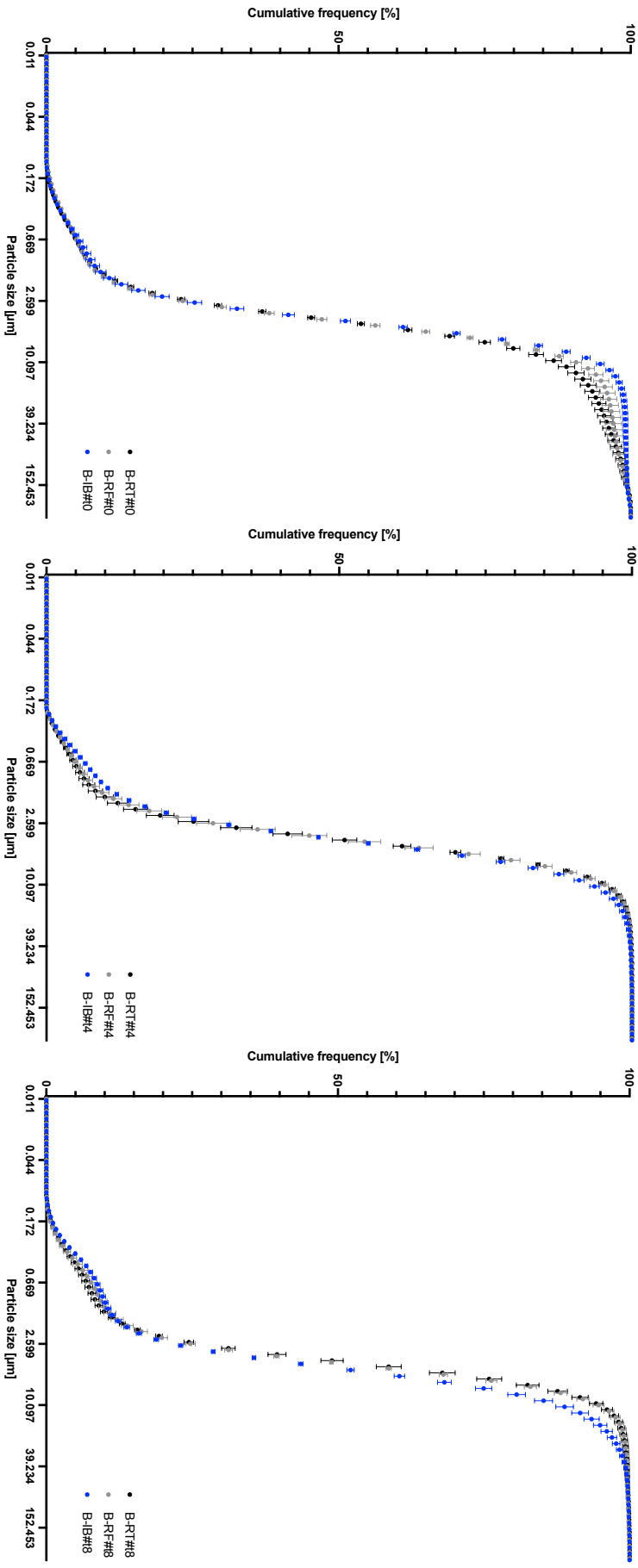


Figure 8-8 Q3 distribution of the B samples measured by laser diffraction analysis at t_0 , t_4 and t_8 (from left to right). Data are averaged ($N = 2$, $n = 3$) and shown with their respective SEM.

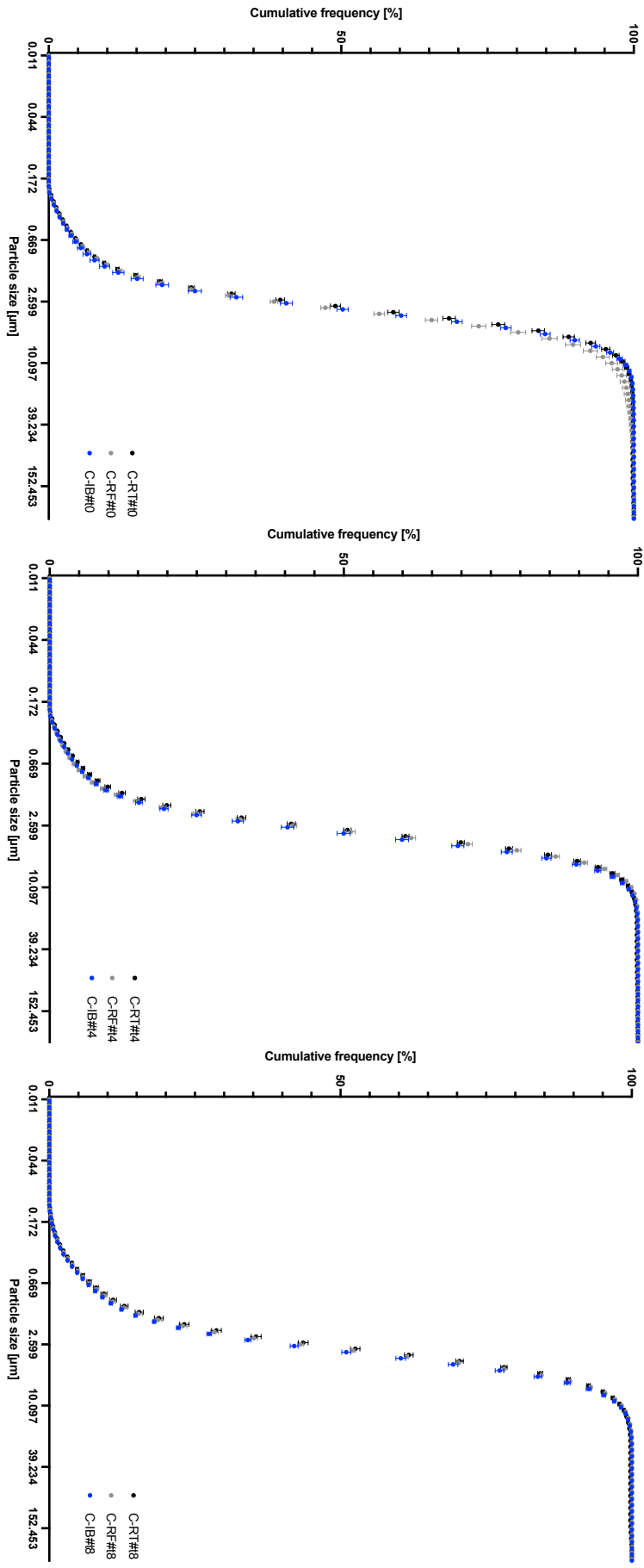


Figure 8-9 Q3 distribution of the C samples measured by laser diffraction analysis at t_0 , t_4 and t_8 (from left to right). Data are averaged ($N = 2$, $n = 3$) and shown with their respective SEM.

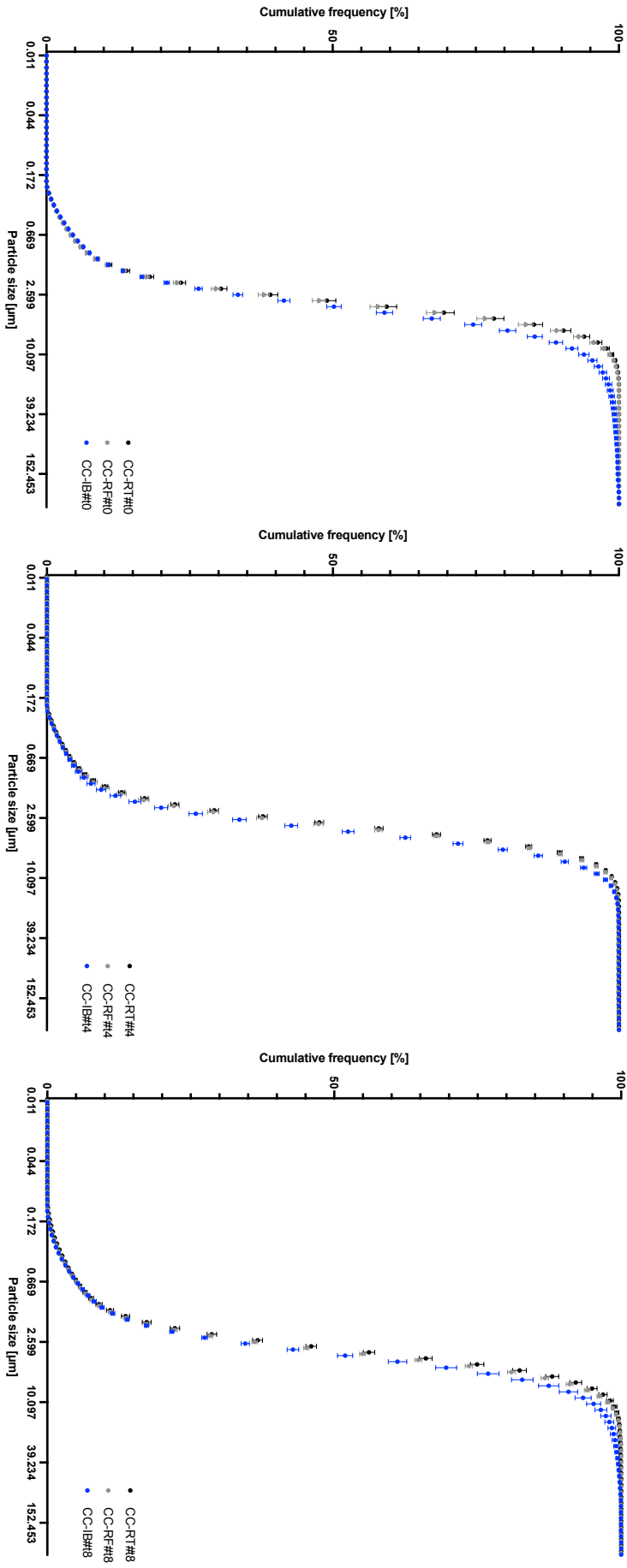


Figure 8-10 Q3 distribution of the CC samples measured by laser diffraction analysis at t_0 , t_4 and t_8 (from left to right). Data are averaged ($N = 2$, $n = 3$) and shown with their respective SEM.

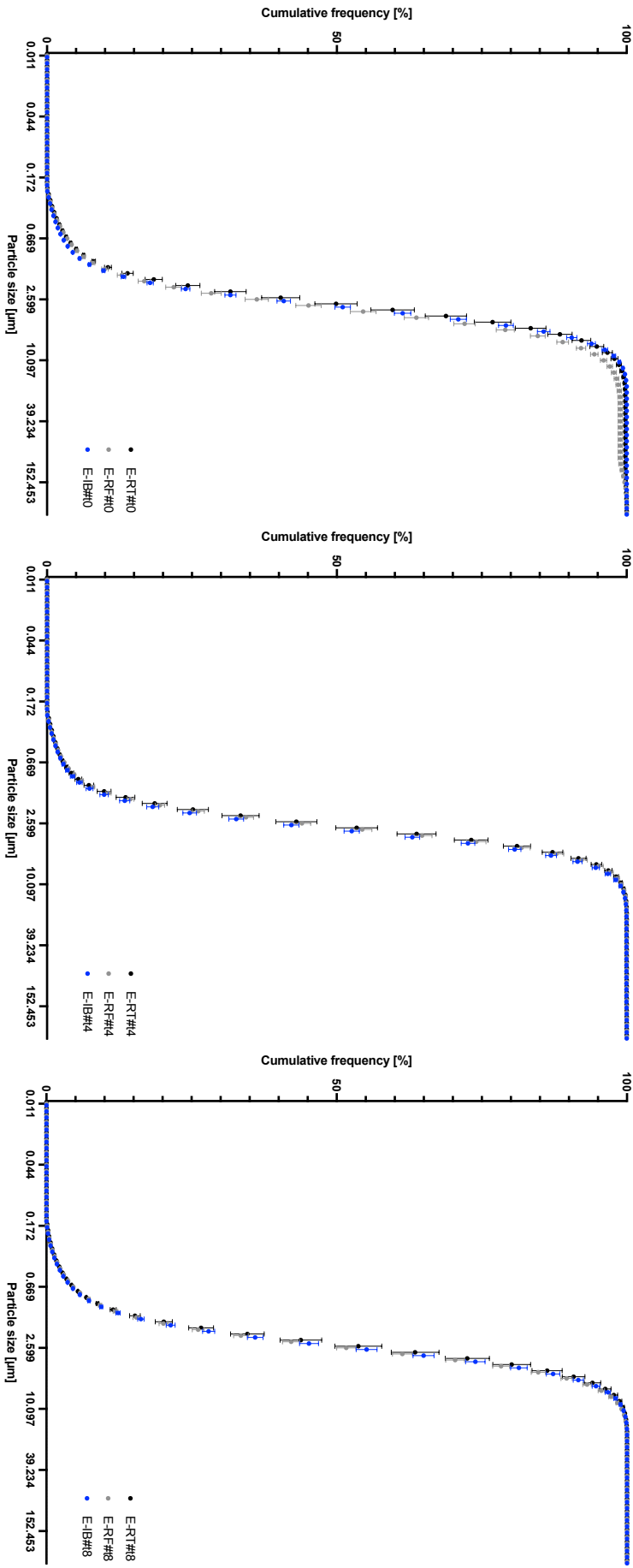


Figure 8-11 Q3 distribution of the E samples measured by laser diffraction analysis at t_0 , t_4 and t_8 (from left to right). Data are averaged ($N = 2$, $n = 3$) and shown with their respective SEM.

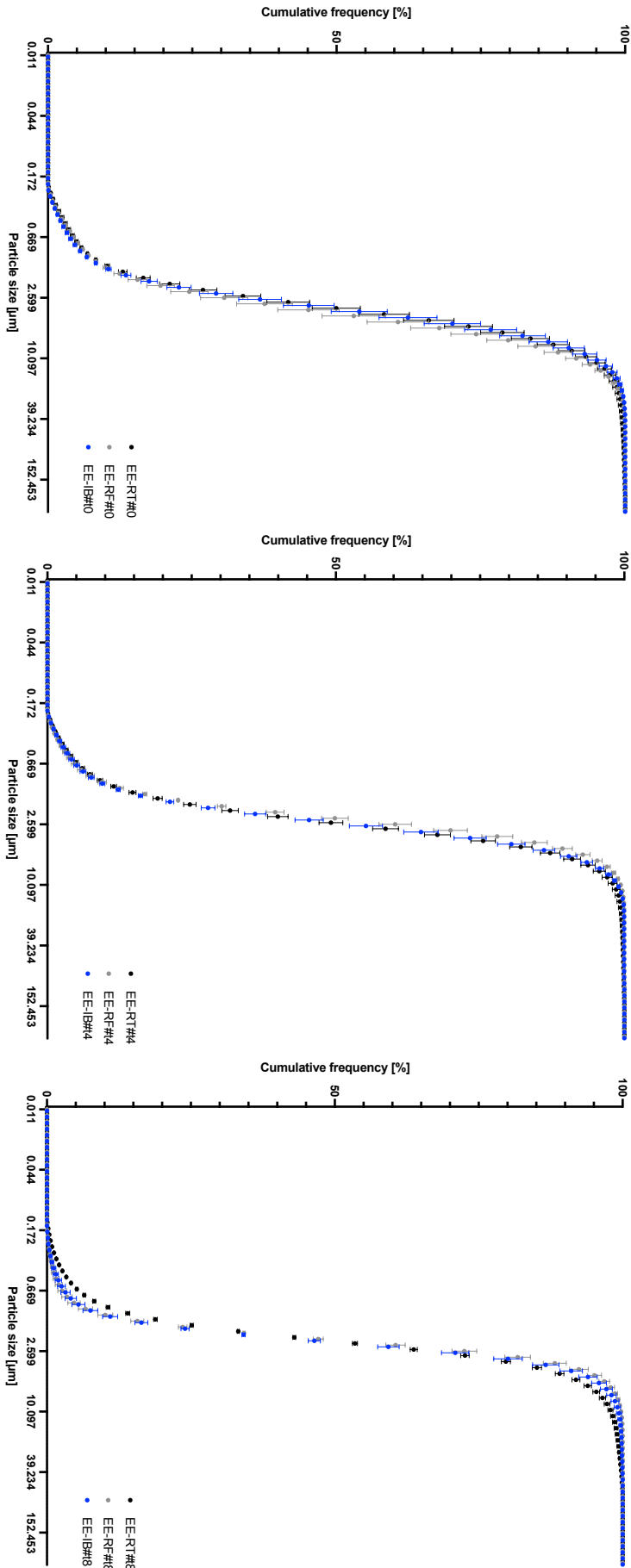


Figure 8-12 Q3 distribution of the EE samples measured by laser diffraction analysis at t_0 , t_4 and t_8 (from left to right). Data are averaged ($N = 2$, $n = 3$) and shown with their respective SEM.

Table 8-1 Span (dimensionless) of the cumulative normalised undersize distribution of all samples crystallised at slow cooling rate (RT). B samples serve as reference. Values are given as mean \pm SEM, values marked with matching letters are significantly different according to one-way ANOVA with $p = 0.05$ ($N = 2, n = 3$).

RT					
	B	C	CC	E	EE
t_0	2.8 ± 0.32^{abc}	1.7 ± 0.052^a	1.5 ± 0.053^b	1.6 ± 0.043^c	2.1 ± 0.14
t_4	1.7 ± 0.13	1.7 ± 0.044	1.5 ± 0.022	1.5 ± 0.038	1.8 ± 0.096
t_8	1.8 ± 0.087	1.8 ± 0.015	1.6 ± 0.070	1.5 ± 0.047	1.7 ± 0.070

Table 8-2 Span (dimensionless) of the cumulative normalised undersize distribution of all samples crystallised at moderate cooling rate (RF). B samples serve as reference. Values are given as mean \pm SEM, values marked with matching letters are significantly different according to one-way ANOVA with $p = 0.05$ ($N = 2, n = 3$).

RF					
	B	C	CC	E	EE
t_0	2.7 ± 0.35^{abcd}	1.9 ± 0.12^a	1.6 ± 0.048^b	1.8 ± 0.042^c	2.0 ± 0.091^d
t_4	1.8 ± 0.085	1.6 ± 0.028	1.5 ± 0.051	1.5 ± 0.034	1.5 ± 0.084
t_8	1.8 ± 0.096^e	1.8 ± 0.044	1.7 ± 0.042	1.6 ± 0.028	1.2 ± 0.10^e

Table 8-3 Span (dimensionless) of the cumulative normalised undersize distribution of all samples crystallised at high cooling rate (IB). B-samples serve as reference. Values are given as mean \pm SEM, values marked with matching letters are significantly different according to one-way ANOVA with $p = 0.05$ ($N = 2, n = 3$).

IB					
	B	C	CC	E	EE
t_0	1.7 ± 0.090	1.6 ± 0.053	2.0 ± 0.095	1.5 ± 0.030	1.9 ± 0.12
t_4	2.1 ± 0.090^{abcd}	1.6 ± 0.025^a	1.6 ± 0.057^b	1.5 ± 0.044^c	1.7 ± 0.063^d
t_8	2.3 ± 0.15^{efg}	1.8 ± 0.031^e	1.9 ± 0.13	1.6 ± 0.030^f	1.3 ± 0.14^g

Table 8-4 Span of the cumulative normalised undersize distribution of all B samples. Values are given as mean \pm SEM, values marked with matching letters are significantly different according to one-way ANOVA with $p = 0.05$ ($N = 2, n = 3$).

	B-RT	B-RF	B-IB
t_0	2.8 ± 0.32^{ab}	2.7 ± 0.35^{cd}	1.7 ± 0.090^e
t_4	1.7 ± 0.13^a	1.8 ± 0.085^c	2.1 ± 0.090
t_8	1.8 ± 0.087^b	1.8 ± 0.096^d	2.3 ± 0.15^e

Table 8-5 Span(dimensionless) of the cumulative normalised undersize distribution of all C and CC samples. Values are given as mean \pm SEM, values marked with matching letters are significantly different according to one-way ANOVA with $p = 0.05$ ($N = 2, n = 3$).

	C-RT	C-RF	C-IB	CC-RT	CC-RF	CC-IB
t_0	1.7 ± 0.052	1.9 ± 0.12	1.6 ± 0.053	1.5 ± 0.053	1.6 ± 0.048	2.0 ± 0.095
t_4	1.7 ± 0.044	1.6 ± 0.028	1.6 ± 0.025	1.5 ± 0.022	1.5 ± 0.051	1.6 ± 0.057
t_8	1.8 ± 0.015	1.8 ± 0.044	1.8 ± 0.031^e	1.6 ± 0.070	1.7 ± 0.042	1.9 ± 0.13

Table 8-6 Span (dimensionless) of the cumulative normalised undersize distribution of all E and EE samples. Values are given as mean \pm SEM, values marked with matching letters are significantly different according to one-way ANOVA with $p = 0.05$ ($N = 2, n = 3$).

	E-RT	E-RF	E-IB	EE-RT	EE-RF	EE-IB
t_0	1.6 ± 0.043	1.8 ± 0.042^a	1.5 ± 0.030	2.1 ± 0.14	2.0 ± 0.091^{bc}	1.9 ± 0.12^d
t_4	1.5 ± 0.038	1.5 ± 0.034^a	1.5 ± 0.044	1.8 ± 0.096	1.5 ± 0.084^b	1.7 ± 0.063
t_8	1.5 ± 0.047	1.6 ± 0.028^a	1.6 ± 0.030	1.7 ± 0.070	1.2 ± 0.10^c	1.3 ± 0.14^d

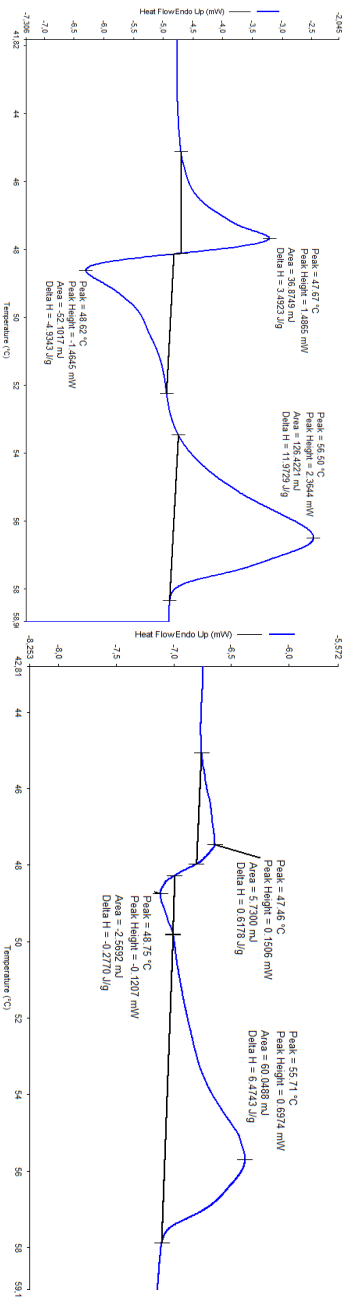


Figure 8-13 DSC curve of the B sample replicates (N = 2) crystallised at a low cooling rate (RT). Melting point determined at t_0 by heating from 20 °C to 70 °C with 2.5 Kmin⁻¹ (endo up).

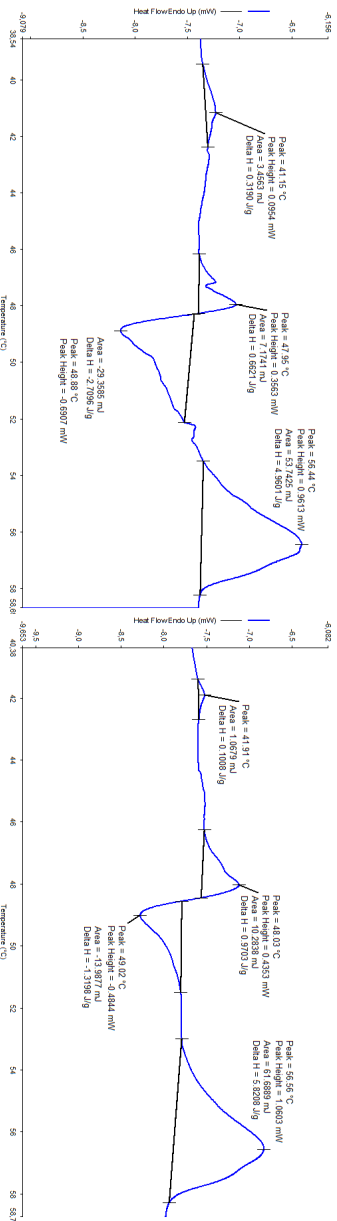


Figure 8-14 DSC curve of the B sample replicates (N = 2) crystallised at a low cooling rate (RT). Melting point determined at t_8 by heating from 20 °C to 70 °C with 2.5 Kmin⁻¹ (endo up).

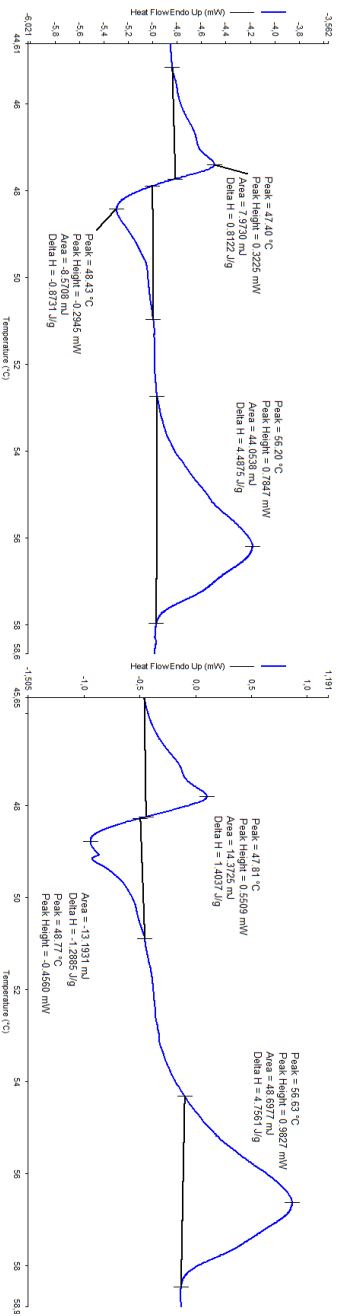


Figure 8-15 DSC curve of the B sample replicates (N = 2) crystallised at a moderate cooling rate (RF). Melting point determined at t_0 by heating from 20 °C to 70 °C with 2.5 Kmin⁻¹ (endo up).

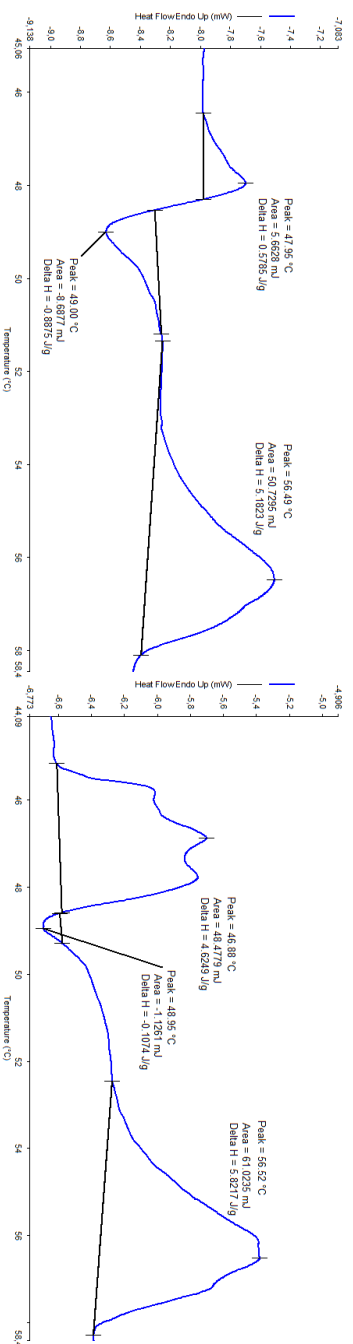


Figure 8-16 DSC curve of the B sample replicates (N = 2) crystallised at a moderate cooling rate (RF). Melting point determined at t_g by heating from 20 °C to 70 °C with 2.5 Kmin⁻¹ (endo up).

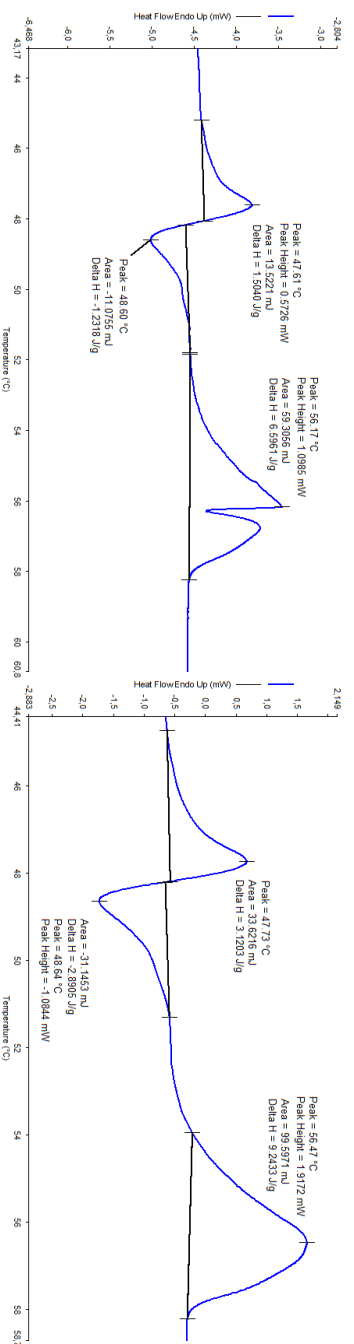


Figure 8-17 DSC curve of the B sample replicates (N = 2) crystallised at a high cooling rate (IB). Melting point determined at t_g by heating from 20 °C to 70 °C with 2.5 Kmin⁻¹ (endo up).

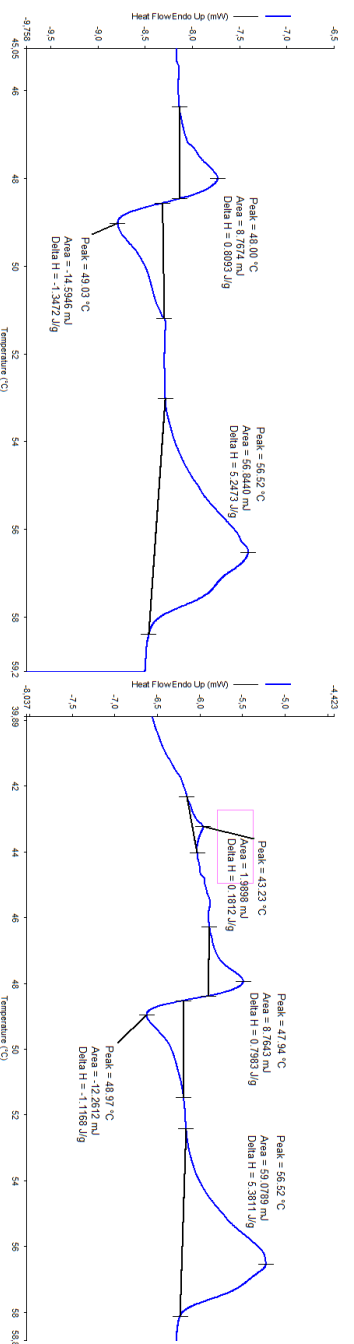


Figure 8-18 DSC curve of the B sample replicates (N = 2) crystallised at a high cooling rate (IB). Melting point determined at t_g by heating from 20 °C to 70 °C with 2.5 Kmin⁻¹ (endo up).

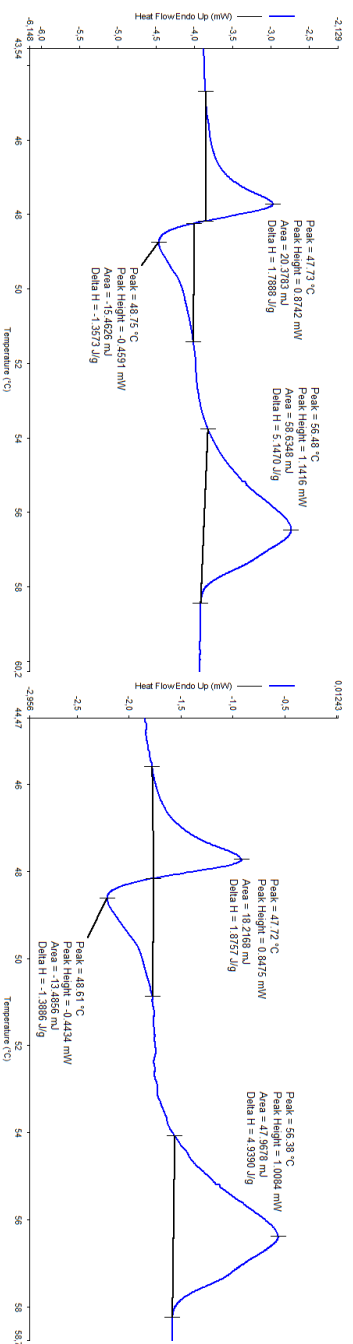


Figure 8-19 DSC curve of the C sample replicates (N = 2) crystallised at a low cooling rate (RT). Melting point determined at t_0 by heating from 20 °C to 70 °C with 2.5 Kmin⁻¹ (endo up).

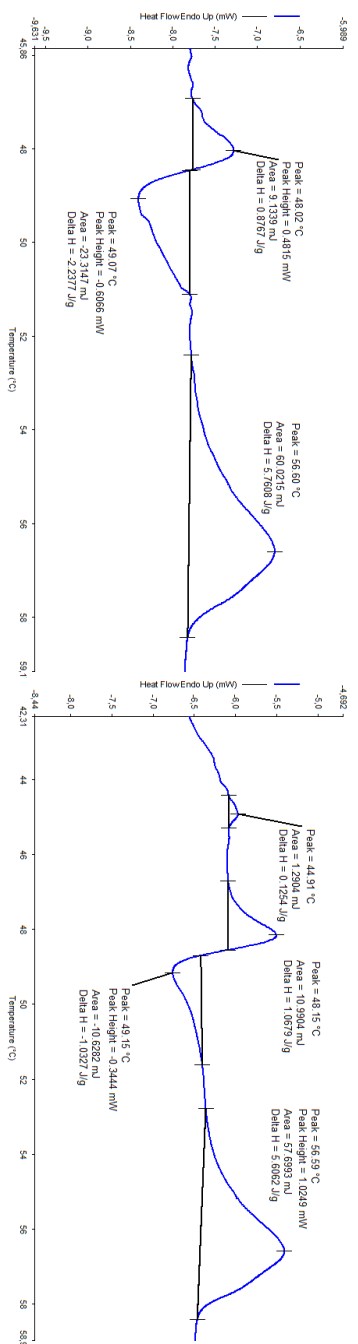


Figure 8-20 DSC curve of the C sample replicates (N = 2) crystallised at a low cooling rate (RT). Melting point determined at t_0 by heating from 20 °C to 70 °C with 2.5 Kmin⁻¹ (endo up).

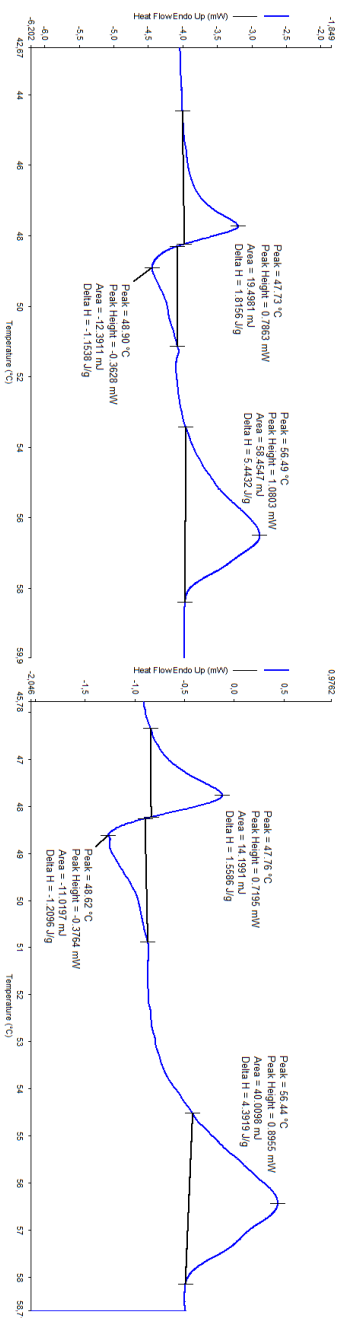


Figure 8-21 DSC curve of the C sample replicates (N = 2) crystallised at a moderate cooling rate (RF). Melting point determined at t_0 by heating from 20 °C to 70 °C with 2.5 Kmin⁻¹ (endo up).

XXX

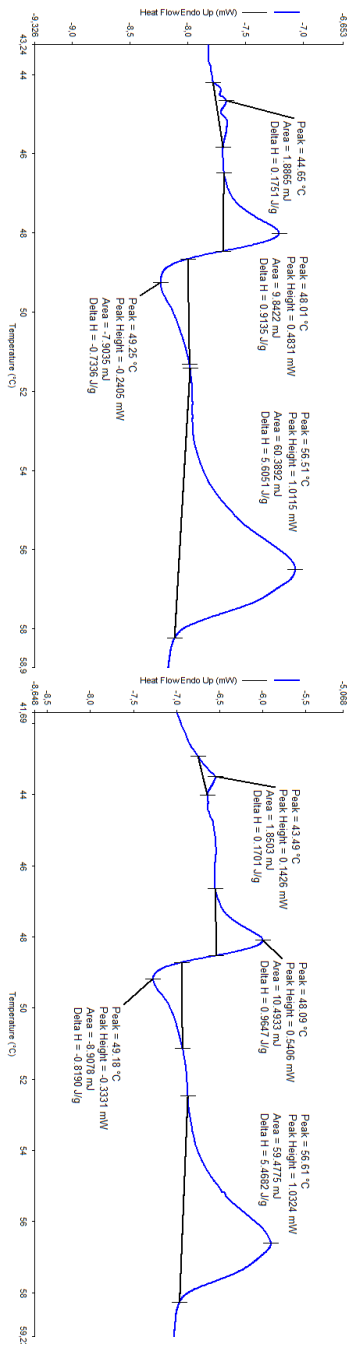


Figure 8-22 DSC curve of the C sample replicates (N = 2) crystallised at a moderate cooling rate (RF). Melting point determined at t_g by heating from 20 °C to 70 °C with 2.5 Kmin⁻¹ (endo up).

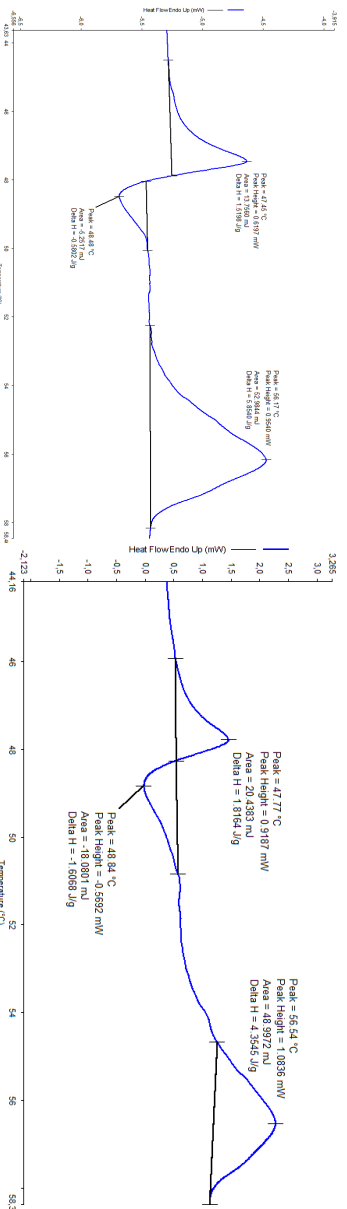


Figure 8-23 DSC curve of the C sample replicates (N = 2) crystallised at a high cooling rate (IB). Melting point determined at t_g by heating from 20 °C to 70 °C with 2.5 Kmin⁻¹ (endo up).

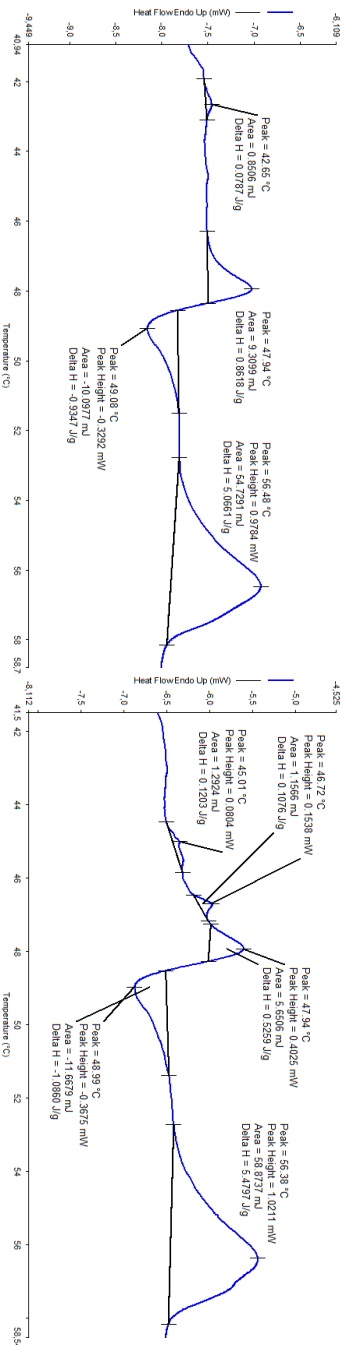


Figure 8-24 DSC curve of the C sample replicates (N = 2) crystallised at a high cooling rate (IB). Melting point determined at t_g by heating from 20 °C to 70 °C with 2.5 Kmin⁻¹ (endo up).

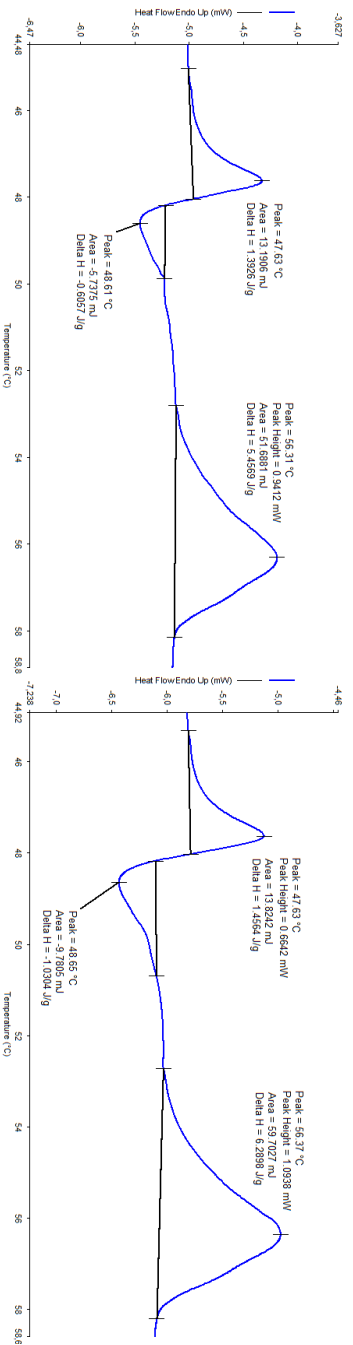


Figure 8-25 DSC curve of the CC sample replicates (N = 2) crystallised at a low cooling rate (RT). Melting point determined at t_0 by heating from 20 °C to 70 °C with 2.5 Kmin⁻¹ (endo up).

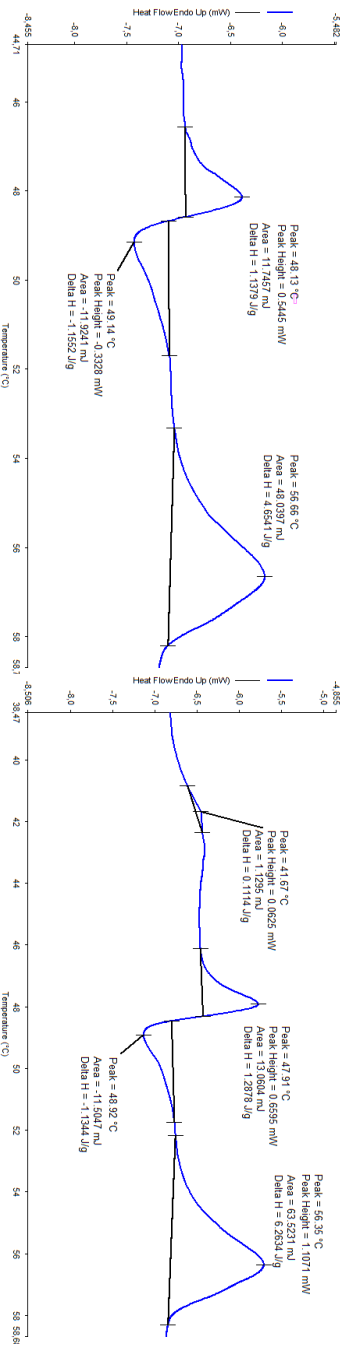


Figure 8-26 DSC curve of the CC sample replicates (N = 2) crystallised at a low cooling rate (RT). Melting point determined at t_0 by heating from 20 °C to 70 °C with 2.5 Kmin⁻¹ (endo up).

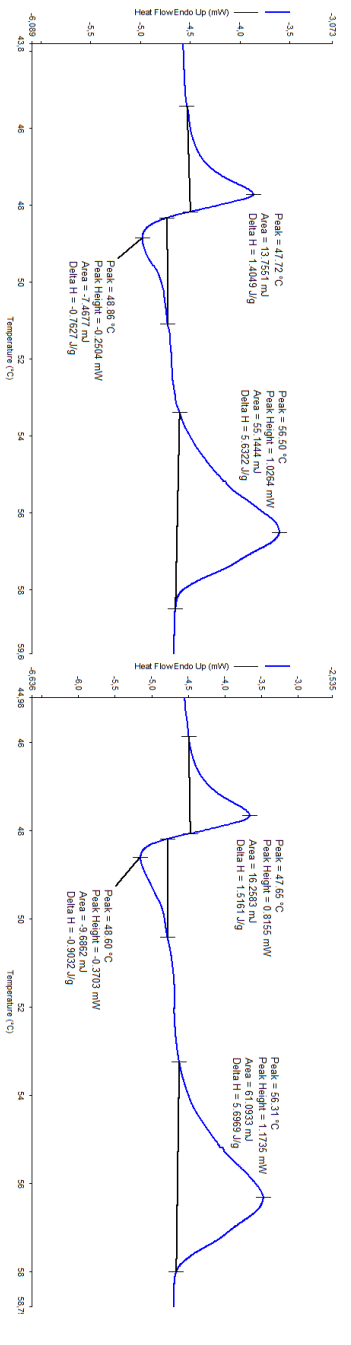


Figure 8-27 DSC curve of the CC sample replicates (N = 2) crystallised at a moderate cooling rate (RF). Melting point determined at t_0 by heating from 20 °C to 70 °C with 2.5 Kmin⁻¹ (endo up).

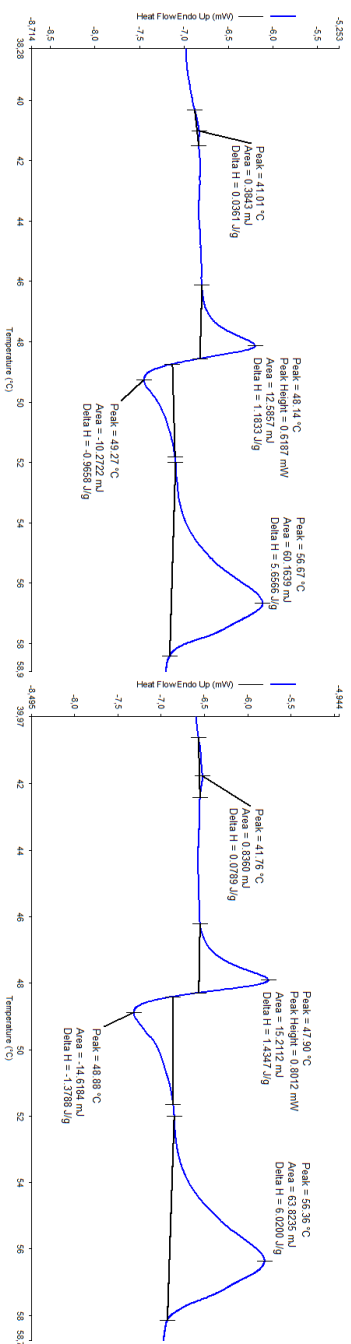
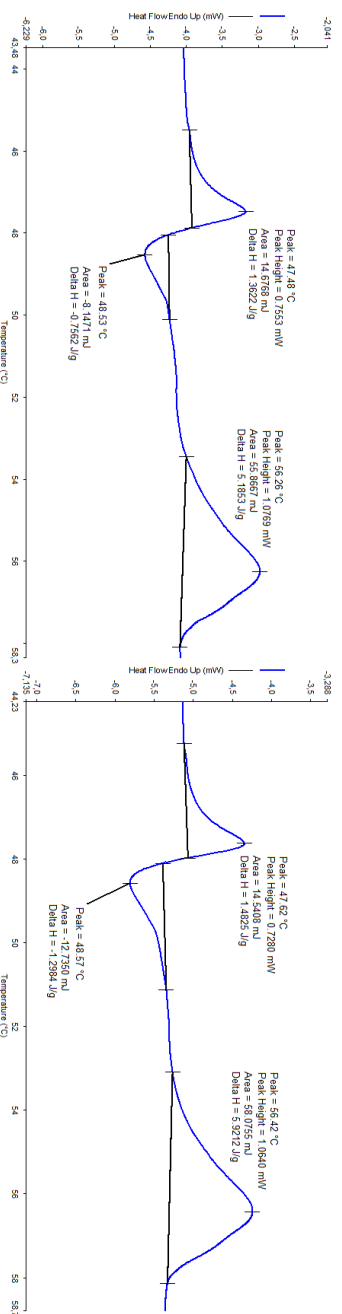
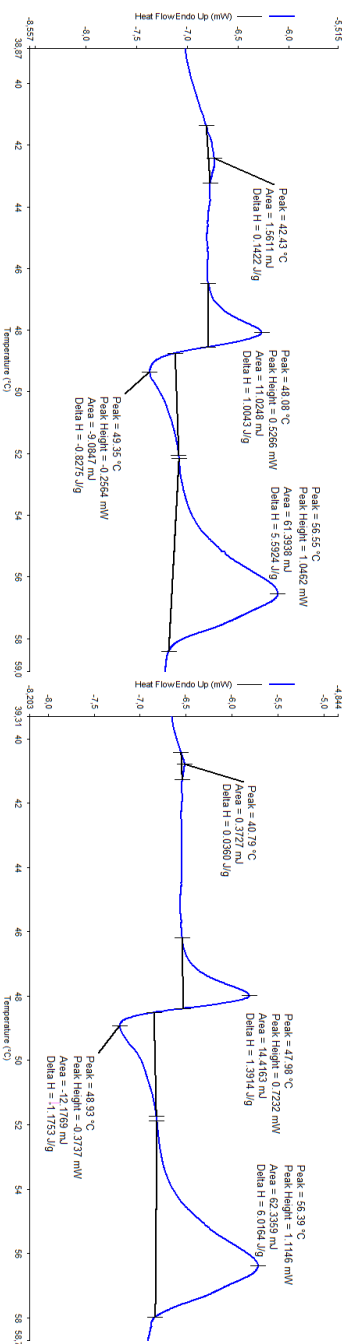


Figure 8-30 DSC curve of the CC sample replicates (N = 2) crystallised at a high cooling rate (lf). Melting point determined at t_g by heating from 20 °C to 70 °C with 2.5 Kmin⁻¹ (endo up).

XXXXIII

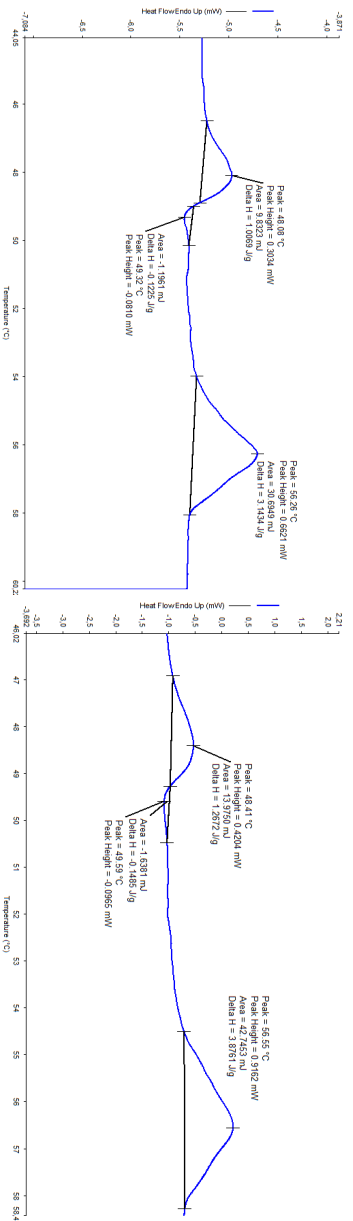


Figure 8-31 DSC curve of the E sample replicates (N = 2) crystallised at a low cooling rate (RT). Melting point determined at t_0 by heating from 20 °C to 70 °C with 2.5 Kmin⁻¹ (endo up).

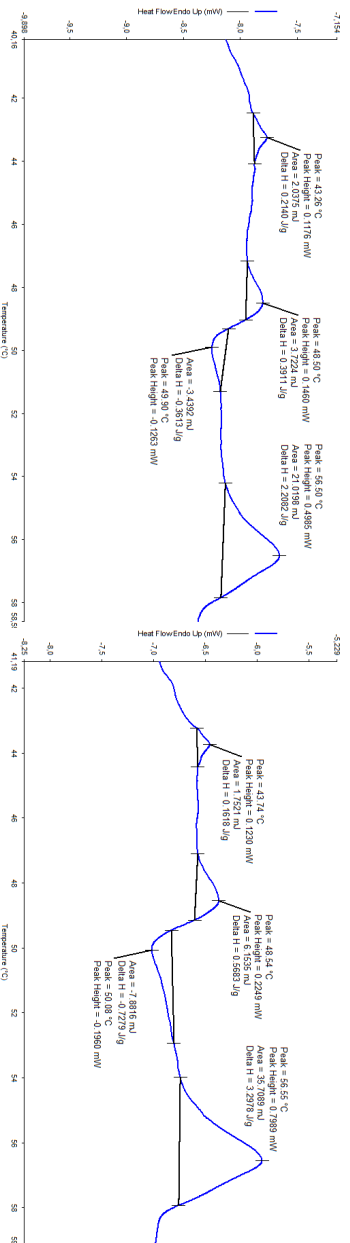


Figure 8-32 DSC curve of the E sample replicates (N = 2) crystallised at a low cooling rate (RT). Melting point determined at t_0 by heating from 20 °C to 70 °C with 2.5 Kmin⁻¹ (endo up).

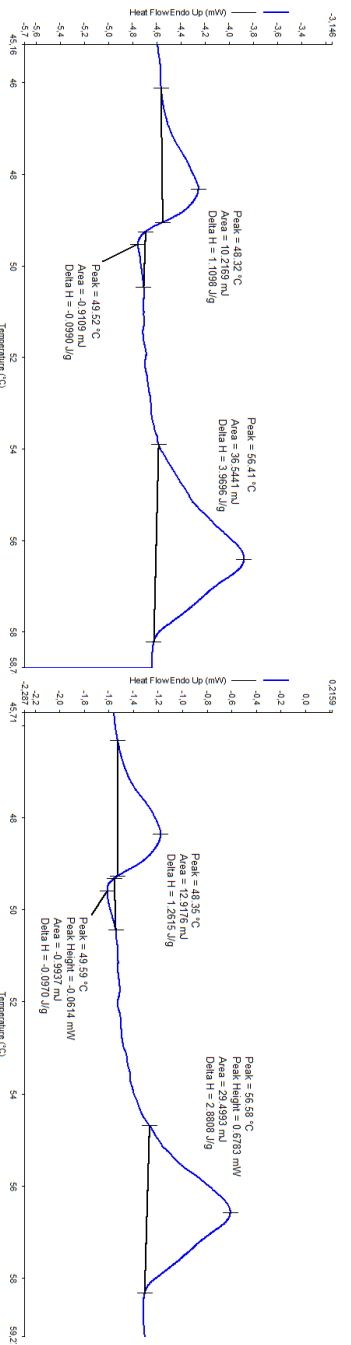


Figure 8-33 DSC curve of the E sample replicates (N = 2) crystallised at a moderate cooling rate (RF). Melting point determined at t_0 by heating from 20 °C to 70 °C with 2.5 Kmin⁻¹ (endo up).

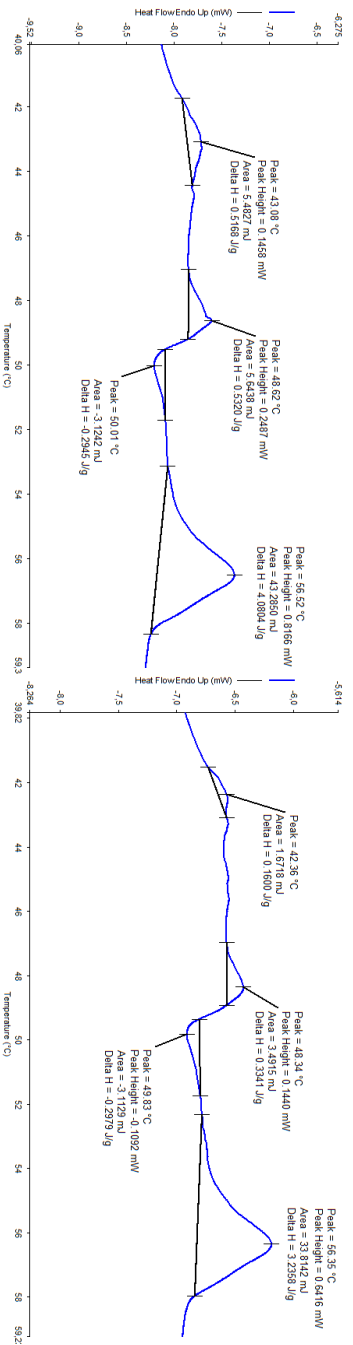


Figure 8-34 DSC curve of the E sample replicates (N = 2) crystallised at a moderate cooling rate (RF). Melting point determined at t_g by heating from 20 °C to 70 °C with 2.5 Kmin⁻¹ (endo up).

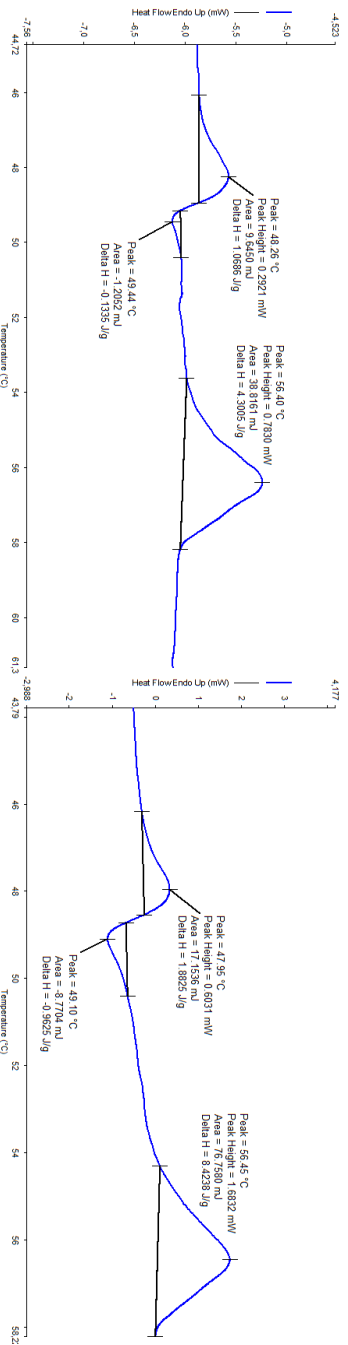


Figure 8-35 DSC curve of the E sample replicates (N = 2) crystallised at a high cooling rate (IB). Melting point determined at t_g by heating from 20 °C to 70 °C with 2.5 Kmin⁻¹ (endo up).

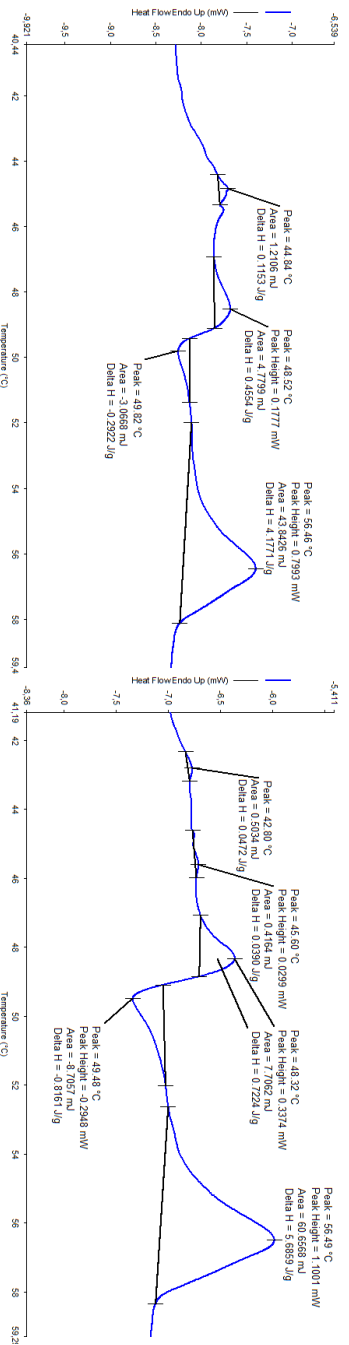


Figure 8-36 DSC curve of the E sample replicates (N = 2) crystallised at a high cooling rate (IB). Melting point determined at t_g by heating from 20 °C to 70 °C with 2.5 Kmin⁻¹ (endo up).

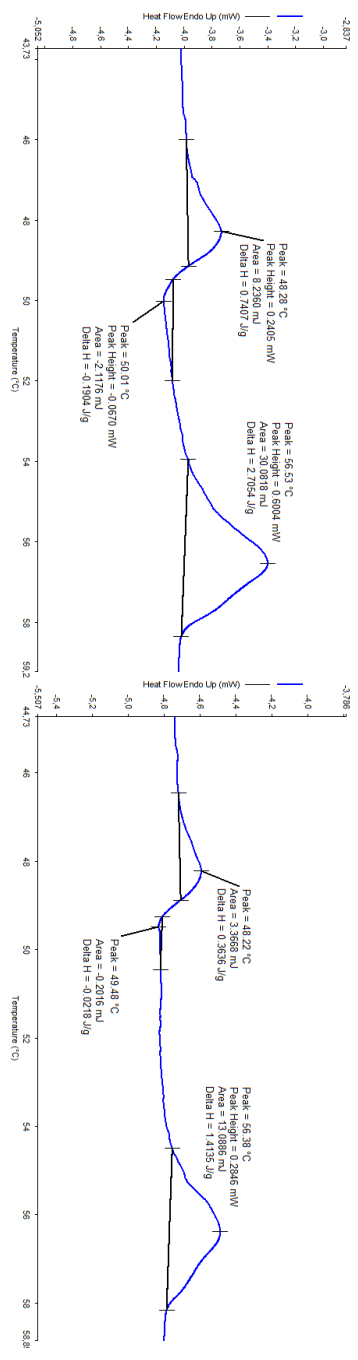


Figure 8-37 DSC curve of the EE sample replicates (N = 2) crystallised at a low cooling rate (RT). Melting point determined at t_0 by heating from 20 °C to 70 °C with 2.5 Kmin⁻¹ (endo up).

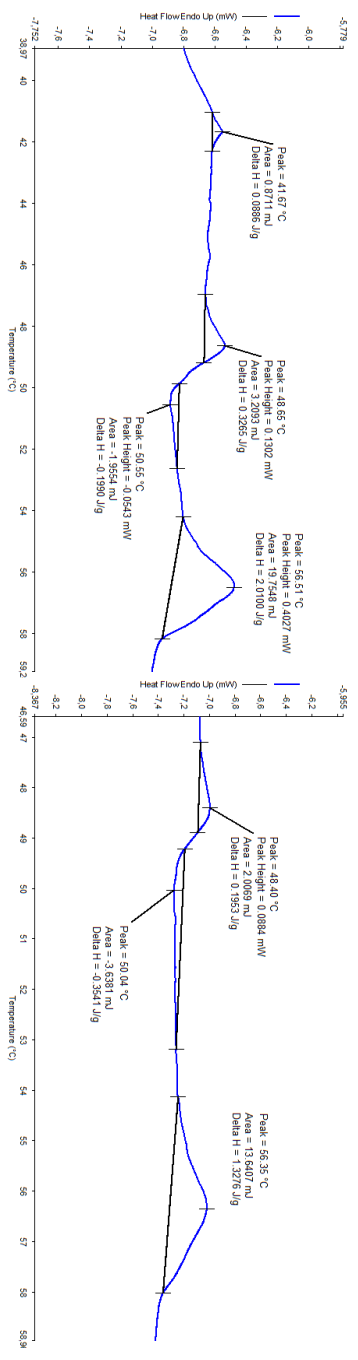


Figure 8-38 DSC curve of the EE sample replicates (N = 2) crystallised at a low cooling rate (RT). Melting point determined at t_0 by heating from 20 °C to 70 °C with 2.5 Kmin⁻¹ (endo up).

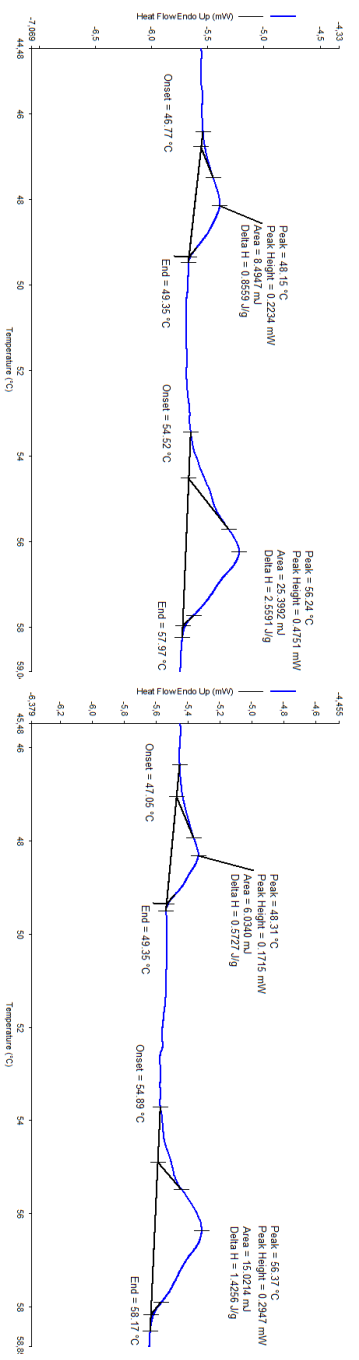


Figure 8-39 DSC curve of the EE sample replicates (N = 2) crystallised at a moderate cooling rate (RP). Melting point determined at t_0 by heating from 20 °C to 70 °C with 2.5 Kmin⁻¹ (endo up).

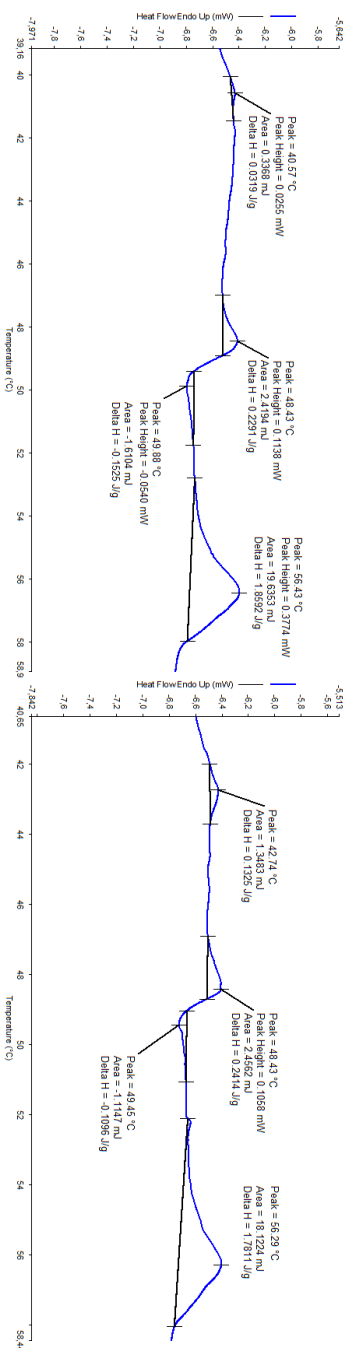
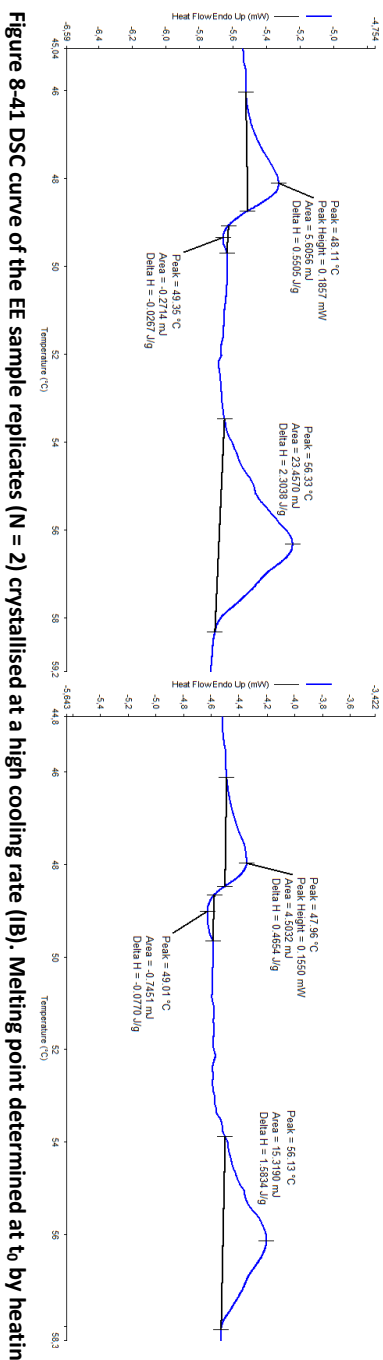
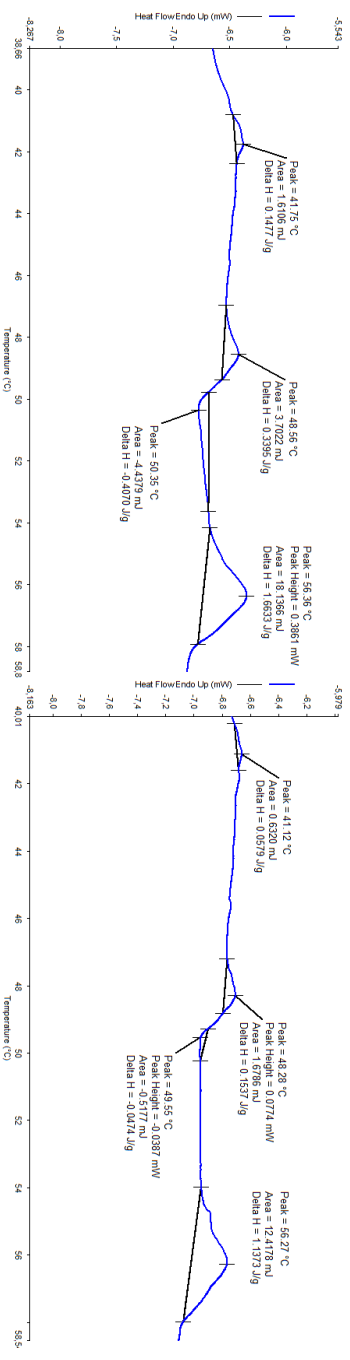


Figure 8-42 DSC curve of the EE sample replicates (N = 2) crystallised at a high cooling rate (IB). Melting point determined at t_g by heating from 20 °C to 70 °C with 2.5 Kmin⁻¹ (endo up).